FEM APPROXIMATION OF MAXWELL EQUATIONS: THE SOURCE PROBLEM, EIGENPROBLEM, AND ELECTROMAGNETIC WAVES

A THESIS SUBMITTED TO
THE GRADUATE SCHOOL OF APPLIED MATHEMATICS
OF
MIDDLE EAST TECHNICAL UNIVERSITY

BY

TUGAY DAĞLI

IN PARTIAL FULFILLMENT OF THE REQUIREMENTS
FOR
THE DEGREE OF MASTER OF SCIENCE
IN
SCIENTIFIC COMPUTING

JANUARY 2023

Approval of the thesis:

FEM APPROXIMATION OF MAXWELL EQUATIONS: THE SOURCE PROBLEM, EIGENPROBLEM, AND ELECTROMAGNETIC WAVES

submitted by **TUGAY DAĞLI** in partial fulfillment of the requirements for the degree of **Master of Science in Scientific Computing Department, Middle East Technical University** by,

Prof. Dr. A. Sevtap Selçuk-Kestel
Dean, Graduate School of **Applied Mathematics** _____

Assoc. Prof. Dr. Önder Türk
Head of Department, **Scientific Computing** _____

Assoc. Prof. Dr. Önder Türk
Supervisor, **Scientific Computing, METU** _____

Examining Committee Members:

Prof. Dr. Özlem Özgün
Electrical and Electronics Engineering, Hacettepe University _____

Assoc. Prof. Dr. Önder Türk
Scientific Computing, METU _____

Prof. Dr. Ömür Uğur
Scientific Computing, METU _____

Date: _____

I hereby declare that all information in this document has been obtained and presented in accordance with academic rules and ethical conduct. I also declare that, as required by these rules and conduct, I have fully cited and referenced all material and results that are not original to this work.

Name, Last Name: TUGAY DAĞLI

Signature :

ABSTRACT

FEM APPROXIMATION OF MAXWELL EQUATIONS: THE SOURCE PROBLEM, EIGENPROBLEM, AND ELECTROMAGNETIC WAVES

Dağlı, Tugay
M.S., Department of Scientific Computing
Supervisor : Assoc. Prof. Dr. Önder Türk

January 2023, 139 pages

In this thesis, edge-based finite element method (FEM) approximations of Maxwell's equations describing the relationship between the space variables and sources along the electromagnetic field are considered. In particular, the lowest-order Nédélec basis functions are implemented to construct the FEM model of the Maxwell source problem, Maxwell eigenvalue problem (EVP), and electromagnetic wave propagation problem. A computational model is constructed to conduct all these problems in the same framework of an approximation formalism.

The convergence properties of the Maxwell EVP formulation are analyzed by applying the spectral theory with those of the associated boundary value source problem. Therefore, the analyses for both of these problems are given together with the corresponding numerical results validating the theoretical features. Moreover, a comparison between the two convergent FEM approximations of the Maxwell EVP that utilizes the lowest-order Nédélec and the linear Lagrange basis functions is performed. This comparison is done by using a special triangulation, namely, a Powell-Sabin type, of the domain that contains a strong singularity.

The electromagnetic wave propagation problem is also considered using two different approaches, namely, a direct time-domain approximation method and a modal analysis technique. For both approaches, a FEM model of the wave propagation problem

is obtained by discretizing the spatial domain using the lowest-order Nédélec basis functions. The time domain approximation of this problem is obtained by employing a finite difference (FD) scheme to approximate the second-order temporal derivative in the obtained FEM model. On the other hand, the frequency domain approximation is acquired by truncating the modal expansion solution. Here, it is set forth that the solution to the electromagnetic wave propagation problem can be represented by an expansion of the approximate eigenmodes that are obtained from the associated Maxwell EVP. As a consequence, it is shown by exploiting the numerical test case of the inhomogeneous wave propagation problem that both methodologies lead to accurate approximations which agree well with each other.

Keywords: Maxwell's equations, Maxwell source problem, Maxwell eigenvalue problem, Electromagnetic wave propagation problem, Finite elements, Edge elements, Modal analysis

ÖZ

MAXWELL DENKLEMLERİNİN SONLU ELEMANLAR YÖNTEMİ YAKLAŞIMI: KAYNAK PROBLEMİ, ÖZDEĞER PROBLEMİ VE ELEKTROMANYETİK DALGALAR

Dağlı, Tugay
Yüksek Lisans, Bilimsel Hesaplama Bölümü
Tez Yöneticisi : Doç. Dr. Önder Türk

Ocak 2023, 139 sayfa

Bu tezde, uzay değişkenleri ile elektromanyetik alan boyunca kaynaklar arasındaki ilişkiyi açıklayan Maxwell denklemlerinin kenar tabanlı sonlu elemanlar yöntemi (SEY) yaklaşımları ele alınmıştır. Özel olarak, Maxwell kaynak probleminin, Maxwell özdeğer probleminin (ÖDP) ve elektromanyetik dalga yayılım probleminin SEY modelini oluşturmak için en düşük dereceli Nédélec temel fonksiyonları uygulanmıştır. Tüm bu problemleri aynı yaklaşım yöntemi çerçevesinde yürütmek için bir hesaplama modeli oluşturulmuştur.

Maxwell ÖDP formülasyonunun yakınsama özellikleri, ilgili sınır değer kaynak problemininkilerle spektral teori uygulanarak analiz edilmiştir. Bu nedenle, bu problemlerin her ikisi için analizler, teorik özellikleri doğrulayan sayısal sonuçlarla birlikte verilmiştir. Ayrıca, en düşük dereceli Nédélec ve birinci dereceli Lagrange baz fonksiyonlarını kullanan Maxwell ÖDP'nin iki yakınsak FEM yaklaşımı arasında bir karşılaştırma yapılmıştır. Bu karşılaştırma, güçlü bir tekillik içeren bölgenin Powell-Sabin adında özel bir üçgenlemesi kullanılarak yapılmıştır.

Elektromanyetik dalga yayılımı problemi de doğrudan zaman-bölgesi yaklaşım yöntemi ve modal analiz tekniği olmak üzere iki farklı yaklaşım kullanılarak ele alınmıştır. Her iki yaklaşım için de, dalga yayılma probleminin bir SEY modeli, en düşük

dereceli Nédélec temel fonksiyonlarını kullanarak uzaysal alanı ayrıklaştırarak elde edilmiştir. Bu problemin zaman alanı yaklaşımı, elde edilen SEY modelinde ikinci dereceden zamansal türevi yaklaşık olarak bulmak için bir sonlu farklar yaklaşımı kullanılarak elde edilmiştir. Öte yandan, frekans alanı yaklaşımı, modal açılım çözümünün kesilmesiyle elde edilmiştir. Burada, elektromanyetik dalga yayılım probleminin çözümünün, ilgili Maxwell ÖDP'den elde edilen yaklaşık özmodların açılımıyla temsil edilebileceği ortaya konmuştur. Sonuç olarak, homojen olmayan dalga yayılımı probleminin sayısal testlerinden yararlanarak, her iki metodolojinin de birbiriyle iyi uyum sağlayan doğru yaklaşımlarla sonuçlandığı gösterilmiştir.

Anahtar Kelimeler: Maxwell denklemleri, Maxwell kaynak problemi, Maxwell özdeğer problemi, Elektromanyetik dalga yayılım problemi, Sonlu elemanlar, Kenar elemanları, Modal analiz

To My Family

ACKNOWLEDGMENTS

I would like to express my sincere gratitude to my thesis supervisor Assoc. Prof. Dr. Önder Türk for his patient guidance, enthusiastic encouragement, and valuable advices during the development and preparation of this thesis. His willingness to give his time and share his experiences has brightened my path.

I would also like to thank my colleagues for creating a friendly and supportive environment. Their companionship helped me a lot during this journey.

I especially want to express my very appreciation to Seda for her unconditional love and support in every aspect of my life.

I owe my deepest gratitude to my dear family, Aytül, Hakan, Meliha, Basri, and Koray for their indescribable love, encouragement, and support.

TABLE OF CONTENTS

ABSTRACT vii

ÖZ ix

ACKNOWLEDGMENTS xiii

TABLE OF CONTENTS xv

LIST OF TABLES xxi

LIST OF FIGURES xxiii

LIST OF ABBREVIATIONS xxvi

CHAPTERS

1 INTRODUCTION 1

1.1 Literature Survey 2

1.1.1 FEM for the Maxwell Equations and Eigenvalue Problems 3

1.1.2 Finite Elements for the Electromagnetic Wave Propagation Problem 8

1.1.3 Modal Analysis of the Electromagnetic Wave Propagation Problem 11

1.2 Plan of the Thesis 13

1.3 Contributions in the Thesis 13

2 MAXWELL'S EQUATIONS 17

2.1 Maxwell's Equations 17

2.1.1 Constitutive Relations 18

2.2 Perfect Electric Conductor Boundary Condition 20

2.3 The Wave Propagation Problem For an Electric Field 21

2.4 Time-Harmonic Maxwell's Equations 22

2.4.1 Time-Harmonic Maxwell's Equations in a Perfectly Conducting Cavity 24

3 THE EDGE BASED FINITE ELEMENT METHOD 27

3.1 The Finite Element Method 27

3.2 Function Spaces 28

3.2.1 Real Normed and Inner Product Vector Spaces . . 28

3.2.2 Banach and Hilbert Spaces 30

3.2.3 L^p Spaces 31

3.2.4 Weak Derivatives 31

3.2.5 Sobolev Spaces 32

3.2.6 Traces 34

3.3 Variational Formulation 35

3.3.1 Variational Formulations of Maxwell's Equations . 36

3.3.1.1 Variational Formulations for Maxwell's Source Problem 37

3.3.1.2 Variational Formulations for the Maxwell Eigenvalue Problem 38

3.3.1.3 Variational Formulation for the Electric Wave Propagation Problem 39

3.4 The Galerkin Method 39

3.4.1 Galerkin Orthogonality 40

3.5 Affine Transformation and Numerical Quadrature 41

3.6 $H(\text{curl})$ Conforming Linear Edge Elements of Nédélec . . . 43

3.6.1 Nédélec Basis Functions on the Reference Triangle 44

3.6.2 Nédélec Basis Functions on the Reference Tetrahedron 45

3.6.3 Global Nédélec Basis Functions 47

3.6.4 Assembly of Stiffness and Mass Matrices 49

3.6.5 Convergence Analysis of FEM 50

4 FEM APPROXIMATION OF TIME-HARMONIC MAXWELL'S EQUATIONS USING NÉDÉLEC ELEMENTS 51

4.1 Maxwell's Source Problem 51

4.1.1 Finite Element Formulations 52

4.1.2 Convergence Analysis of the Source Problem . . . 52

4.1.3 Numerical Results of Maxwell's Source Problem . 55

4.2 The Maxwell EVP 59

4.2.1 The Finite Element Formulations 60

4.2.2 Convergence Analysis of the Maxwell EVP 60

4.2.3 Numerical Results of the Maxwell Eigenvalue Problem 65

4.2.3.1 Numerical Results of 2D Domains . . 66

4.2.3.1.1 Square Domain 68

4.2.3.1.2 L-Shape Domain 73

4.2.3.1.3 Cracked Square Domain . 77

4.2.3.1.4 Cracked Domain with Powell-Sabin Triangulation . . . 81

4.2.3.1.5 Square Domain with Two Different Materials 84

4.2.3.1.6 Rectangular Domain with Two Different Materials . 94

4.2.3.2 Numerical Results of 3D Domains . . 99

4.2.3.2.1 Cube 100

4.2.3.2.2 Thick L Shape 104

4.2.3.2.3 Fichera Corner 107

5 MODAL ANALYSIS OF THE ELECTROMAGNETIC WAVE PROPAGATION PROBLEM USING EDGE-BASED FEM 111

5.1 The electric wave propagation problem and modal analysis at continuous level 112

5.2 Finite element approximation of the wave propagation problem and the EVP 113

5.3 The discrete modal analysis 115

5.4 Numerical Results 118

5.4.1 An Inhomogeneous Wave Propagation Problem . . 118

6 CONCLUSION 127

REFERENCES 131

LIST OF TABLES

Table 4.1 Errors and convergence rates in the L^2-norm, $H(\text{curl})$-norm, and $H(\text{curl})$-seminorm for different meshes in square domain $[0, \pi]^2$. 57

Table 4.2 The first ten exact and approximated eigenvalues on a sequence of uniform meshes with the convergence rates. 68

Table 4.3 The first ten exact and approximated eigenvalues on a sequence of criss-cross meshes with the convergence rates. 69

Table 4.4 The first ten exact and approximated eigenvalues on a sequence of unstructured meshes with the convergence rates. 69

Table 4.5 The first five reference and approximated eigenvalues on a sequence of uniform meshes with the convergence rates. 73

Table 4.6 The first five reference and approximated eigenvalues on a sequence of criss-cross meshes with the convergence rates. 73

Table 4.7 The first five reference and approximated eigenvalues on a sequence of unstructured meshes with the convergence rates. 74

Table 4.8 The first ten reference and approximated eigenvalues on a sequence of uniform meshes with the convergence rates. 77

Table 4.9 The first ten reference and approximated eigenvalues on a sequence of criss-cross meshes with the convergence rates. 78

Table 4.10 The first ten reference and approximated eigenvalues using edge elements on a sequence of Powell-Sabin meshes with the convergence rates. 82

Table 4.11 The first ten reference and approximated eigenvalues using nodal elements on a sequence of Powell-Sabin meshes with the convergence rates. 83

Table 4.12 The first ten reference and approximated eigenvalues on a sequence of uniform meshes with the convergence rates ($\epsilon_{r_1} = 0.5$). 85

Table 4.13 The first ten reference and approximated eigenvalues on a sequence of criss-cross meshes with the convergence rates ($\epsilon_{r_1} = 0.5$). 85

Table 4.14 The first ten reference and approximated eigenvalues on a sequence of unstructured meshes with the convergence rates ($\epsilon_{r_1} = 0.5$). 86

Table 4.15 The first ten reference and approximated eigenvalues on a sequence of uniform meshes with the convergence rates ($\epsilon_{r_1} = 0.1$). 89

Table 4.16 The first ten reference and approximated eigenvalues on a sequence of criss-cross meshes with the convergence rates ($\epsilon_{r_1} = 0.1$). 89

Table 4.17 The first ten reference and approximated eigenvalues on a sequence of unstructured meshes with the convergence rates ($\epsilon_{r_1} = 0.1$). 90

Table 4.18 The first five analytical and approximated cutoff wavenumbers on the uniform, criss-cross, and unstructured meshes. 94

Table 4.19 The first five analytical and approximated eigenvalues on a sequence of uniform meshes with the convergence rates. 95

Table 4.20 The first five analytical and approximated eigenvalues on a sequence of criss-cross meshes with the convergence rates. 95

Table 4.21 The first five analytical and approximated eigenvalues on a sequence of unstructured meshes with the convergence rates. 95

Table 4.22 The first eleven exact and approximated eigenvalues on a sequence of uniform meshes with the convergence rates. 100

Table 4.23 The first eleven exact and approximated eigenvalues on a sequence of unstructured meshes with the convergence rates. 101

Table 4.24 The first nine reference and approximated eigenvalues on a sequence of uniform meshes with the convergence rates. 104

Table 4.25 The first nine reference and approximated eigenvalues on a sequence of unstructured meshes with the convergence rates. 105

Table 4.26 The first eight reference and approximated eigenvalues on a sequence of uniform meshes with the convergence rates. 107

Table 4.27 The first eight reference and approximated eigenvalues on a sequence of unstructured meshes with the convergence rates. 108

Table 5.1 Comparison between the two approaches in terms of CPU times and Errors. 125

LIST OF FIGURES

Figure 2.1 Two homogeneous media separated by a surface. 21

Figure 3.1 Reference elements: unit triangle and unit tetrahedron with their tangential unit vectors of the numbered edges. 44

Figure 3.2 The vectors defining the triangle and tetrahedron. 46

Figure 3.3 Signs of edges of two different triangles that are shared in the mesh (thick line indicates the positive direction that is defined by the user). . . . 47

Figure 4.1 Uniform, criss-cross, and unstructured meshes of the square domain. 56

Figure 4.2 Quiver plots of FEM and Exact solutions. 58

Figure 4.3 Contours of FEM and Exact solutions. 58

Figure 4.4 Uniform, criss-cross, and unstructured meshes of the square domain. 68

Figure 4.5 Contours of the first five approximated eigenfunctions using criss-cross mesh with 24448 DOF on Ω_1. 70

Figure 4.5 Contours of the first five approximated eigenfunctions using criss-cross mesh with 24448 DOF on Ω_1. (cont.) 71

Figure 4.6 Quivers of the first five approximated eigenfunctions using criss-cross mesh with 24448 DOF on Ω_1. 72

Figure 4.7 Uniform, criss-cross, and unstructured meshes of the L-shape domain. 73

Figure 4.8 Contours of the first five approximated eigenfunctions using criss-cross mesh with 18304 DOF on Ω_2. 74

Figure 4.8 Contours of the first five approximated eigenfunctions using criss-cross mesh with 18304 DOF on Ω_2. (cont.) 75

Figure 4.9 Quivers of the first five approximated eigenfunctions using criss-cross mesh with 18304 DOF on Ω_2. 76

Figure 4.10 Uniform and criss-cross meshes of the cracked square domain where the red part indicates the boundary. 77

Figure 4.11 Contours of the first five approximated eigenfunctions using criss-cross mesh with 24416 DOF on Ω_3. 78

Figure 4.11 Contours of the first five approximated eigenfunctions using criss-cross mesh with 24416 DOF on Ω_3. (cont.) 79

Figure 4.12 Quivers of the first five approximated eigenfunctions using criss-cross mesh with 24416 DOF on Ω_3. 80

Figure 4.13 Powell-Sabin triangulation of the cracked square domain where the boundary is indicated in red. 81

Figure 4.14 Square domain with two different materials. 84

Figure 4.15 Contours of the first five approximated eigenfunctions using criss-cross mesh with 24416 DOF on Ω_4 ($\epsilon_{r_1} = 0.5$). 86

Figure 4.15 Contours of the first five approximated eigenfunctions using criss-cross mesh with 24416 DOF on Ω_4 ($\epsilon_{r_1} = 0.5$). (cont.) 87

Figure 4.16 Quivers of the first five approximated eigenfunctions using criss-cross mesh with 24416 DOF on Ω_4 ($\epsilon_{r_1} = 0.5$). 88

Figure 4.17 Contours of the first five approximated eigenfunctions using criss-cross mesh with 24416 DOF on Ω_4 ($\epsilon_{r_1} = 0.1$). 91

Figure 4.17 Contours of the first five approximated eigenfunctions using criss-cross mesh with 24416 DOF on Ω_4 ($\epsilon_{r_1} = 0.1$). (cont.) 92

Figure 4.18 Quivers of the first five approximated eigenfunctions using criss-cross mesh with 24416 DOF on Ω_4 ($\epsilon_{r_1} = 0.1$). 92

Figure 4.18 Quivers of the first five approximated eigenfunctions using criss-cross mesh with 24416 DOF on Ω_4 ($\epsilon_{r_1} = 0.1$). 93

Figure 4.19 Rectangle domain with two different materials. 94

Figure 4.20 Contours of the first five approximated eigenfunctions using criss-cross mesh with 24416 DOF on Ω_5. 96

Figure 4.20 Contours of the first five approximated eigenfunctions using criss-cross mesh with 24448 DOF on Ω_5. (cont.) 97

Figure 4.21 Quivers of the first five approximated eigenfunctions using criss-cross mesh with 24416 DOF on Ω_5. 97

Figure 4.21 Quivers of the first five approximated eigenfunctions using criss-cross mesh with 24416 DOF on Ω_5. (cont.) 98

Figure 4.22 Uniform and unstructured meshes of the cube domain. 100

Figure 4.23 Contours of the first nine approximate eigenfunctions on Ω_6. 102

Figure 4.23 Contours of the first nine approximate eigenfunctions on Ω_6. (cont.) 103

Figure 4.24 Uniform and unstructured meshes of the thick L-shape domain. . . 104

Figure 4.25 Contours of the first eight approximate eigenfunctions on Ω_7. . . . 105

Figure 4.25 Contours of the first eight approximate eigenfunctions on Ω_7. (cont.) 106

Figure 4.26 Uniform and unstructured meshes of the fichera corner domain. . . 107

Figure 4.27 Contours of the first five approximate eigenfunctions on Ω_8. 109

Figure 5.1 Coefficients that control the tangential field on the selected edge. . 120

Figure 5.2 Variation of the error at fixed time t^*. 123

Figure 5.3 Coefficients that control the tangential field on the selected edge. . 124

LIST OF ABBREVIATIONS

2D	Two Dimensional
3D	Three Dimensional
DG	Discontinuous Galerkin
DOF	Degrees of Freedom
EVP	Eigenvalue Problem
FD	Finite Difference
FEM	Finite Element Method
HDG	Hybrid Discontinuous Galerkin
PDE	Partial Differential Equation
PEC	Perfect Electric Conductor

CHAPTER 1

INTRODUCTION

Partial differential equations (PDEs) are utilized in many fields of industry and science. In general, exact solutions of PDEs are either too challenging or impossible to obtain. For this reason, numerical approximations of PDEs must be considered by employing numerical techniques such as finite element, finite volume, boundary element, finite difference, and spectral element methods. The goal of using numerical methods is to approximate the exact solution or, if the exact solution does not exist for a particular case, to produce results that are consistent with the experimental results of the relevant case accurately and efficiently. To this end, finite element methods are widely used as approximating methods to obtain accurate and efficient results for PDEs that are mostly related to the natural sciences and engineering.

Finite element methods (FEM) can be characterized as a class of methodologies to approximate functions at a discrete level, which include standard, mixed, conforming, non-conforming, and discontinuous Galerkin methods. These methods perform in a way that utilizes the discretized domain using a set of a finite number of points, edges, faces, elements, and the related basis functions defined on them. Therefore, finite element methods are broadly studied by many researchers because of their ability to produce efficient approximations on geometrically complex domains. Another essential benefit is the feature that differential equations are converted into a system of algebraic equations that can be structured locally over each element using the finite element method.

A set of coupled PDEs known as Maxwell's equations serves as the basis for electromagnetism, optics, and electric circuits. The equations employ a mathematical rep-

resentation of optical, electric, and radio technologies, including radar, lenses, wireless communication, electric motors, and power generation (see, e.g., [77, 101, 104]). Maxwell's equations explain how currents, charges, and changes in the fields produce electric and magnetic fields. Furthermore, the Maxwell eigenvalue problem (EVP) is the problem arising from finding cavity resonators that are important in microwave and optical systems. They are being used as filters or tools to improve physical interactions, radiation antennas, or electromagnetic sources like magnetrons and lasers. They can also be employed to enhance sensor sensitivity (see, e.g., [45, 72, 87]). Additionally, Maxwell's equations describe the propagation of electromagnetic waves in free space or through a medium. The electromagnetic wave propagation problem that is derived from Maxwell's equations simulates physical phenomena such as radio waves, microwaves, X-rays, radars, etc.

In this thesis, the three formulations of Maxwell's equations, which are the source problem, the eigenvalue problem, and the electromagnetic wave propagation problem, are considered. The source and eigenvalue problems are derived in a time-harmonic setting, and the electromagnetic wave propagation problem is obtained in the time domain. The edge-based FEM using the lowest-order Nédélec basis functions is studied to approximate the three formulations of Maxwell's equations. The main reason is that Nédélec basis functions are consistent with the physics of the systems that are modeled by Maxwell equations [88]. Lastly, a modal analysis and FEM in space/finite difference (FD) in time approaches are considered to approximate the electromagnetic wave propagation problem.

1.1 Literature Survey

As Maxwell's equations form the basis of numerous phenomena, researchers focused on approximating Maxwell's equations in both boundary value and eigenvalue problems and the electromagnetic wave propagation problems using various methods throughout the years. Moreover, the modal analysis of the electromagnetic wave propagation problem is performed with the help of the modes obtained by using approximate methodologies.

Problems involving Maxwell's equations are being extensively considered using various methods such as the finite element method, boundary element method [51, 64, 67, 73, 100, 102], finite volume method [2, 3, 92], reduced basis method [54], multigrid methods [103, 106], spectral element method [70], and uncertainty quantification [49]. However, the finite element methods are widely preferred by many researchers in the study of Maxwell's equations and EVP.

A literature survey about the finite element methods for Maxwell's equations and modal analysis of the electromagnetic wave propagation problems is presented below.

1.1.1 FEM for the Maxwell Equations and Eigenvalue Problems

In finite element methods using nodal basis functions for a non-convex polyhedral domain, nodal elements might lead to spurious eigenvalues [23, 63], which may be fixed with the constructions introduced in [19, 30, 36, 37, 38]. Bossavit focused on both edge and node-based finite element approximations of Maxwell's equations and presented that the node-based finite elements cause spurious solutions, and using edge elements prevents the unphysical, the so-called "spurious modes" in [23]. In [63], Konrad proposed a nodal finite element method for approximating Maxwell's equations in 3D that reduces the number of spurious solutions but could not be fully eliminated. In [30], Caorsi, Fernandes, and Raffetto explained the reason and the behavior of spurious solutions in Galerkin finite element approximations of Maxwell EVP. Furthermore, the convergence of Galerkin finite element approximations of electromagnetic eigenproblems is investigated in this paper using two slightly different definitions of convergence, the second of which clarifies the intuitive concept of the "spurious-free method." While both definitions include necessary and sufficient conditions, only the newly proposed one proves that whether or not an approximation converges for a given family of finite element triangulations is unaffected by the properties of the materials in the cavity. In addition, they showed that the lowest-order edge elements fulfill discrete compactness and allow convergent approximations even in the eigenproblem, including anisotropic, inhomogeneous, and discontinuous material properties. In [37], Costabel and Dauge proposed a method for approximating time-harmonic Maxwell's equations on 2D and 3D polyhedral domains using

nodal finite elements. They regularized the divergence part of the problem to prevent spurious solutions in the presence of reentrant corners or edges by introducing special weights inside the divergence integral. They proved that the presented method produces accurate approximations. In [38], Costabel and Dauge focused on the approximation of Maxwell eigenvalues with perfectly conducting boundary conditions on polyhedral cavities using the nodal finite element method. They used nodal elements since the bilinear form corresponding to the curl-curl operator is regularized to eliminate the gradient fields. In addition, to avoid the bilinear form corresponding to the divergence operator from converging to a wrong solution in the domain with reentrant edges or corners, they modified it using the method of addition of singular functions and the method of regularization with weight. In [8], Badia and Codina proposed the nodal FEM to approximate Maxwell's problem using a newly introduced formulation of the continuous problem and a stabilization. They demonstrated the suggested approach's convergent characteristics for singular and smooth solutions. In [44], Duan, Tan, Yang, and You presented the nodal FEM with Lagrange linear elements, with one element bubble per element. The proposed method produced accurate results for the general Maxwell's eigenvalue and source problems with the discontinuous and nonhomogeneous medium. In addition, in some examples given in the study, it is shown that the method is suitable for singular solutions. In [42], Duan, Du, Liu, and Zhang approximated both Maxwell source and eigenvalue problems using mixed elements that are inf-sup stable. They used nodal Lagrange elements for the discretization of the electric field and discontinuous piecewise constant elements for the Lagrange multiplier. The suggested method gives spectral-correct, spurious-free approximations when applied to the eigenvalue problem, as shown in a theory together with the numerical experiments that verify the findings. In [43], Duan, Liu, Ma, Tan, and Zhang studied the Lagrange basis functions for the FEM solution of Maxwell's equations. They obtained optimally convergent results for both singular and smooth solutions using the Lagrange elements of order greater than or equal to two on barycentric refinements. In [19], the spurious-free approximations of Maxwell EVP in two-dimensional domains using Lagrange elements are considered. Specifically, the convergence analysis of FEM that employs the linear Lagrange basis functions on Powell-Sabin triangulation, the quadratic Lagrange basis functions on Clough-Tocher triangulation, and the quartic (or higher) Lagrange basis functions on

general shape-regular triangulations for Maxwell EVP in two dimensions are demonstrated by Boffi, Guzmán, and Neilan.

Many researchers studying Maxwell's equations use the Discontinuous Galerkin approximation as an alternative to the Galerkin approximation due to its ability to provide spurious free results. In [28], Buffa and Perugia presented necessary and sufficient conditions for the Discontinuous Galerkin spurious-free approximation of the Maxwell source problem with discontinuous material parameters and suitable boundary conditions. In [26], Buffa, Houston, and Perugia proposed several numerical experiments that both support the theory presented in [28] and provided more insight into discontinuous Galerkin methods. They demonstrated, in particular, that the DG techniques do not yield arbitrary spurious solutions on conformal meshes. In [55], Hestheaven and Warburton approximated the Maxwell EVP using a high-order nodal discontinuous Galerkin (DG) method. For 2D problems, the straightforward application of the DG method was efficiently performed since it did not support any spurious modes, even for the singular problems. However, a modification was needed to control spurious solutions in 3D cases to achieve an efficient approximation. The results show that the high-order nodal DG method is an accurate, efficient alternative to the classical Galerkin method. In [29], Buffa, Perugia, and Warburton obtained spurious-free approximations on general irregular meshes in the two-dimensional domain by using a projection-based penalization at non-conforming interfaces, which is a mortar-type method. They used a mortar-type method to prevent the possibility of spurious solutions on general irregular meshes and proved that the proposed DG method is spectrally correct. They provided numerical examples of both convex and non-convex problem domains to demonstrate the theoretical results with regular and discontinuous material coefficients. In [79], the numerical solution of time-harmonic Maxwell's equation using two hybridizable discontinuous Galerkin (HDG) methods was proposed by Nguyen, Peraire, and Cockburn. The mixed curl-curl formulation is approximated by the first HDG method, and the vector wave formulation is approximated by the second HDG method. The presented HDG methods provided the results of standard DG approximation for the time-harmonic Maxwell's equation with some additional advantages. In particular, the HDG methods have less number of globally coupled unknowns in comparison with the standard DG methods, and this leads to

an advantage in terms of both computational and memory costs. Also, for smooth solutions, the numerical solution can be post-processed at the element level, and for singular solutions, in order to improve accuracy, local post-processing is effective.

The mixed FEMs are studied to resolve the divergence-free condition to prevent numerical schemes from producing spurious solutions. In [75], the Maxwell equations on a domain that smooth and bounded are approximated using a semidiscrete mixed finite element and analyzed by Monk. He proved a convergence for mixed methodologies and showed that it could be useful in the proof of estimates when Nedelec's elements are used. In [21], Bonito and Guermond also approximated Maxwell's EVP using the mixed method with the nodal-based finite element discretization and the control of divergence-free condition in a fractional Sobolev space. In [57], Jiang, N. Liu, Tang, and Q. H. Liu approximated Maxwell's EVP by using mixed FEM with the introduction of the Lagrangian multiplier. They make use of the lowest-order edge-based basis functions to interpolate the field whereas first-order nodal basis functions for the Lagrangian to prevent spurious solutions. In [85], Qiao, Yao, and Jia proposed a nonconforming mixed finite element approximation of 3D the time-harmonic Maxwell equation with superconvergence and extrapolation analysis. They concluded that this mixed finite element possesses super-close characteristics. In addition, a post-process operator achieved global superconvergence, implying it can enhance the order of approximation from 1 to 2 with the perfectly conducting boundary condition. In [27], Buffa, Ciarlet Jr., and Jamelot approximated the Maxwell EVP. They used mixed FEM with the discretization of an electric field using the weighted method of Costabel and Dauge [37] and the discretization of the Lagrange multiplier employing the Zero Near Singularity finite element pair of Ciarlet Jr. and Hechme [82].

The following works compared the finite element methods using nodal and edge elements. In [88], Reddy, Deshpande, Cockrell, and Beck applied nodal-based and edge-based FEM to Maxwell's eigenvalue problem (EVP). Implementation of nodal-based finite elements resulted in spurious solutions. The implementation of edge-based finite elements eliminated spurious solutions because of the properties of edge-based basis functions and their consistency with the physical properties of Maxwell's EVP. In [14], Boffi, Farina, and Gastaldi compared some finite element method approximations (nodal and edge finite elements) based on two variational formulations (un-

constrained and penalized formulations) of Maxwell EVP on different domains. In addition, to deal with the penalized formulation in the presence of reentrant corners, they presented a new non-standard finite element method: a biquadratic element with a suitable projection. They concluded that the edge finite element approximation is generally well suited for the problem. The best choice for the problem in a convex domain is using nodal elements for the penalized formulation. However, nodal finite element approximation should not be considered when the domain has a reentrant corner. In particular, no conforming nodal finite element approximation of the penalized formulation can produce satisfactory results. Terminally, the presented new non-standard finite element method performed well with the difficulty of imposing boundary conditions in the vertices of reentrant corners.

The studies that compared nodal and edge finite elements showed that edge finite elements produce spurious-free, convergent approximations for Maxwell EVP, and edge elements are consistent with the physical properties of Maxwell EVP. In [80], for the spatial discretization of Maxwell's equations in $\mathbb{R}^3$, Nédélec proposed a finite element method. The method, which uses his unusual curl- and divergence-conforming elements, simultaneously discretize the electric and magnetic fields. One advantage of this approach is that the discrete divergence-free magnetic displacement can be produced if the proper initial data is used. A second benefit is that the approach transparently manages discontinuous material features. In [74], Monk proved optimal-order convergence estimates by analyzing the generalization of Nédélec's scheme studied in [80]. He further showed that when the material is dielectric, and the electromagnetic field is in vacuum or free space, the Nédélec method can be superconvergent. In [15], Boffi, Fernandes, Gastaldi, and Perugia proposed a criterion to investigate if the edge FEM is convenient for the eigensolution of Maxwell's system. In [16], Boffi and Gastaldi used edge element spaces and imposed the divergence condition. Known properties of edge elements are reviewed, and uniform convergence in the L^2-norm is proved. In [20], Boffi, Kukichi, and Schoberl analyzed a modification of standard edge elements that restores the optimality of the convergence based on a projection technique since Nedelec edge elements do not perform acceptable approximation on quadrilateral meshes as proved in the study. In [18], Boffi, Gastaldi, Rodríguez, and Šebestová proved the reliability and efficiency of the residual error

indicator, which they introduced in the study for the Nedelec finite element approximation with the usage of mixed formulation of Maxwell's eigenproblem. In [76], Monk approximated the time-harmonic Maxwell equations on a bounded domain using Nèdèlec edge FEM. A complication arises in the zero electric conductivity case since the bilinear form is no longer coercive. This complication was obviated using a discrete Helmholtz decomposition. In [17], Boffi and Gastaldi focused on the adaptive Nèdèlec edge finite element approximation of the Maxwell EVP in three dimensions with a standard residual-based error indicator and proved the optimal convergence. In [52], for Maxwell EVP in 2D, a linear nonconforming finite element was proposed by Hansbo and Rylander. In proposed element shape functions, degrees of freedom (DOF) are related to the midpoints of the element's edges. The tangential field is continuous at each edge's midpoint, while it is permitted to have a discontinuous normal component, offering an approximation to the Crouziex–Raviart element. The suggested element is devoid of spurious solutions, and the eigenfrequencies related to well-resolved eigenmodes are recreated with the suitable multiplicity for cavity eigenvalue problems. In [78], Monk and Demkowicz proved h-convergence of the edge-based FEM for the approximation of Maxwell source and eigenvalue problems using theory of collectively compact operators. In addition, they expanded the work of Kikuchi [59] that proves the convergence of the lowest-order edge element approximation for Maxwell EVP, which is based on the discrete compactness property, by showing that edge elements of all orders have this property. In [105], optimal error estimates for Nédélec edge element approximation of time-harmonic Maxwell's equations on a general Lipschitz domain in both L^2-norm and $H(curl)$-norm is obtained by Zhong, Shu, Wittum, and Xu. They also presented an optimal convergence estimate for Nédélec's second-type elements.

1.1.2 Finite Elements for the Electromagnetic Wave Propagation Problem

Many researchers focused on approximating the electromagnetic wave propagation problem using various finite element methods such as FEM using nodal elements [62, 84], a hybrid method that combines the finite element method and high-frequency technique [32], discontinues Galerkin methods [41, 99], and FEM using edge elements [5, 11, 56, 68, 89]. Also, various methods of approximating the electromag-

netic wave propagation problems are compared in [66].

The finite element methods using nodal basis functions are presented in the following. In [62], Konrad represented electromagnetic waves in anisotropic media using high-order polynomial triangular finite elements in which the components of vector variational formulation associated with them. Konrad indicated that the formulation is suitable for electromagnetic waves in isotropic and anisotropic lossless mediums. The finite element model is highly accurate when it has adequate degrees of freedom. However, as a drawback, the material property tensors are required to be independent of the frequency, and they must not exhibit spatial change inside the triangles. It is challenging to model curving borders with triangles that have straight edges. In [84], Pinello, Lee, and Cangellaris interpreted electromagnetic wave interactions in two-dimensional dielectric structures using the one-dimensional finite element method by linear interpolating functions. The two-dimensional boundary value problem is converted into a system of coupled ordinary differential equations that is solved using one-dimensional finite elements thanks to the usage of Floquet's theory and the periodic permittivity function's Fourier series expansions. The suggested numerical method's accuracy and effectiveness are shown by comparing outcomes from competing approaches.

Moreover, there are some hybrid techniques for the approximation of electromagnetic wave propagation problems that are presented in the following. In [32], Garcia-Castillo, Gomez-Revuelto, Saez de Adana, and Salazar-Palma introduced a hybrid FEM and high-frequency techniques for the study of electromagnetic waves in complex systems. This method uses linear triangular elements to discretize the electric or magnetic field on the polarization. The analysis of the electrically big objects of the structure is done using a high-frequency approach. In contrast, the study of the areas with small and complex characteristics is done using FEM, considering contacts between the FEM domains and the objects evaluated using high-frequency techniques. In [41], Davies, Morgan, and Hassan studied the approximation of the electromagnetic wave scattering problem using the high-order discontinuous Galerkin method as well as a continuous Galerkin spectral element method for spatial approximation. The time is discretized using a fourth-order Runge-Kutta technique. The method was tested against an exact analytical solution for a circular scatterer before being used for

the simulation of several particular cases in a predictive setting. The results demonstrated the computational advantages of mesh convergence achieved by increasing the order of approximation rather than reducing element size. Additionally, in [99], the electromagnetic wave propagation problem in three dimensions was studied by Tian, Shi, and Chan using the interior penalty discontinuous Galerkin time domain approach. In order to build the relevant system in local elements, they devised the internal penalty fluxes corresponding to various forms of boundary conditions that are frequently employed in electromagnetic modeling. They conducted an analytical study and numerical demonstration of the method's stability. They showed that the suggested method offers a competitive performance in terms of computing time and memory use by contrasting it with the FEM time domain and DG time domain.

The comparison of different finite element methods for the approximation of electromagnetic wave propagation problem is performed in [66] by J. Lee, R. Lee, and Cangellaris. The presented study compared the time-domain point-matched nodal finite element method, nodal finite element method with integral lumping, edge-based finite element method, and finite different time-domain method to approximate the electromagnetic wave propagation problem. In this comparison, the results have shown that the edge-based finite element method gave more accurate results.

The finite element methods using edge basis functions are discussed in subsequent studies. In [11], the electromagnetic wave propagation problem is approximated using the finite element method using the lowest-order Nédeléc edge elements in space and an unconditionally stable finite difference method scheme in time. Also, they introduced the lumping approach to stabilize the numerical scheme to obtain faster convergence. In [56], Hill, Farle, and Dyczij-Edlinger suggested a multilevel solution that uses a partly gauged scheme for the iterative manner and a tree-gauged formulation on the coarsest mesh. Additionally, they have extended the idea of hanging nodes to higher order $H(\text{curl})$-conforming tetrahedral elements. The proposed method allowed a lot of flexibility in the degree of freedom allocation in a hp-adaptive setting. In [89], Ren, Kalscheuer, Greenhalgh, and Maurer applied the adaptive finite element method using Nédélec edge elements. They tested their methodology with two exact solutions and one benchmark for the specific settings and concluded that the proposed approach produces accurate and robust performance. In [68], a finite element time do-

main solution to the electromagnetic wave propagation problem with complex-shaped loop sources was put out by Li, Lu, Farquharson, and Hu. They employed backward Euler for the temporal discretization, local refinement, and vector finite elements for the space with unstructured tetrahedral grids. The numerical results are compared and agreed well with the ones obtained using a frequency-domain finite element solver. In [5], Anees and Angermann introduced an edge-based Nédeléc curl-conforming and Raviart Thomas div-conforming finite elements for the electric and magnetic fields, respectively, and that used backward Euler for the temporal discretization in order to study the approximation of time-dependent Maxwell's equations where it is claimed that the methodology has the benefit of being significantly more powerful and accurate than finite-difference time domain or other existing methods about error estimates and numerical experiments.

1.1.3 Modal Analysis of the Electromagnetic Wave Propagation Problem

The modal analysis technique is employed in the context of electromagnetic wave propagation problem using the pseudospectral modal method [96], spectral element method [69], discontinuous Galerkin method [4], finite difference method [39, 98], and finite element methods [10, 48, 81, 94, 104].

The modal analysis of the electromagnetic wave propagation problem using the finite difference method is presented in the following. In [98], Thomas, Sewell, and Benson used a full-vectorial higher-order finite-difference method to estimate the electromagnetic wave propagation problem for rectangular dielectric waveguides. The approach is semi-analytical in design and employs unique difference equations for the homogeneous, interface, and corner types of mesh points. Their method achieved significantly higher order convergence than other high-order finite difference systems that are already in use, according to a number of test problems. In [39], a generalized modal expansion theory in the context of the physics of wave-matter interaction in bounded and unbounded two-dimensional electromagnetic problems was proposed by Dai, Chew, Lo, Liu, and Jiang. They examined the field response under reduced modal representation. They concluded that a limited number of trapped and radiation modes could approximately describe the fields where the modes are approximated

using the Yee-grid-based finite difference method.

In [96], the pseudospectral modal method, which was introduced by Song and Lu introduced, is a method for electromagnetic wave propagation problems to evaluate leaky waveguide modes. The suggested method excelled the introduced mode matching method with its numerical variations based on Fourier series and finite differences because of its accuracy. Xiaoyu, Cai, Chen, N. Liu, and H. Liu approximated the Maxwell EVP using the mixed spectral element method to obtain eigenmodes for the modal analysis of electromagnetic wave propagation problem in [69]. In [4], the approach proposed by Fonseca and Figueroa is based on a discretization of the vector wave propagation problem using an interior penalty discontinuous Galerkin for the approximation of modes. The approach is spurious-free and accurate by using the appropriate penalty function. The modal analysis of problem in rectangular microwave waveguides, rib waveguides, strip waveguides (leaky mode), and dielectric-loaded surface plasmon-polariton waveguides is perfomed to show the method's accuracy.

The finite element methods for the modal analysis of electromagnetic wave propagation problems are presented in the following. Zghal, Bahloul, Chatta, Attia, Pagnoux, and others applied the modal analysis using the vectorial finite element method and simulated microstructured optical fibers [104]. The modal properties of the simulation with various pitches and hole dimensions have been found over a broad spectral spectrum. They showed that single-mode propagation occurs throughout a wide spectral range. Finally, in [81], when studying modal analysis of photonic waveguides, Orlandini, Figueroa, Devloo, and Oliveira used adaptive high-order edge elements to obtain modes using mixed finite element formulation. The suggested approach was applied to the rib waveguide and compared with those from [4] and [96] to show the efficacy of this study. In [94], Habib and Kordi studied a modal analysis of multiconductor cables on a two-dimensional domain using the finite element method to approximate the resulting EVP to obtain propagation constants and the corresponding distribution of the electromagnetic fields. They demonstrated various numerical experiments to show the method's accuracy in comparing the approximated modes with the reference and analytical results. A modal analysis of the electromagnetic wave propagation problem in anisotropic diffused-channel waveguides is presented by Franco, Passaro, Neto, Cardoso, and Machado [48]. The modes are approxi-

mated by FEM using first-order triangular Lagrange elements. The modal analysis is performed utilizing the obtained approximate eigenvalues in consideration of the refractive index model. In [10], Benbouzid, Reyne, Dérou, and Foggia modeled a synchronous machine using FEM to investigate vibration behavior. They explored this through the resonant frequencies, mode spaces, and electromagnetic force distribution. These considerations are handled using FEM to approximate related EVP and electric and magnetic fields to analyze force distribution.

1.2 Plan of the Thesis

The introduction of Maxwell's equations and the derivation of the three forms, which are the Maxwell source problem, Maxwell EVP, and the electromagnetic wave propagation problem, are presented in Chapter 2. The basics of FEM, the introduction of related spaces, their traces, variational forms, and Nédélec basis functions are given in Chapter 3. The edge-based FEM approximation of Maxwell source and eigenvalue problems, including convergence analysis and numerical results are studied in Chapter 4. Chapter 5 presents a modal analysis of the electromagnetic wave propagation problem using edge-based FEM and FEM in space and FD in time approximation of the electromagnetic wave propagation problem. Finally, Chapter 6 includes a summary of the studies carried out in the thesis.

1.3 Contributions in the Thesis

In this thesis, FEM using the lowest-order Nédélec basis functions is considered to approximate Maxwell's equations in mainly three different configurations: the source problem, the EVP, and the electromagnetic wave propagation problem. As presented in Section 1.1, the edge-based finite element methods are widely employed by many researchers to approximate various configurations of Maxwell's equations because of their well-agreement with the physical characteristics governed by the Maxwell system. Also, it is known that there are available open-source finite element libraries to perform FEM computations using edge elements such as FEniCS [1], FreeFEM [53], and NGSolve [93]. In addition, an introductory material that presents finite el-

ement programming for the electromagnetic problems in MATLAB is given [107]. In the present study, a computational model that performs the edge-based FEM approximations of three different configurations is constructed through programs written in MATLAB in a unified framework. The computational model is established by exploiting MATLAB's linear system solvers, generalized matrix eigenvalue solvers, PDE Toolbox (for mesh generation and visualization), and the library consisting of the construction of Nédélec finite element matrices presented in [6].

As already mentioned, there are ongoing research and development goals in the area of approximating the solutions to the Maxwell equations. Especially, approximating the singular solutions on non-smooth domains is a challenging task. In this thesis, two FEM approximations of the Maxwell EVP are compared in a novel way on the same Powell-Sabin triangulation of a two-dimensional domain that contains a slit and hence with a solution exhibiting a strong singularity. The lowest-order Nédélec basis functions are used for the edge-element solution, whereas the linear Lagrange basis functions with specific properties on the Powell-Sabin triangulations are implemented to obtain the nodal solution. As presented in Section 1.1.1, the convergence properties of the nodal FEM rely on the results established in [19].

Approximating the solution to the electromagnetic wave propagation problem is widely performed using two approaches; the direct time-domain approach, and the modal analysis approach, as detailed in Section 1.1.2 and Section 1.1.3. This thesis also considers the two mentioned methodologies to approximate the wave propagation problem for an electric field derived from Maxwell's equations in the time domain. The two approximations for the electric wave propagation problem are conducted by adopting the approaches used in [33] for a modal analysis technique as well as the FEM in space-FD in time approach in incompressible elastic solids.

In this thesis, the FEM model of the electromagnetic wave propagation problem is obtained by considering the spatial discretization using the lowest-order Nédélec basis functions. Then, it is shown that the solution to the FEM model can be expressed by an expansion with the use of the approximate eigenmodes obtained from the associated Maxwell EVP. The direct time approximation is performed by approximating the second-order temporal derivative using the second-order accurate backward dif-

ference scheme in the FEM model. The modal approximation is obtained by truncating the provided solution given as an expansion of eigenfunctions. These numerical approximations are performed on the wave propagation problem for an electric field. Compared with the provided analytical solution, it is demonstrated that both methods are accurate and agree well with each other.

CHAPTER 2

MAXWELL'S EQUATIONS

2.1 Maxwell's Equations

In [71], James Clark Maxwell modified Ampere's Law for stationary currents, and he combined the following four equations that are given in (2.1) together to formulate a consistent theory to explain electromagnetic phenomena (see, e.g., [60]). Maxwell's equations describe the relationship between the space variables and sources along the electromagnetic field. The electromagnetic field produced by the sources is expressed by the scalar charge density function ρ and the vector current density function $\mathcal{J}$, and is described with field variables electric field intensity, magnetic field intensity, electric displacement, and magnetic induction and denoted by $\mathcal{E},\ \mathcal{H},\ \mathcal{D},\ \mathcal{B}$, respectively. The Maxwell equations are given as

$$\frac{\partial \mathcal{B}}{\partial t} + \nabla \times \mathcal{E} = \mathbf{0}, \tag{2.1a}$$

$$\nabla \cdot \mathcal{D} = \rho, \tag{2.1b}$$

$$\frac{\partial \mathcal{D}}{\partial t} - \nabla \times \mathcal{H} = -\mathcal{J}, \tag{2.1c}$$

$$\nabla \cdot \mathcal{B} = 0. \tag{2.1d}$$

Faraday's law, given in equation (2.1a), states the influence of a magnetic field that varies in time on the electric field. Gauss's electric law gives the charge density's impact on electric displacement (2.1b). The third Maxwell's equation (2.1c) is Ampère's circuital law modified by Maxwell and points out how time-varying electric field and current density function affect the magnetic field. Finally, Gauss's magnetic

law is stated in the equation (2.1d).

Using the fact that $\nabla \cdot (\nabla \times \mathbf{Z}) = 0$ for any vector $\mathbf{Z}$, the divergence condition in (2.1d) becomes a direct result of (2.1a).

The charge conservation holds, if ρ and $\mathcal{J}$ are related by the following

$$\frac{\partial \rho}{\partial t} + \nabla \cdot \mathcal{J} = 0. \tag{2.2}$$

Hence, the divergence condition in (2.1b) is a direct result of (2.1c), provided that charge conservation holds [77].

2.1.1 Constitutive Relations

It is needed to perform reductions in the equations given in (2.1) since there are more unknowns than equations. For this reason, constitutive relations should be considered so that $\mathcal{E}$ is correlated to $\mathcal{D}$, and $\mathcal{H}$ is associated with $\mathcal{B}$. These relations are based on the characteristics of the matter in the electromagnetic field's domain and will be applied to equations (2.1) to be able to focus on the less number of dependent variables. The characteristics of the matter are complicated because they usually are affected not only by the molecular properties of the matter but also by macroscopic aspects such as density and temperature. In addition, there are cases where the characteristics of the material are time-dependent [60]. As the mentioned complications are not the focus of this study, the following constructions are followed from [60] and [77] because it is compatible with the literature that is related to Maxwell's system aimed to analyze using finite elements (see, e.g., [13], [27], [57], [88]).

For the cases where ferroelectric and ferromagnetic materials are disregarded, and the fields are small enough, the constitutive relations are presented in the form of linear equations

$$\mathcal{D} = \epsilon \mathcal{E} \quad \text{and} \quad \mathcal{B} = \mu \mathcal{H}, \tag{2.3}$$

where ϵ and μ are the permittivity and permeability parameters of the material. In this case, the medium (material through which electromagnetic waves propagate) is called linear.

In practice, the prevailing circumstance is that several materials (e.g., copper, air)

fill the electromagnetic field's domain called inhomogeneous material. In isotropic materials, the material properties are independent of the directions; Equation (2.3) is modeled with scalar functions $\epsilon, \mu : \mathbb{R}^3 \to \mathbb{R}$. If the parameters of the material depend on the directions, this case is called anisotropic. In the case of anisotropic materials, $\epsilon : \mathbb{R}^3 \to \mathbb{R}^{3\times3}$ and $\mu : \mathbb{R}^3 \to \mathbb{R}^{3\times3}$ are called the permittivity tensor and permeability tensor, respectively.

Furthermore, the current density $\mathcal{J}$ can also depend on the material and the fields. Thus, an additional relation is required. The electric field generates a current (flow of electric charges) in a conducting material, and Ohm's law describes this as

$$\mathcal{J} = \sigma\mathcal{E} + \mathcal{J}_a, \tag{2.4}$$

where $\mathcal{J}_a$ is the applied current density. The function $\sigma : \mathbb{R}^3 \to \mathbb{R}$ is called the conductivity for an isotropic material. The material is called a conductor if $\sigma > 0$ and is said to be a nonconducting if $\sigma = 0$. In addition, the conductivity of anisotropic material σ is also matrix-valued. In vacuum or free space, $\sigma = 0$ and $\epsilon = \epsilon_0 = 8.854 \times 10^{-12}\text{Fm}^{-1}$, $\mu = \mu_0 = 4\pi \times 10^{-7}\text{Hm}^{-1}$ in the standard SI units [77].

Next, the following Maxwell's equations are obtained by substituting the constitutive relations (2.3) and Ohm's law (2.4) to Equation (2.1) and stated as

$$\frac{\partial(\mu\mathcal{H})}{\partial t} + \nabla \times \mathcal{E} = \mathbf{0}, \tag{2.5a}$$

$$\nabla \cdot (\epsilon\mathcal{E}) = \rho, \tag{2.5b}$$

$$\frac{\partial(\epsilon\mathcal{E})}{\partial t} - \nabla \times \mathcal{H} = -(\sigma\mathcal{E} + \mathcal{J}_a), \tag{2.5c}$$

$$\nabla \cdot (\mu\mathcal{H}) = 0. \tag{2.5d}$$

Note that the problems are considered in linear, isotropic mediums where ϵ, μ in (2.3), and σ in (2.4) are scalar functions.

To work with the less number of dependent variables, $\mathcal{H}$ or $\mathcal{E}$ can be eliminated from the first-order system given (2.5). If $\mathcal{E}$ is eliminated by considering the derivative of (2.5a) with respect to time t and using (2.5c), then the second-order PDE in $\mathcal{H}$ is

obtained that

$$\begin{aligned} \frac{\partial^2(\mu\mathcal{H})}{\partial t^2} + \sigma\frac{\partial(\mu\mathcal{H})}{\partial t} + \nabla\times(\epsilon^{-1}\nabla\times\mathcal{H}) &= -\nabla\times\mathcal{J}_a, \\ \nabla\cdot(\mu\mathcal{H}) &= 0. \end{aligned} \tag{2.6}$$

In this study, the focus is on a second-order PDE in $\mathcal{E}$, which is obtained by taking the derivative of (2.5c) with respect to time t that is resulted as

$$\frac{\partial^2(\epsilon\mathcal{E})}{\partial t^2} + \frac{\partial(\sigma\mathcal{E})}{\partial t} - \nabla\times\frac{\partial\mathcal{H}}{\partial t} = -\frac{\partial\mathcal{J}_a}{\partial t},$$

and using (2.5a), the second-order PDE in $\mathcal{E}$ is given by

$$\begin{aligned} \frac{\partial^2(\epsilon\mathcal{E})}{\partial t^2} + \frac{\partial(\sigma\mathcal{E})}{\partial t} + \nabla\times(\mu^{-1}\nabla\times\mathcal{E}) &= -\frac{\partial\mathcal{J}_a}{\partial t}, \\ \nabla\cdot(\epsilon\mathcal{E}) &= \rho. \end{aligned} \tag{2.7}$$

Moreover, the three configurations of Maxwell's equations are considered on the domains that have perfect electric conductor (PEC) boundaries. The PEC boundary condition is introduced in the following section.

2.2 Perfect Electric Conductor Boundary Condition

Maxwell's equations only hold for the electromagnetic field if the domain has smooth parameter functions ϵ, μ, and σ [60]. When a surface denoted by S splits two homogeneous media, the parameters are piecewise continuous with finite jumps on the surface S. The finite jumps suggest that the fields meet specific requirements on S, where Maxwell's equations hold on both sides. This section contains the particular case, but other conditions on the surface S can be found in [60, 77]. Before deriving the PEC boundary condition, consider Figure 2.1 and let $\mathcal{E}_m$ denote the limiting values of the electric fields as S is approached from region m, where the index $m \in \{1, 2\}$.

The electric field's tangential component must be continuous across S for $\nabla\times\mathcal{E}$ to be well defined. Thus, the following is obtained.

$$\mathbf{n}\times(\mathcal{E}_1 - \mathcal{E}_2) = 0 \ \text{ on } \ S, \tag{2.8}$$

where $\mathbf{n}$ denotes the unit normal pointing from Region 2 to Region 1.

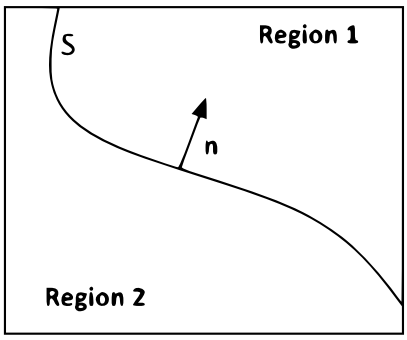


Figure 2.1: Two homogeneous media separated by a surface.

To arrive at the perfect conducting boundary condition, suppose that Region 2 in Figure 2.1 is the perfect conductor. Then, it follows from Ohm's law given in (2.4) that if the current density remains bounded and the conductivity $\sigma \to \infty$, then $\mathcal{E}_2 \to 0$ in (2.8). Therefore, the perfect conducting boundary condition for $\mathcal{E}_1$ is stated as

$$\mathbf{n} \times \mathcal{E}_1 = 0 \ \text{ on } \ S. \tag{2.9}$$

2.3 The Wave Propagation Problem For an Electric Field

The propagation of electromagnetic waves can be described by Equations (2.6) and (2.7), which follow from Maxwell's equations in the time domain. As mentioned earlier, the second-order PDE in $\mathcal{E}$ given in (2.7) is studied in this thesis. Let $\Omega \subset \mathbb{R}^{\{2,3\}}$ be a bounded, simply connected, Lipschitz, polyhedral domain with PEC boundary $\partial\Omega$, and time $t \in [0, T)$. Then, the wave propagation problem for an electric field can be stated as follows:

$$\begin{aligned}
\frac{\partial^2(\epsilon\mathcal{E})}{\partial t^2} + \frac{\partial(\sigma\mathcal{E})}{\partial t} + \nabla \times (\mu^{-1}\nabla \times \mathcal{E}) &= -\frac{\partial \mathcal{J}_a}{\partial t} \ \text{ in } \Omega, \ \text{ for } t \in (0, T), \\
\nabla \cdot (\epsilon\mathcal{E}) &= \rho \ \text{ in } \Omega, \ \text{ for } t \in (0, T), \\
\mathbf{n} \times \mathcal{E} &= 0 \ \text{ on } \partial\Omega, \ \text{ for } t \in (0, T), \\
\mathcal{E}(\mathbf{x}, 0) &= \mathcal{E}_0 \ \text{ in } \Omega, \\
\frac{\partial \mathcal{E}(\mathbf{x}, 0)}{\partial t} &= \dot{\mathcal{E}}_0 \ \text{ in } \Omega,
\end{aligned} \tag{2.10}$$

where $\mathcal{E}_0$ and $\dot{\mathcal{E}}_0$ are given initial conditions.

2.4 Time-Harmonic Maxwell's Equations

The time-harmonic Maxwell system is obtained from the time-dependent problem under the assumptions that the Fourier transforms in time are allowed by the fields and the temporal frequency $\omega > 0$. Hence, for all the variables, the following is considered.

$$\mathcal{V} = \mathcal{R}\Big(\exp(-i\omega t)\hat{\mathbf{V}}(x)\Big), \tag{2.11}$$

in which $\mathcal{V} \in \{\mathcal{E},\ \mathcal{D},\ \mathcal{H},\ \mathcal{B},\ \mathcal{J},\ \mathcal{J}_a,\ \rho\}$, and $\hat{\mathbf{V}} \in \{\hat{\mathbf{E}},\ \hat{\mathbf{D}},\ \hat{\mathbf{H}},\ \hat{\mathbf{B}},\ \hat{\mathbf{J}},\ \hat{\mathbf{J}}_a,\ \hat{\rho}\}$ is the corresponding variable that only has spatial dependence. Also, $i = \sqrt{-1}$ is the complex unit, and $\mathcal{R}(\cdot)$ denotes the real part of the argument. Note that $\mathcal{R}(\cdot)$ exists in (2.11) because the fields $\hat{\mathbf{V}}$ are complex-valued [60], that is $\hat{\mathbf{V}} : \mathbb{R}^3 \to \mathbb{C}^3$.

Then, time-harmonic Maxwell's equations are derived by substituting (2.11) into (2.5) as

$$-i\omega\mu\hat{\mathbf{H}} + \nabla \times \hat{\mathbf{E}} = \mathbf{0}, \tag{2.12a}$$

$$\nabla \cdot (\epsilon\hat{\mathbf{E}}) = \hat{\rho}, \tag{2.12b}$$

$$-i\omega\epsilon\hat{\mathbf{E}} + \sigma\hat{\mathbf{E}} - \nabla \times \hat{\mathbf{H}} = -\hat{\mathbf{J}}_a, \tag{2.12c}$$

$$\nabla \cdot (\mu\hat{\mathbf{H}}) = 0, \tag{2.12d}$$

where the time-harmonic charge density $\hat{\rho}$ in (2.12b) can be eliminated using the relation (2.2) together with Ohm's law given in (2.4), and it follows that

$$\hat{\rho} = \frac{1}{i\omega}\nabla \cdot (\sigma\hat{\mathbf{E}} + \hat{\mathbf{J}}_a). \tag{2.13}$$

For simplicity, it is suitable to work with the following new variables and the relative parameter values followed from [35] given as

$$\mathbf{E} = \epsilon_0^{1/2}\hat{\mathbf{E}} \ \text{ and } \ \mathbf{H} = \mu_0^{1/2}\hat{\mathbf{H}}, \tag{2.14a}$$

Now, considering Equations (2.12) and the definitions given in (2.14a), relative permittivity and permeability are defined in the following.

$$\epsilon_r = \frac{1}{\epsilon_0}\Big(\epsilon + \frac{i\sigma}{\omega}\Big), \ \text{ and } \ \mu_r = \frac{\mu}{\mu_0}. \tag{2.14b}$$

It is important to emphasize that the focus is on the cases where ϵ, μ are scalars and $\sigma = 0$ throughout the study. In these cases, the relative parameters given in (2.14b)

can be restated as follows:

$$\epsilon_r = \frac{\epsilon}{\epsilon_0}, \text{ and } \mu_r = \frac{\mu}{\mu_0}, \tag{2.14c}$$

where ϵ_0 and μ_0 are the vacuum parameters, as introduced earlier. For instance, if the given domain Ω is considered as vacuum ($\epsilon = \epsilon_0$, $\mu = \mu_0$, and $\sigma = 0$), then the relative parameters are $\epsilon_r = \mu_r = 1$. Also, on the dielectric region, the permittivity value is greater than the permittivity of vacuum, that is, $\epsilon > \epsilon_0$ [31]. Therefore, the relative permittivity value given in (2.14c) can be considered $\epsilon_r \geq 1$.

Next, substituting Equations (2.14) into the equations given in (2.12), the following system is obtained:

$$-i\kappa\mu_r\mathbf{H} + \nabla \times \mathbf{E} = 0, \tag{2.15a}$$

$$-i\kappa\epsilon_r\mathbf{E} - \nabla \times \mathbf{H} = -\frac{1}{i\kappa}\mathbf{F}, \tag{2.15b}$$

$$\nabla \cdot (\epsilon_r\mathbf{E}) = -\frac{1}{\kappa^2}\nabla \cdot \mathbf{F}, \tag{2.15c}$$

$$\nabla \cdot (\mu_r\mathbf{H}) = 0, \tag{2.15d}$$

where $\kappa = \omega\sqrt{\epsilon_0\mu_0}$ is the wave number, and $\mathbf{F} = i\kappa\mu^{1/2}\hat{\mathbf{J}}_a$.

In the case of the time-harmonic Maxwell's equations, the system of equations given in (2.15) can also be reduced to one unknown $\mathbf{E}$ or $\mathbf{H}$ by eliminating one of the variables, as it happened in the time-domain. Firstly, $\mathbf{E}$ is eliminated by applying curl ($\nabla\times$) operator to (2.15b) and using (2.15a) to obtain PDE in $\mathbf{H}$ given as

$$\nabla \times (\epsilon_r^{-1}\nabla \times \mathbf{H}) - \kappa^2\mu_r\mathbf{H} = \nabla \times ((i\kappa\epsilon_r)^{-1}\mathbf{F}) \text{ in } \Omega, \tag{2.16a}$$

$$\nabla \cdot (\mu_r\mathbf{H}) = 0 \text{ in } \Omega. \tag{2.16b}$$

Next, $\mathbf{H}$ is eliminated by solving (2.15a) for $\mathbf{H}$ and substituting into (2.15b) to obtain the following second-order PDE given as

$$\nabla \times (\mu_r^{-1}\nabla \times \mathbf{E}) - \kappa^2\epsilon_r\mathbf{E} = \mathbf{F} \text{ in } \Omega, \tag{2.17a}$$

$$\nabla \cdot (\epsilon_r\mathbf{E}) = -\frac{1}{\kappa^2}\nabla \cdot \mathbf{F} \text{ in } \Omega. \tag{2.17b}$$

Equations (2.16) and (2.17) are commonly used in the applications of electromagnetic wave propagation. For instance, some of these applications are scattering from an

object inside a parallel-plate or rectangular waveguide, radiation from a line-source in a parallel-place waveguide, and 3D waveguides with uniform cross-sections [107].

This thesis considers time-harmonic Maxwell's equations in a perfectly conducting cavity to find cavity resonances and corresponding non-zero electric fields, which leads to the Maxwell EVP. Also, the associated source problem called Maxwell's source problem is considered. For these problems Equations (2.17) in $\mathbf{E}$ are studied. Before introducing these problems, note that the PEC boundary condition given in (2.9) also holds for the time-harmonic electric field $\mathbf{E}$ [77], which is given in the form:

$$\mathbf{n} \times \mathbf{E} = 0 \ \text{ on } \ \partial\Omega, \tag{2.18}$$

where $\mathbf{n}$ is the unit outward normal on the boundary $\partial\Omega$ of the given domain Ω.

2.4.1 Time-Harmonic Maxwell's Equations in a Perfectly Conducting Cavity

Time-harmonic Maxwell's equations in a perfectly conducting cavity will be the focused problem in this study. Before continuing to the problem definition, it is important to note that the cavity $\Omega \in \mathbb{R}^d$ $(d = 2, 3)$ is a bounded region isolated from an electromagnetic perspective from the outer region with the PEC boundary denoted by $\partial\Omega$. From the second-order Maxwell's system given in (2.17) with a perfectly conducting cavity domain, the problem is to find the time-harmonic electric field $\mathbf{E}$ corresponding to a given source function $\mathbf{F}$ by solving the following system:

$$\nabla \times (\mu_r^{-1} \nabla \times \mathbf{E}) - \kappa^2 \epsilon_r \mathbf{E} = \mathbf{F} \ \text{ in } \ \Omega, \tag{2.19a}$$

$$\nabla \cdot (\epsilon_r \mathbf{E}) = -\frac{1}{\kappa^2} \nabla \cdot \mathbf{F} \ \text{ in } \ \Omega, \tag{2.19b}$$

$$\mathbf{n} \times \mathbf{E} = 0 \ \text{ on } \ \partial\Omega. \tag{2.19c}$$

There are values of κ such that (2.19a) fails to have a unique solution which is called cavity resonances or Maxwell eigenvalues of Ω [77, 97]. Cavity resonators play an essential role in the microwave and optical systems. They function by causing constructive and destructive wave interference in a confined area. Moreover, they are being used as filters or tools to improve physical interactions, radiation antennas, or electromagnetic sources like magnetrons or lasers. They can also be employed to enhance sensor sensitivity (see, e.g., [45, 72, 87]).

The problem of finding cavity resonances in a perfectly conducting cavity can be written as follows: find cavity resonances κ and non-trivial time-harmonic electric fields $\mathbf{E}$ that satisfies Equation (2.19) with $\mathbf{F} = 0$, such that

$$\nabla \times (\mu_r^{-1} \nabla \times \mathbf{E}) = \kappa^2 \epsilon_r \mathbf{E} \text{ in } \Omega, \tag{2.20a}$$

$$\nabla \cdot (\epsilon_r \mathbf{E}) = 0 \text{ in } \Omega, \tag{2.20b}$$

$$\mathbf{n} \times \mathbf{E} = 0 \text{ on } \partial\Omega. \tag{2.20c}$$

Before considering the Maxwell eigenvalue problem and the source problem, consider a given bounded, simply connected, Lipschitz, polyhedral domain $\Omega \in \mathbb{R}^d$, $d = 2, 3$. The assumptions on the domain are needed conditions for the finite element analysis of the following problems, which will be discussed in Chapter 4.

Naturally, the problem of finding cavity resonances gives rise to the **Maxwell eigenvalue problem** that can be written as follows: find the eigenvalue $\lambda \in \mathbb{R}$ and the eigenfunction $\mathbf{u} \neq 0$ such that

$$\nabla \times (\mu_r^{-1} \nabla \times \mathbf{u}) = \lambda(\epsilon_r \mathbf{u}) \text{ in } \Omega, \tag{2.21a}$$

$$\nabla \cdot (\epsilon_r \mathbf{u}) = 0 \text{ in } \Omega, \tag{2.21b}$$

$$\mathbf{n} \times \mathbf{u} = 0 \text{ on } \partial\Omega. \tag{2.21c}$$

Here, the time-harmonic electric field $\mathbf{E}$ is denoted by $\mathbf{u}$.

Finally, a problem which consists of Equations (2.19) is called **Maxwell's source problem** if κ^2 is not a Maxwell eigenvalue in Ω [77, 78]. The source problem is finding $\mathbf{E}$ corresponding to a given a constant κ^2 and $\mathbf{F}$ such that $\nabla \cdot \mathbf{F} = 0$. Thus, the source problem is considered as follows:

$$\nabla \times (\mu_r^{-1} \nabla \times \mathbf{E}) - \kappa^2 \epsilon_r \mathbf{E} = \mathbf{F} \text{ in } \Omega, \tag{2.22a}$$

$$\nabla \cdot (\epsilon_r \mathbf{E}) = 0 \text{ in } \Omega, \tag{2.22b}$$

$$\mathbf{n} \times \mathbf{E} = 0 \text{ on } \partial\Omega. \tag{2.22c}$$

It is important to note that, following from (2.19b), if $\nabla \cdot \mathbf{F} = 0$, then $\nabla \cdot (\epsilon_r \mathbf{E}) = 0$. The condition of the given source being divergence-free is important to have in the source problem for the unique solution, which will be discussed in Chapter 4.

CHAPTER 3

THE EDGE BASED FINITE ELEMENT METHOD

In this chapter, some background information is provided on the finite element method (FEM), the function spaces, the traces, the variational formulation, Galerkin method, affine transformation, and numerical quadrature that are mainly given in [65, 97]. Specifically, the function space $H(\text{curl})$ where the solutions are sought and the trace of functions in $H(\text{curl})$ are introduced by following [77]. Next, the standard and mixed variational (weak) formulations are presented for the following configurations of Maxwell's equations: the source problem, EVP, and the electric wave propagation problem. The mixed weak formulations of the source and eigenvalue problems are followed from [15, 16, 58]. Moreover, following [6, 24, 77, 80], the lowest-order Nédélec edge elements that are $H(\text{curl})$ conforming are introduced. Furthermore, the Piola mappings are presented as an appropriate mapping for the introduced edge elements because of their continuity-preserving property for the space $H(\text{curl})$.

3.1 The Finite Element Method

The FEM is a widely used numerical method for approximating partial differential equations (PDEs) in engineering and mathematics. The common research areas are fluid flow, analysis of structures, heat transfer, mass transport, and electromagnetic potential.

In general, the FEM follows the following path to approximate PDEs:

i) The variational form of the problem is obtained.

ii) The variational form is discretized by implementing piecewise polynomials as trial functions.

iii) The approximate solution is obtained from the solution of an algebraic form that is followed by the discrete problem.

The formal definition of a finite element is given in the following [97]:

A finite element is a triple $(K, \mathcal{P}, \mathcal{N})$ such that

1. $K \subset \mathbb{R}^n$ is a geometric domain (e.g., triangle, tetrahedron),
2. $\mathcal{P}$ is a space of functions (e.g. polynomials) on K,
3. $\mathcal{N} = \{N_1, \ldots, N_s\}$ is a set of linear functionals on $\mathcal{P}$, called degrees of freedom.

The finite element $(K,\ \mathcal{P},\ \mathcal{N})$ is unisolvent if the degrees of freedom of $\mathcal{N}$ uniquely determine a function in $\mathcal{P}$. Depending on whether the spatial dimension n is 1, 2, or 3, the polygon K is of a different kind. Lines, triangles, quadrilaterals, tetrahedrons, and bricks are the most popular polygons. Each polygon is derived from the domain mesh. For domains with curved bounds, triangles and tetrahedrons work well, while quadrilateral and brick polygons are simple in programming. Prisms are most commonly utilized in domains having cylindrical symmetry, such as pipes [65].

3.2 Function Spaces

The regularity of a PDE's solution affects how effectively it may be approximated numerically. Lebesque integrability and differentiability describe regularity. Function spaces are a collection of functions that have specific differentiability and integrability features that are introduced in the following.

3.2.1 Real Normed and Inner Product Vector Spaces

A real vector space V equipped with a norm is called a real normed vector space. A norm on a vector space V is a mapping $||\cdot|| : V \to \mathbb{R}$ that has the following

properties:

- $||u + v|| \leq ||u|| + ||v||$
- $||au|| = |a|\ ||u||$
- $||u|| \geq 0, u = 0 \iff ||u|| = 0$

for all $u, v \in V$ and $a \in \mathbb{R}$. Additionally, a semi-norm $|\cdot| : V \to \mathbb{R}$ has the properties of a norm with one exception, which is $|u| = 0$ does not need to imply $u = 0$.

On a vector space V, a linear form $L(\cdot) : V \to \mathbb{R}$ satisfies:

- $L(u + v) = L(u) + L(v)$
- $L(au) = aL(u)$

for all $u, v \in V$ and $a \in \mathbb{R}$. $L(\cdot)$ is said to be bounded, if the following is satisfied:

$$|L(v)| \leq C||v||, \quad \forall v \in V, \tag{3.1}$$

where C is a constant. Also, the norm of $L(\cdot)$ is given by

$$||L|| = \sup_{v \in V} \frac{|L(v)|}{||v||}, \quad \forall v \neq 0. \tag{3.2}$$

The **dual space** of V is the set of all continuous functionals on V and is denoted by V^*. It can be shown that the dual space V^* is a linear vector space under the addition and scalar multiplication operations of V. The dual space V^* can be normed by setting $||L||_{V^*} = ||L||$.

A bilinear form on a real vector space V is a mapping $a(\cdot, \cdot) : V \times V \to \mathbb{R}$ such that

- $a(u + v, w) = a(u, w) + a(v, w)$
- $a(a, v + w) = a(u, v) + a(u, w)$
- $a(\zeta u, v) = \zeta\ a(u, v)$
- $a(u, \zeta v) = \zeta\ a(u, v)$

for all $u, v, w \in V$ and ζ is a scalar. The symmetric bilinear form fulfills the following equality, which is given as

$$a(u, v) = a(v, u) \tag{3.3}$$

for all $u, v \in V$. Next, the bilinear form is said to be bounded (continuous), if C is a constant such that

$$|a(u, v)| \leq C||u||||v||, \quad \forall u, v \in V. \tag{3.4}$$

A real vector space equipped with an inner product is called an inner product space. An inner product is a symmetric bilinear form which satisfies the following:

- $a(u, u) \geq 0, \quad a(u, u) = 0 \iff u = 0$

for all $u \in V$. Inner products are denoted by $(\cdot, \cdot)$ and are given as

$$||u||^2 = (u, u). \tag{3.5}$$

Also, inner products define a norm by Equation (3.5) on V. In addition, a bilinear form $a(\cdot, \cdot)$ defines the so called energy norm $|||u|||^2 = a(u, u)$.

3.2.2 Banach and Hilbert Spaces

Before defining Banach and Hilbert spaces, the concept of completeness must be defined.

Let $\{v_m\}_{m=1}^{\infty}$ of elements $v_m \in V$ be a sequence in a normed vector space V, such that for all $\epsilon > 0$, there exists $\tau \in \mathbb{Z}^+$ that satisfies

$$||v_m - v_n|| \leq \epsilon, \quad \text{for } \ m, n \geq \tau, \tag{3.6}$$

then, the sequence $\{v_m\}_{m=1}^{\infty}$ is called a Cauchy sequence.

A sequence $\{v_m\}_{m=1}^{\infty}$ is convergent if there exists $v \in V$ such that for all $\epsilon > 0$, there exists $\tau \in \mathbb{Z}^+$ such that

$$||v - v_m|| \leq \epsilon, \quad \text{for } \ m \geq \tau. \tag{3.7}$$

It can be concluded that a convergent sequence is also a Cauchy sequence. If every Cauchy sequence in a vector space is convergent, then a vector space is said to be

complete. Now, a complete normed vector space is called a Banach space, and a complete inner product vector space is said to be a Hilbert space.

3.2.3 L^p Spaces

The most significant Banach and Hilbert spaces in finite element analysis are vector spaces of functions that come from the spaces L^p.

The function spaces $L^p(\Omega)$ are given by

$$L^p(\Omega) = \{v : \Omega \to \mathbb{R} : ||v||_{L^p(\Omega)} < \infty\}, \tag{3.8}$$

where

$$||v||_{L^p(\Omega)} = \left(\int_\Omega |v|^p dx \right)^{1/p}, \quad 1 \leq p < \infty, \tag{3.9}$$

and

$$||v||_{L^\infty(\Omega)} = \sup_{x \in \Omega} |v(x)|. \tag{3.10}$$

The integral, in this case, is a so-called Lebesgue integral, which permits the integration of a wider range of functions than the conventional Riemann integral. In practice, well-defined point values are not required for these functions. In addition, the function spaces $L^p(\Omega)$ are Banach spaces for all $1 \leq p < \infty$.

3.2.4 Weak Derivatives

The phrase "weak derivative" refers to a definition of the derivative in an average meaning since functions in Hilbert spaces are rarely regular enough for the original understanding of the derivative.

Let $C^k(\Omega)$ be the space of all $k < \infty$ times continuously differentiable functions in Ω and $\mathcal{D}(\Omega)$ be the space of all infinitely differentiable functions that vanish on the boundary of the domain Ω which is called the space of test functions.

Let

$$D^\alpha \varphi = \prod_{i=1}^{d} \left(\frac{\partial}{\partial x_i} \right)^{\alpha_i} \varphi, \quad \varphi \in \mathcal{D}(\Omega) \tag{3.11}$$

denote the classical partial derivative, where $\alpha = (\alpha_1, \alpha_2, \ldots, \alpha_d)$ is a multi-index. Using the partial integration and the fact that boundary terms vanish, the following is obtained:

$$\int_\Omega \frac{\partial u}{\partial x_i}\varphi dx = -\int_\Omega u\frac{\partial \varphi}{\partial x_i}dx, \quad \forall \varphi \in \mathcal{D}(\Omega), \tag{3.12}$$

for any $u \in C^1(\Omega)$. Repeating this formula α times, the following is obtained:

$$\int_\Omega (D^\alpha u)\varphi dx = (-1)^{|\alpha|}\int_\Omega u(D^\alpha \varphi)dx, \quad \forall \varphi \in \mathcal{D}(\Omega), \tag{3.13}$$

for any $u \in C^{|\alpha|}(\Omega)$, where $|\alpha| = \sum_{i=1}^{d} \alpha_i$. Note that the right-hand side requires the strong regularity $u \in C^{|\alpha|}(\Omega)$. Therefore, the space of locally integrable functions is introduced below. When the function is integrable on every compact subset of its domain, then it is called locally integrable, and the space of locally integrable functions are defined as

$$L_{loc}(\Omega) = \{v : v \in L^1(K), \text{ for all compact } K \subset \Omega\}. \tag{3.14}$$

Let $u \in L_{loc}(\Omega)$. If there is a function $g \in L_{loc}(\Omega)$ such that

$$\int_\Omega g\varphi dx = (-1)^{|\alpha|}\int_\Omega u(D^\alpha \varphi)dx, \quad \forall \varphi \in \mathcal{D}(\Omega), \tag{3.15}$$

then the function g is the weak derivative $D^\alpha u$ of the function u.

3.2.5 Sobolev Spaces

In finite element analysis, Sobolev spaces are crucial because they give the norms for dealing with PDE solutions and measuring approximation errors. Let $u \in L_{loc}(\Omega)$ and assume that all weak derivatives $D^\alpha u$ with $|\alpha| \leq k$ exist, where k is a non-negative integer. The Sobolev norm of u is defined by

$$||u||_{W_k^p(\Omega)} = \left(\sum_{|\alpha|\leq k} ||D^\alpha u||^p_{L^p(\Omega)}\right)^{1/p}, \quad 1 \leq p < \infty, \tag{3.16}$$

and

$$||u||_{W_k^p(\Omega)} = \max_{|\alpha|\leq k} ||D^\alpha u||_{L^\infty(\Omega)}, \quad p = \infty. \tag{3.17}$$

Then, the Sobolev space $W_k^p(\Omega)$ is the space of $L^p(\Omega)$ functions u, whose weak derivatives also lies in $L^p(\Omega)$ and defined by

$$W_k^p(\Omega) = \{u \in L_{loc}(\Omega) : ||u||_{W_k^p(\Omega)} < \infty\}. \tag{3.18}$$

The Sobolev spaces are Banach spaces for all $1 \leq p$. However, for $p = 2$ $W_k^2(\Omega)$, is also a Hilbert space which is the most common in finite element analysis. The Hilbert space $W_k^2(\Omega)$ has inner product and norm as:

$$(u, v)_{W_k^2(\Omega)} = \sum_{|\alpha| \leq k} (D^\alpha u, D^\alpha u)_{L^2(\Omega)}, \tag{3.19}$$

$$||u||_{W_k^2(\Omega)} = \sum_{|\alpha \leq k} ||D^\alpha u||^2_{L^2(\Omega)}. \tag{3.20}$$

Also, note that the notation $H^k(\Omega) = W_k^2(\Omega)$ is used to emphasize the Hilbert space property in which $H^k(\Omega)$ denotes the space of functions that kth derivatives and are square-integrable in $L^2(\Omega)$ and is defined as

$$H^k(\Omega) = \{u \in L^2(\Omega) : D^k u \in L^2(\Omega)\}. \tag{3.21}$$

Thus, with $k = 1$, consider the following

$$H^1(\Omega) = \{u \in L^2(\Omega) : D^1 u \in L^2(\Omega)\}, \tag{3.22}$$

where it is induced by an inner product and norm given in the following:

$$(u, v)_{H^1(\Omega)} = (u, v)_{L^2(\Omega)} + (\nabla u, \nabla v)_{L^2(\Omega)}, \tag{3.23}$$

$$||u||^2_{H^1(\Omega)} = ||u||^2_{L^2(\Omega)} + ||\nabla u||_{L^2(\Omega)}. \tag{3.24}$$

Next, the space $H^1(\Omega)$ with homogeneous Dirichlet boundary condition is defined as

$$H_0^1(\Omega) = \{u \in H^1(\Omega) \mid u = 0 \text{ on } \partial\Omega\}. \tag{3.25}$$

The functional space for Maxwell's equations is defined as follows:

$$H(\text{curl}; \Omega) = \{\mathbf{u} \in L^2(\Omega) : \nabla \times \mathbf{u} \in L^2(\Omega)\}, \tag{3.26}$$

with the inner product defined as

$$(\mathbf{u}, \mathbf{v})_{H(\text{curl};\Omega)} = (\mathbf{u}, \mathbf{v}) + (\nabla \times \mathbf{u}, \nabla \times \mathbf{v}), \quad \mathbf{u}, \mathbf{v} \in H(\text{curl}; \Omega), \tag{3.27}$$

which induces a norm $|| \cdot ||_{H(\text{curl};\Omega)}$ on $H(\text{curl}; \Omega)$. Next, the defined functional space with homogeneous Dirichlet boundary condition is described as

$$H_0(\text{curl}; \Omega) = \{\mathbf{u} \in H(\text{curl}; \Omega) \ \mid \ \mathbf{n} \times \mathbf{u} = 0 \ \text{ on } \ \partial\Omega\}. \tag{3.28}$$

Moreover, the following spaces will be helpful in the convergence analysis in the finite element approximation:

$$H(\text{div};\Omega) = \{\mathbf{u} \in L^2(\Omega) \ \mid \ \nabla \cdot \mathbf{u} \in L^2(\Omega)\}, \tag{3.29a}$$

$$H_0(\text{div};\Omega) = \{\mathbf{u} \in H(\text{div};\Omega) \ \mid \ \mathbf{n} \cdot \mathbf{u} = 0 \ \text{ on } \ \partial\Omega\}, \tag{3.29b}$$

$$H(\text{div}^0;\Omega) = \{\mathbf{u} \in H(\text{div};\Omega) \ \mid \ \nabla \cdot \mathbf{u} = 0 \ \text{ in } \ \Omega\}. \tag{3.29c}$$

3.2.6 Traces

It is important to consider features of functions in Sobolev spaces on the boundary $\partial\Omega$ since the Lebesgue integral only defines such functions up to a set of measure zero. If the function is continuous, it can be evaluated directly on the boundary. However, developing an idea for a general Sobolev function is necessary. Trace of the function is a process of making a smooth approximation within the domain and then evaluating this approximation on the border for a general Sobolev function. For instance, any $a \in W_p^1(\Omega)$ can be restricted to $b \in L^p(\partial\Omega)$, and conversely, any $b \in L^p(\partial\Omega)$ can be extended to $a \in W_1^p(\Omega)$ [65]. Furthermore, assume that $\partial\Omega$ is sufficiently regular, and let tr denote the trace operator

$$tr : W_1^p(\Omega) \to L^p(\partial\Omega) \tag{3.30}$$

which is well-defined and satisfying the following Trace inequality

$$||tr(b)||_{L^p(\partial\Omega)} \leq M||b||_{L^p(\Omega)}^{\frac{1-p}{p}} \ ||a||_{W_1^p(\Omega)}^{\frac{1}{p}}, \tag{3.31}$$

where M is a constant.

Now, the trace properties of functions in $H(\text{curl};\Omega)$ are examined following from [77]. Maxwell's equations require the tangential trace of the electric field to be well-defined in a physical sense. For this reason, it must be verified that the functions in $H(\text{curl};\Omega)$ should have a well-defined tangential trace. With this aim, two traces are defined in the following for a smooth function $\mathbf{v} \in C^\infty(\overline{\Omega})$ that are given as

$$tr_t(\mathbf{v}) = \mathbf{v}|_{\partial\Omega} \times \mathbf{n}, \tag{3.32}$$

$$tr_T(\mathbf{v}) = (\mathbf{v}|_{\partial\Omega} \times \mathbf{n}) \times \mathbf{n}, \tag{3.33}$$

where $\mathbf{n}$ is the unit outward normal to Ω.

Next, consider the following Banach space $X(\partial\Omega)$ that is stated as:

$$X(\partial\Omega) = \left\{ f \in H^{-1/2}(\partial\Omega) \mid \exists \mathbf{v} \in H(\text{curl};\Omega) \text{ with } tr(\mathbf{v}) = f \right\}, \tag{3.34}$$

with norm

$$||f||_{X(\partial\Omega)} = \inf_{\mathbf{v}\in H(\text{curl};\Omega),\ tr(\mathbf{v})=f} ||\mathbf{v}||_{H(\text{curl};\Omega)}. \tag{3.35}$$

Finally, consider the following theorem that shows the well-defined tangential trace for the space $H(\text{curl};\Omega)$, which will be used in deriving the variational formulations of Maxwell's equations.

Theorem 3.2.1 (Theorem 3.31, [77])**.** *The space $X(\partial\Omega)$ is a Hilbert space. The trace mapping $tr_t : H(curl;\Omega) \to X(\partial\Omega)$ is surjective. The trace mapping $tr_T : H(curl;\Omega) \to X(\partial\Omega)'$ is well-defined. Moreover, for any $\mathbf{u}, \mathbf{v} \in H(curl;\Omega)$ the following holds:*

$$(\nabla \times \mathbf{u}, \mathbf{v}) - (\mathbf{u}, \nabla \times \mathbf{v}) = \langle tr_t(\mathbf{u}), tr_T(\mathbf{v})\rangle_{\partial\Omega}. \tag{3.36}$$

Therefore, the space $H_0(\text{curl};\Omega)$ can be defined as

$$H_0(\text{curl};\Omega) = \{\mathbf{u} \in H(\text{curl};\Omega) \mid tr_t(\mathbf{u}) = 0\}. \tag{3.37}$$

More details on $H(\text{curl})$ space and the trace of functions in $H(\text{curl})$ can be found in [25, 77].

3.3 Variational Formulation

Variational or weak formulations of boundary value problems are used in finite element methods. A well defined variational formulation must be established before discretizing the Maxwell system. The existence and uniqueness of the solution to a variational problem must be considered before proceeding to approximate the relevant problem. Before that, consider the following definitions of continuity and coercivity of a bilinear form and continuity of a linear form.

Definition 3.3.1 (Continuity and Coercivity of a Bilinear Form)**.** *Let H be a Hilbert space with inner product* $(\cdot,\cdot)$*, and* $a : H \times H \to \mathbb{R}$ *be a bilinear form. If there exists a positive constant* c *such that*

$$|a(u,v)| \leq c||u||_H||v||_H, \quad \forall u,v \in H, \tag{3.38}$$

then the bilinear form is said to be continuous. If there exists a positivte constant c^* *such that*

$$a(u,u) \geq c^*||u||_H^2, \quad \forall u \in H, \tag{3.39}$$

then the bilinear form is said to be coercive on H.

Definition 3.3.2 (Continuity of a Linear Form)**.** *Let* $l(\cdot) : H \to \mathbb{R}$ *be a linear form. If there exists a constant* c *such that*

$$l(v) \leq c||v||_H, \quad \forall v \in H, \tag{3.40}$$

then the linear form is said to be continuous or bounded.

Theorem 3.3.1 (Lax-Milgram Lemma)**.** *Let H be a Hilbert space with inner product* $(\cdot,\cdot)$*, and* $a : H \times H \to \mathbb{R}$ *be a bilinear form, which is continuous (or bounded) and coercive on H, and* $l(\cdot)$ *be a continuous (or bounded) linear form on H. Subsequently, there exists a unique solution* $u \in H$ *to the following abstract variational problem: find* $u \in H$ *such that*

$$a(u,v) = l(v), \quad \forall v \in H. \tag{3.41}$$

The proof of Lax-Milgram Lemma can be found in a standard FEM textbook, e.g., in [65].

3.3.1 Variational Formulations of Maxwell's Equations

The variational (or weak) formulations of the already introduced Maxwell's equations, which are the source problem, EVP, and the electromagnetic wave propagation problem, are presented in this section. These problems are considered in a polyhedral domain $\Omega \subset \mathbb{R}^{\{2,3\}}$ that is bounded, simply connected, and Lipschitz. The standard and mixed weak formulations for three configurations of Maxwell's equations are given. The standard formulation is followed for the computational purposes of

Maxwell's systems, and the mixed formulations are presented for the aim of convergence analysis of FEM using the lowest-order Nédélec edge basis functions. The mixed formulations and the standard formulations are equivalent for both continuous and discrete levels, as stated in [13, 15, 16].

3.3.1.1 Variational Formulations for Maxwell's Source Problem

The standard variational formulation of Maxwell's source problem is obtained by multiplying Equation (2.22a) with the test function $\mathbf{v} \in H_0(\text{curl}; \Omega)$ and using Theorem 3.2.1. Moreover, the equivalent mixed weak formulation is given where it takes its place in the convergence analysis of FEM that is presented in [16].

The variational formulations of Maxwell's source problem (2.22) with the given divergence-free source function $\mathbf{F} \in H(\text{div}^0; \Omega)$ and $\kappa^2 \in \mathbb{R}$ are stated in the following.

1. The standard formulation:

   Find $\mathbf{E} \in H_0(\text{curl}; \Omega)$ such that

   $$(\mu_r^{-1} \nabla \times \mathbf{E}, \nabla \times \mathbf{v}) - \kappa^2 (\epsilon_r \mathbf{E}, \mathbf{v}) = (\mathbf{F}, \mathbf{v}), \quad \forall \mathbf{v} \in H_0(\text{curl}; \Omega). \tag{3.42}$$

2. The mixed formulation:

   Find $(\mathbf{E}, p) \in H_0(\text{curl}; \Omega) \times H_0^1(\Omega)$ such that

   $$\begin{aligned} (\mu_r^{-1} \nabla \times \mathbf{E}, \nabla \times \mathbf{v}) - \kappa^2 (\epsilon_r \mathbf{E}, \mathbf{v}) + (\mathbf{v}, \nabla p) &= (\mathbf{F}, \mathbf{v}), \quad \forall \mathbf{v} \in H_0(\text{curl}; \Omega), \\ (\mathbf{E}, \nabla q) &= 0, \qquad \forall q \in H_0^1(\Omega), \end{aligned} \tag{3.43}$$

where $(\cdot, \cdot)$ denotes the $L^2(\Omega)$ inner product and κ^2 is not a Maxwell eigenvalue [77, 97], and these eigenvalues are obtained by solving the Maxwell eigenvalue problem introduced in (2.21).

3.3.1.2 Variational Formulations for the Maxwell Eigenvalue Problem

The standard and two different mixed variational formulations are presented where these formulations are equivalent on both continuous and discrete levels [13]. The standard variational formulation of Maxwell EVP is obtained as it was performed in the case of the source problem. Next, the equivalent mixed formulation introduced in [58] is presented, which is associated with the source problem's mixed variational formulation. Moreover, another equivalent mixed formulation that is utilized in the convergence analysis of FEM is given following [15].

The variational formulations of Maxwell EVP given in (2.21) are presented in the following.

(1) The standard formulation:

Find $\lambda \in \mathbb{R}$ and $\mathbf{E} \in H_0(\text{curl}; \Omega)$ with $\mathbf{E} \neq 0$ such that

$$(\mu_r^{-1} \nabla \times \mathbf{E}, \nabla \times \mathbf{v}) = \lambda(\epsilon_r \mathbf{E}, \mathbf{v}), \qquad \forall \mathbf{v} \in H_0(curl; \Omega). \tag{3.44}$$

(2) The mixed formulation introduced in [58]:

Find $\lambda \in \mathbb{R}$ and $\mathbf{E} \in H_0(\text{curl}; \Omega)$ with $\mathbf{E} \neq 0$, such that for $p \in H_0^1(\Omega)$,

$$\begin{aligned} (\mu_r^{-1} \nabla \times \mathbf{E}, \nabla \times \mathbf{v}) + (\mathbf{v}, \nabla p) &= \lambda(\epsilon_r \mathbf{E}, \mathbf{v}), \quad \forall \mathbf{v} \in H_0(\text{curl}; \Omega), \\ (\mathbf{E}, \nabla q) &= 0, \qquad\qquad\quad \forall q \in H_0^1(\Omega). \end{aligned} \tag{3.45}$$

(3) The mixed formulation introduced in [15]:

Find $\lambda \in \mathbb{R}$ and $\mathbf{E} \in H_0(\text{curl}; \Omega)$ with $\mathbf{E} \neq 0$, such that for $\mathbf{s} \in H_0(\text{div}^0; \Omega; \mu_r^{1/2})$ with $\mathbf{s} \neq 0$,

$$\begin{aligned} (\epsilon_r \mathbf{E}, \mathbf{v}) - (\mu_r^{-1/2} \nabla \times \mathbf{v}, \mathbf{s}) &= \mathbf{0}, \qquad\quad \forall \mathbf{v} \in H_0(\text{curl}; \Omega), \\ (\mu_r^{-1/2} \nabla \times \mathbf{E}, \mathbf{t}) &= \lambda(\mathbf{s}, \mathbf{t}), \quad \forall \mathbf{t} \in H_0(\text{div}^0; \Omega; \mu_r^{1/2}), \end{aligned} \tag{3.46}$$

where the space $H_0(\text{div}^0; \Omega; \mu_r^{1/2})$ is defined as

$$H_0(\text{div}^0; \Omega; \mu_r^{1/2}) = \{\mathbf{u} \in L^2(\Omega) \mid \nabla \cdot (\mu_r^{1/2} \mathbf{u}) = 0, \text{ and } (\mu_r^{1/2} \mathbf{u}) \cdot \mathbf{n}|_{\partial\Omega} = 0\}.$$

3.3.1.3 Variational Formulation for the Electric Wave Propagation Problem

Consider the electric wave propagation problem (2.10) with the assumption on the charge density as $\rho = 0$ for unity since the interest is on divergence-free fields in this study. Also, considering the relation given in (2.2) and Ohm's law given in (2.4), this assumption leads to the following equation

$$\nabla \cdot (\sigma \mathcal{E} + \mathcal{J}_a) = 0, \tag{3.47}$$

where $\mathcal{J}_a$ is the given applied current density function, and the conductivity σ is a scalar function since the isotropic cases are considered in this study. Also, note that Equation (3.47) leads to divergence-free condition on the given applied current density ($\nabla \cdot \mathcal{J}_a = 0$) when non-conducting material ($\sigma = 0$) is considered. Then, the variational formulation of this problem is obtained by multiplying the first equation in (2.10) with the test function $\mathbf{v} \in H_0(\text{curl}; \Omega)$ and using Theorem 3.2.1. Also, the given initial conditions are projected onto $H_0(\text{curl}; \Omega)$, and the variational formulation of the electric wave propagation problem is stated in the following:
Find $\mathcal{E} \in H_0(\text{curl}; \Omega) \times (0, T)$ for all $\mathbf{v} \in H_0(\text{curl}; \Omega)$ such that

$$\begin{aligned} \Big(\frac{\partial^2(\epsilon\mathcal{E})}{\partial t^2}, \mathbf{v}\Big) + \Big(\frac{\partial(\sigma\mathcal{E})}{\partial t}, \mathbf{v}\Big) + (\mu^{-1}\nabla \times \mathcal{E}, \nabla \times \mathbf{v}) &= \Big(-\frac{\partial \mathcal{J}_a}{\partial t}, \mathbf{v}\Big), \text{ for } t \in (0, T), \\ (\mathcal{E}(\mathbf{x}, 0), \mathbf{v})_{H_0(\text{curl};\Omega)} &= (\mathcal{E}_0, \mathbf{v})_{H_0(\text{curl};\Omega)}, \\ \Big(\frac{\partial \mathcal{E}(\mathbf{x}, 0)}{\partial t}, \mathbf{v}\Big)_{H_0(\text{curl};\Omega)} &= (\dot{\mathcal{E}}_0, \mathbf{v})_{H_0(\text{curl};\Omega)}, \end{aligned} \tag{3.48}$$

where $\mathcal{E}_0$ and $\dot{\mathcal{E}}_0$ are given initial conditions.

3.4 The Galerkin Method

The Galerkin method is the process of converting the variational formulation (continuous operator problem) of the given boundary value problem into a discrete problem. If it is known that the variational form (3.41) has a unique solution $u \in H$ by Lax-Milgram Lemma, the space H_h can be considered, which is a finite-dimensional subspace of H with the basis $\{\Upsilon_1, \Upsilon_2, \ldots, \Upsilon_n\}$ such that $H_h = \text{span}\{\Upsilon_1, \Upsilon_2, \ldots, \Upsilon_n\}$.

Then, $u_h \in H_h$ can be represented as

$$u_h = \sum_{i=1}^{n} \alpha_i \Upsilon_i, \quad \text{for} \quad i = 1, 2, \ldots, n, \tag{3.49}$$

where $\alpha_i \quad \text{for} \quad i = 1, 2, \ldots, n$, are the unknown coefficients to be found using the discrete system obtained by the Galerkin method. Consider the following variational form

$$b(u, v) = l(v), \quad \forall v \in H, \tag{3.50}$$

where $b(\cdot, \cdot)$ is a bilinear form on the Hilbert space H, and l is a bounded (continuous) linear functional on H. On the discrete subspace H_h of H, the variational form becomes

$$b(u_h, v_h) = l(v_h), \quad \forall v_h \in H_h. \tag{3.51}$$

Using the representation of $u_h \in H_h$ given in (3.49), and considering $v_h = \Upsilon_i$, for $i = 1, 2, \ldots, n$ since span$\{\Upsilon_1, \Upsilon_2, \ldots, \Upsilon_n\}$ is basis for H_h; the variational form becomes

$$\sum_{i=1}^{n} \alpha_i b(\Upsilon_i, \Upsilon_j) = l(\Upsilon_j), \quad j = 1, 2, \ldots, n. \tag{3.52}$$

This constructs a system of n linear algebraic equations to find the unknown coefficients $\alpha_i, \quad \text{for} \quad i = 1, 2, \ldots, n$.

3.4.1 Galerkin Orthogonality

It is known that the unique solution $u \in H$ satisfies

$$b(u, v) = l(v), \quad \forall v \in H, \tag{3.53}$$

and in particular,

$$b(u, v_h) = l(v_h), \quad \forall v_h \in H_h, \tag{3.54}$$

since $v_h \in H_h \subset H$. Also, the Galerkin approximation $u_h \in H_h$ satisfies Equation (3.51). Then, the following is obtained by subtracting (3.51) from (3.54):

$$b(u - u_h, v_h) = 0, \quad \forall v_h \in H_h, \tag{3.55}$$

which means that the error $e = u - u_h$ is orthogonal to the discrete space H_h.

Cea's lemma is an abstract "best approximation" result derived from Galerkin orthogonality, and its proof can be found, for instance, in [97].

Theorem 3.4.1 (Cea's Lemma)**.** *Let $u_h \in H_h$ be the solution of the discrete system for a given $H_h \subset H$, and $u \in H$ be the continuous solution. Then;*

$$||u - u_h||_H \leq \frac{c^*}{c} \inf_{v_h \in H_h} ||u - v_h||_H, \tag{3.56}$$

where c^* is the continuity constant and c is the coercivity constant.

3.5 Affine Transformation and Numerical Quadrature

In some cases, such as using first-order nodal Lagrange basis functions for H^1 provides a straightforward calculation of stiffness, mass matrices, and load vector. However, this can not be generalized for higher-order nodal basis functions and some other basis functions, such as edge/face-based basis functions. This prevents the benefit of the FEM's ability to work with more complex geometries. To be able to take the advantage of this ability, affine transformation, and numerical quadrature must be considered. Combining these two concepts enables a straightforward and consistent approach to the elemental assembly process.

To understand the transformation as given in [65], consider the nodal basis function for triangular elements. Suppose that, a triangle K is given with nodes $(x^{(i)}, y^{(i)}), i = 1, 2, \ldots, N$. Refer to K as a global element, and $\hat{K}$ as a reference (local) element. The aim is to use the basis functions Z_j on $\hat{K}$ to define the global element K following the given formulas:

$$x(r, s) = \sum_{i=1}^{N} x^{(i)} Z_i(r, s), \tag{3.57a}$$

$$y(r, s) = \sum_{i=1}^{N} y^{(i)} Z_i(r, s), \tag{3.57b}$$

where (r, s) is a given point in $\hat{K}$. It should be noted that the given formulas provide a mapping between the points (r, s) and corresponding global points (x, y) in K, where global points are parametrized by the local ones.

Furthermore, it is known that a function ϑ on K can be expressed as

$$\vartheta_i(r, s) = \sum_{i=1}^{N} \vartheta_i Z_i(r, s), \tag{3.58}$$

where $\vartheta_i = \vartheta((x^{(i)}, y^{(i)}))$.

The chain rule to differentiate ϑ with respect to r and s is given in the following and is needed for the construction of stiffness matrix.

$$\frac{\partial \vartheta}{\partial x} = \frac{\partial \vartheta}{\partial r}\frac{\partial r}{\partial x} + \frac{\partial \vartheta}{\partial s}\frac{\partial s}{\partial x}, \tag{3.59a}$$

$$\frac{\partial \vartheta}{\partial y} = \frac{\partial \vartheta}{\partial r}\frac{\partial r}{\partial y} + \frac{\partial \vartheta}{\partial s}\frac{\partial s}{\partial y}. \tag{3.59b}$$

Also, this can be shown in the matrix form as

$$\begin{bmatrix} \frac{\partial \vartheta}{\partial x} \\ \frac{\partial \vartheta}{\partial y} \end{bmatrix} = \mathbf{J}^{-1} \begin{bmatrix} \frac{\partial \vartheta}{\partial r} \\ \frac{\partial \vartheta}{\partial s} \end{bmatrix}, \tag{3.60}$$

where $\mathbf{J}$ denotes the Jacobian matrix, which is defined as

$$\mathbf{J} = \begin{bmatrix} \frac{\partial x}{\partial r} & \frac{\partial y}{\partial r} \\ \frac{\partial x}{\partial s} & \frac{\partial y}{\partial s} \end{bmatrix}. \tag{3.61}$$

It is also known that the existence of the inverse of Jacobian depends on the global element's quality, and if there exists an inverse, then the mapping is bijective.

Since integration over the global element K is needed for the calculation of finite element matrices and load vector, the process using the change of variables is represented as follows:

$$\int_K f(x,y)dxdy = \int_{\hat{K}} f(r,s)|\det(\mathbf{J}(r,s))|drds. \tag{3.62}$$

Now, this is where the numerical quadrature takes its place. The integral can be calculated numerically, for example, using Gauss quadrature weights (w_p) and points (r_p, s_p) on the local element $\hat{K}$ which is stated as

$$\int_{\hat{K}} f(r,s)|\det(\mathbf{J}(r,s))|drds = \sum_{p=1}^{N_p} f(r_p,s_p)|\det(\mathbf{J}(r_p,s_p))|, \tag{3.63}$$

where N_p is the number of quadrature points.

In this study, Piola mapping is considered because of the continuity-preserving property for the space $H(\text{curl})$ [24, 77, 91], which followed from the works related to the mappings of edge-based vector basis functions [6, 24, 80, 86, 90, 91].

Vectors between Eulerian and Lagrangian coordinates are mapped by the Piola mapping. The Piola mapping that preserves tangential components is called *covariant*. The covariant Piola mapping is defined in the following.

Definition 3.5.1 (Piola Mapping)**.** *Consider a nondegenerate mapping* $\boldsymbol{P} : \ddot{S} \to S = \boldsymbol{P}(\ddot{S})$ *with Jacobian* $\mathbf{J} = \mathbf{J}(X)$*, where* $X \in \ddot{S} \subset \mathbb{R}^N$*. Then, the mapping* $\mathcal{P}$ *is defined by*

$$\mathcal{P}(\xi) = \xi(\boldsymbol{P}^{-1}), \quad \textit{for } \xi \in H^k(\ddot{S}). \tag{3.64}$$

The covariant Piola mapping $\mathcal{P}^{curl}$ *is defined as*

$$\mathcal{P}^{curl}(\xi) = \mathbf{J}^{-T}\xi(\boldsymbol{P}^{-1}), \quad \textit{for } \xi \in L^2(\ddot{S}). \tag{3.65}$$

Further details on the Piola mapping related to the preferred $H(\text{curl})$ conforming basis functions will be discussed in the following section.

3.6 $H(\text{curl})$ Conforming Linear Edge Elements of Nédélec

As mentioned earlier in Section 1.1, the accuracy and efficiency of Nédélec edge elements for the finite element approximation of Maxwell's equations have been shown by many studies because of their consistency with the physical properties of the problem and ability to produce spurious-free, convergent approximations.

In the construction of $H(\text{curl})$ conforming finite element spaces, local finite elements should be patched together while making a proper matching of degrees of freedom over shared element facets (edge of a triangle or a face or edge of a tetrahedron). More specifically, degrees of freedom that correspond to tangential traces must match the $H(\text{curl})$ conforming discretizations [90]. In this thesis, Maxwell's equations are discretized using $H(\text{curl})$ conforming linear edge elements of Nédélec and will be introduced in the following with the help of the relevant studies [6, 80, 86, 91].

Before the introduction of the linear edge elements of Nédélec, let $\Omega \subset \mathbb{R}^d, d = 2, 3$, be an open, bounded, and connected Lipschitz domain. Also, recall the definition of $H(\text{curl})$ that is given as

$$H(\text{curl}; \Omega) = \{\mathbf{u} \in L^2(\Omega) \mid \nabla \times \mathbf{u} \in L^2(\Omega)\}, \tag{3.66}$$

where $L^2(\Omega)$ is the space of square-integrable functions. The domain Ω is discretized using triangular elements for two-dimensional and tetrahedral elements for three-dimensional problem and the related meshes called T, where the basis functions in finite elements space $V_h \subset H(\text{curl}; \mathsf{T})$ are chosen as linear Nédélec elements.

The global Nédélec basis functions and the global spatial variables are denoted by $\Upsilon(\vec{x})$ and $\vec{x} = (x, y, z)^T$, respectively. The unit triangle (2D) and the unit tetrahedron (3D) are considered as reference elements, and the reference basis functions with the spatial variables are denoted as; $\hat{\Upsilon}(\vec{x})$ and $\hat{\vec{x}} = (\hat{x}, \hat{y}, \hat{z})^T$. Also, the ith edge and the tangential unit vector of the related edge of the reference elements are denoted by $\hat{\mathrm{L}}_i$ and $\hat{t}_{\hat{L}_i}$. Moreover, the degrees of freedom for the reference elements are related to the edges, which is 3 for the unit triangle and 6 for the unit tetrahedron, which can be seen in Figure 3.1 with their numberings. Additionally, the discrete divergence-free condition in Maxwell's equations are automatically satisfied using these basis functions [77]. Since the introductory parts are given related to the linear Nédélec elements, Nédélec basis functions will be introduced in the following.



Figure 3.1: Reference elements: unit triangle and unit tetrahedron with their tangential unit vectors of the numbered edges.

3.6.1 Nédélec Basis Functions on the Reference Triangle

The related finite element $(\hat{\mathcal{K}}, \hat{\mathcal{P}}, \hat{\mathcal{N}})$ is defined as follows [6, 80, 91]:

1. $\hat{\mathcal{K}} \subset \mathbb{R}^2$ is a unit triangle.
2. A space of functions $\hat{\mathcal{P}}$ on $\hat{\mathcal{K}}$ is spanned by: $\begin{pmatrix} 1 \\ 0 \end{pmatrix}, \begin{pmatrix} 0 \\ 1 \end{pmatrix}, \begin{pmatrix} \hat{y} \\ -\hat{x} \end{pmatrix}$.
3. A set of linear functionals $\hat{\mathcal{N}} = \{\hat{N}_1, \hat{N}_2, \hat{N}_3\}$ on $\hat{\mathcal{P}}$, called degrees of freedom

related to each edge of the unit triangle are defined as follows:

$$\hat{N}_i(\hat{\vec{v}}) = \int_{\hat{L}_i} \hat{t}_{\hat{L}_i} \cdot \hat{\vec{v}} ds, \quad i = 1, 2, 3. \tag{3.67}$$

The basis functions on the reference triangle are obtained by the relation $\hat{N}_i(\hat{\Upsilon}_j) = \delta_{ij}$, where δ_{ij} is the Kronecker delta, resulting in

$$\hat{\Upsilon}_1(\hat{\vec{x}}) = \begin{pmatrix} -\hat{y} \\ \hat{x} \end{pmatrix}, \tag{3.68a}$$

$$\hat{\Upsilon}_2(\hat{\vec{x}}) = \begin{pmatrix} -\hat{y} \\ \hat{x} - 1 \end{pmatrix}, \tag{3.68b}$$

$$\hat{\Upsilon}_3(\hat{\vec{x}}) = \begin{pmatrix} 1 - \hat{y} \\ \hat{x} \end{pmatrix}. \tag{3.68c}$$

As mentioned earlier, Piola mapping is used to preserve tangential continuity, and the mapping between global and basis functions on the reference element is stated as follows:

$$\Upsilon(\vec{x})|_{\mathcal{K}} = \mathbf{J}^{-T}\, \hat{\Upsilon}(\mathbf{P}^{-1}(\vec{x})), \tag{3.69a}$$

$$\nabla \times \Upsilon(\vec{x})|_{\mathcal{K}} = \frac{1}{\det(\mathbf{J})} \nabla \times \hat{\Upsilon}(\mathbf{P}^{-1}(\vec{x})). \tag{3.69b}$$

3.6.2 Nédélec Basis Functions on the Reference Tetrahedron

The related finite element $(\hat{\mathcal{K}}, \hat{\mathcal{P}}, \hat{\mathcal{N}})$ is defined as follows [6, 80, 91]:

1. $\hat{\mathcal{K}} \subset \mathbb{R}^3$ is a unit tetrahedron.
2. A space of functions $\hat{\mathcal{P}}$ on $\hat{\mathcal{K}}$ is spanned by:

$$\begin{pmatrix} 1 \\ 0 \\ 0 \end{pmatrix}, \begin{pmatrix} 0 \\ 1 \\ 0 \end{pmatrix}, \begin{pmatrix} 0 \\ 0 \\ 1 \end{pmatrix}, \begin{pmatrix} 0 \\ \hat{z} \\ \hat{y} \end{pmatrix}, \begin{pmatrix} \hat{z} \\ 0 \\ \hat{x} \end{pmatrix}, \begin{pmatrix} \hat{y} \\ \hat{x} \\ 0 \end{pmatrix}.$$

3. A set of linear functionals $\hat{\mathcal{N}} = \{\hat{N}_1, \ldots, \hat{N}_6\}$ on $\hat{\mathcal{P}}$, called degrees of freedom related to the each edge of unit tetrahedron are defined as follows:

$$\hat{N}_i(\hat{\vec{v}}) = \int_{\hat{L}_i} \hat{t}_{\hat{L}_i} \cdot \hat{\vec{v}} ds, \quad i = 1, \ldots, 6. \tag{3.70}$$

Again, the reference basis functions are obtained by the relation $\hat{N}_i(\hat{\Upsilon}_j) = \delta_{ij}$, and are stated as:

$$\hat{\Upsilon}_1(\hat{\vec{x}}) = \begin{pmatrix} 1-\hat{z}-\hat{y} \\ \hat{x} \\ \hat{x} \end{pmatrix}, \quad \hat{\Upsilon}_2(\hat{\vec{x}}) = \begin{pmatrix} \hat{y} \\ 1-\hat{z}-\hat{x} \\ \hat{y} \end{pmatrix}, \tag{3.71a}$$

$$\hat{\Upsilon}_3(\hat{\vec{x}}) = \begin{pmatrix} \hat{z} \\ \hat{z} \\ 1-\hat{y}-\hat{x} \end{pmatrix}, \quad \hat{\Upsilon}_4(\hat{\vec{x}}) = \begin{pmatrix} -\hat{y} \\ \hat{x} \\ 0 \end{pmatrix}, \tag{3.71b}$$

$$\hat{\Upsilon}_5(\hat{\vec{x}}) = \begin{pmatrix} 0 \\ -\hat{z} \\ \hat{y}, \end{pmatrix}, \quad \hat{\Upsilon}_6(\hat{\vec{x}}) = \begin{pmatrix} \hat{z} \\ 0 \\ -\hat{x} \end{pmatrix}. \tag{3.71c}$$

Then, the mapping between global and basis functions on the reference tetrahedrons is given as:

$$\Upsilon(\vec{x})|_{\mathcal{K}} = \mathbf{J}^{-T}\, \hat{\Upsilon}(\mathbf{P}^{-1}(\vec{x})), \tag{3.72a}$$

$$\nabla \times \Upsilon(\vec{x})|_{\mathcal{K}} = \frac{\mathbf{J}}{\det(\mathbf{J})}\, \nabla \times \hat{\Upsilon}(\mathbf{P}^{-1}(\vec{x})). \tag{3.72b}$$

Consider the covariant Piola mappings $\mathbf{P}(\hat{\vec{x}}) : \mathbb{R}^d \to \mathbb{R}^d,\ d = 2, 3$, which can be stated as follows:

$$\mathbf{P}(\hat{\vec{x}}) = B\hat{\vec{x}} + c, \tag{3.73}$$

where the Jacobian of mapping is $\mathbf{J} = B$.

In this case, the vectors defining the triangles or tetrahedrons are the column vectors of $\mathbf{J}$ [6], which are denoted as $\mathbf{t}_i$.

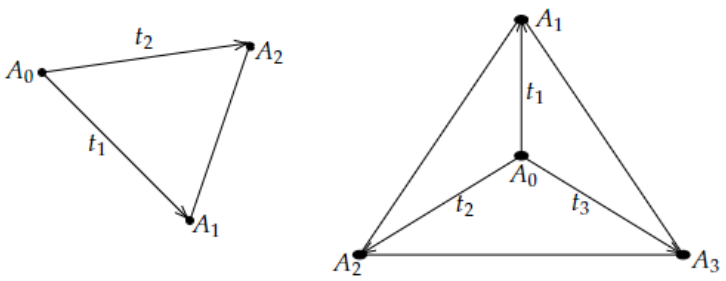


Figure 3.2: The vectors defining the triangle and tetrahedron.

In Figure 3.2, $A_i,\ i = 0, 1, 2$ or $i = 0, 1, 2, 3$ are the vertices of element in the mesh. Then, the vectors defining triangles or tetrahedrons $\mathbf{t}_i$ are obtained as

$$\mathbf{t}_i = A_i - A_0,$$

where $i = 1, 2$ in 2D, and $i = 1, 2, 3$ in 3D. Additionally, vector c in (3.73) is given as

$$c = A_0.$$

Hence, the covariant Piola mappings can be represented as:

$$\mathbf{P}(\hat{\vec{x}}) = \begin{bmatrix} \mathbf{t}_1,\ \mathbf{t}_2 \end{bmatrix} \begin{pmatrix} \hat{x} \\ \hat{y} \end{pmatrix} + \begin{pmatrix} x_0 \\ y_0 \end{pmatrix},\ \text{(2D)},$$

$$\mathbf{P}(\hat{\vec{x}}) = \begin{bmatrix} \mathbf{t}_1,\ \mathbf{t}_2,\ \mathbf{t}_3 \end{bmatrix} \begin{pmatrix} \hat{x} \\ \hat{y} \\ \hat{z} \end{pmatrix} + \begin{pmatrix} x_0 \\ y_0 \\ z_0 \end{pmatrix},\ \text{(3D)}.$$

3.6.3 Global Nédélec Basis Functions

Some components still have to be included in order to acquire the global basis functions. A global basis function has connections to several elements. The local orientation of the degrees of freedom (3.67) is not guaranteed to be the same in different elements. The Nédélec basis functions' orientation must be in the same order to construct functions whose tangential components are continuous at element interfaces [6]. To visualize this situation, consider Figure 3.3, where K_k and K_l are two triangular elements that share an edge in the mesh and let Υ be the global basis function related to that edge.

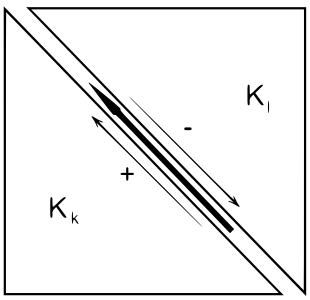


Figure 3.3: Signs of edges of two different triangles that are shared in the mesh (thick line indicates the positive direction that is defined by the user).

To obtain the global basis function Υ on the shared edge, there will be two basis functions $\hat{\Upsilon}_k, \hat{\Upsilon}_l$ that will be transformed from $\hat{\mathcal{K}}$ to K_k, K_l. One can see that in (3.67), unit tangential vectors related to each edge are used to compute the local basis functions. When the transformations given in (3.69) and (3.72) are performed, the tangential components at the edge might be opposite of each other, where it is dependent on the mappings. In particular, if $\det(\mathbf{J}_{K_k}) < 0$, and $\det(\mathbf{J}_{K_l}) > 0$, then the mapping for K_l sustains the counter-clockwise orientation of the reference element, and the mapping for K_k is oriented clockwise in which on the shared edge the orientation is in the same direction and the transformations given in (3.69) and (3.72) are enough for both elements. Otherwise, one of the transformations must be multiplied by -1, since the orientation on the shared edge will be opposite [6]. Therefore, *the transformations for the global basis functions* are demonstrated as follows:

The two and three-dimensional cases:

$$\Upsilon(\vec{x})|_{\mathcal{K}} = [\text{sign}_{\mathcal{K}}^m]\, \mathbf{J}_{\mathcal{K}}^{-T}\ \hat{\Upsilon}_i(\mathbf{P}_{\mathcal{K}}^{-1}(\vec{x})), \tag{3.74a}$$

The two-dimensional case:

$$\nabla \times \Upsilon(\vec{x})|_{\mathcal{K}} = [\text{sign}_{\mathcal{K}}^m]\, \frac{1}{\det(\mathbf{J}_{\mathcal{K}})} \nabla \times \hat{\Upsilon}_i(\mathbf{P}_{\mathcal{K}}^{-1}(\vec{x})), \tag{3.74b}$$

The three-dimensional case:

$$\nabla \times \Upsilon(\vec{x})|_{\mathcal{K}} = [\text{sign}_{\mathcal{K}}^m]\, \frac{1}{\det(\mathbf{J}_{\mathcal{K}})}\ \mathbf{J}_{\mathcal{K}}\ \nabla \times \hat{\Upsilon}_j(\mathbf{P}_{\mathcal{K}}^{-1}(\vec{x})), \tag{3.74c}$$

where the sign datas are related to the two elements as:

$$\begin{aligned}
\left[\text{sign}_{\mathcal{K}_k}^m\right] &= +1,\ \left[\text{sign}_{\mathcal{K}_l}^n\right] = +1, \quad \text{if}\, \det(\mathbf{J}_{\mathcal{K}_k}) > 0,\ \text{and}\ \det(\mathbf{J}_{\mathcal{K}_l}) < 0,\\
\left[\text{sign}_{\mathcal{K}_k}^m\right] &= +1,\ \left[\text{sign}_{\mathcal{K}_l}^n\right] = -1, \quad \text{if}\, \det(\mathbf{J}_{\mathcal{K}_k}) > 0,\ \text{and}\ \det(\mathbf{J}_{\mathcal{K}_l}) > 0,\\
\left[\text{sign}_{\mathcal{K}_k}^m\right] &= -1,\ \left[\text{sign}_{\mathcal{K}_l}^n\right] = +1, \quad \text{if}\, \det(\mathbf{J}_{\mathcal{K}_k}) < 0,\ \text{and}\ \det(\mathbf{J}_{\mathcal{K}_l}) < 0,\\
\left[\text{sign}_{\mathcal{K}_k}^m\right] &= -1,\ \left[\text{sign}_{\mathcal{K}_l}^n\right] = -1, \quad \text{if}\, \det(\mathbf{J}_{\mathcal{K}_k}) < 0,\ \text{and}\ \det(\mathbf{J}_{\mathcal{K}_l}) > 0.
\end{aligned}$$

Note that, m, n are edge indexes for the elements indexed with k, l.

3.6.4 Assembly of Stiffness and Mass Matrices

The stiffness matrix denoted by K is constructed using the introduced Nédélec basis functions as

$$K_{ij} = \int_{\Omega} (\nabla \times \Upsilon_i) \cdot (\nabla \times \Upsilon_j)\, dx, \tag{3.75}$$

where i, j are the global numbering of the edges (degrees of freedom) of a mesh. Moreover, using the introduced Piola transformation, the local matrices using the reference element are assembled. By using the transformations above, the local stiffness matrices related to the global stiffness matrix K are calculated on each element $\mathcal{K} \in \mathsf{T}$ as follows:

The two-dimensional case:

$$K^{\mathcal{K}}_{mn} = \frac{1}{\det(\mathbf{J}_{\mathcal{K}})} \int_{\hat{\mathcal{K}}} ([\text{sign}^m_{\mathcal{K}}]\, \nabla \times \hat{\Upsilon}_m(\mathbf{P}^{-1}_{\mathcal{K}}(\vec{x}))([\text{sign}^n_{\mathcal{K}}]\, \nabla \times \hat{\Upsilon}_n(\mathbf{P}^{-1}_{\mathcal{K}}(\vec{x}))d\hat{\vec{x}}, \tag{3.76}$$

where $m, n \in \{1, 2, 3\}$ in 2D.

The three-dimensional case:

$$K^{\mathcal{K}}_{mn} = \frac{1}{\det(\mathbf{J}_{\mathcal{K}})} \int_{\hat{\mathcal{K}}} ([\text{sign}^m_{\mathcal{K}}]\, \mathbf{J}_{\mathcal{K}} \nabla \times \hat{\Upsilon}_m(\mathbf{P}^{-1}_{\mathcal{K}}(\vec{x})) \cdot ([\text{sign}^n_{\mathcal{K}}]\, \mathbf{J}_{\mathcal{K}} \nabla \times \hat{\Upsilon}_n(\mathbf{P}^{-1}_{\mathcal{K}}(\vec{x}))d\hat{\vec{x}}, \tag{3.77}$$

where $m, n \in \{1, 2, 3, 4, 5, 6\}$ in 3D.

On the other hand, the mass matrix denoted by M is constructed as

$$M_{ij} = \int_{\Omega} \Upsilon_i \cdot \Upsilon_j\, dx, \tag{3.78}$$

where i, j are the global numbering of the edges (degrees of freedom) of a mesh. Then, the global mass matrices $M^{\mathcal{K}}$ are calculated using the introduced Piola mappings as follows:

The two and three-dimensional cases:

$$M^{\mathcal{K}}_{mn} = |\det(\mathbf{J}_{\mathcal{K}})| \int_{\hat{\mathcal{K}}} ([\text{sign}^m_{\mathcal{K}}]\, \mathbf{J}^{-T}_{\mathcal{K}}\, \hat{\Upsilon}_m(\mathbf{P}^{-1}_{\mathcal{K}}(\vec{x}))) \cdot ([\text{sign}^n_{\mathcal{K}}]\, \mathbf{J}^{-T}_{\mathcal{K}}\, \hat{\Upsilon}_n(\mathbf{P}^{-1}_{\mathcal{K}}(\vec{x})))d\hat{\vec{x}}, \tag{3.79}$$

where $m, n \in \{1, 2, 3\}$ in 2D, and $m, n \in \{1, 2, 3, 4, 5, 6\}$ in 3D.

Lastly, a load vector where it might be needed in source problems, and electromagnetic wave propagation problems with given source function f, denoted by b, is calculated on each element $\mathcal{K} \in \mathsf{T}$ as follows:

The two and three-dimensional cases:

$$b_m^{\mathcal{K}} = |\det(\mathbf{J}_{\mathcal{K}})| \int_{\hat{\mathcal{K}}} f \cdot ([\text{sign}_{\mathcal{K}}^m]\, \mathbf{J}_{\mathcal{K}}^{-T}\ \hat{\Upsilon}_m(\mathbf{P}_{\mathcal{K}}^{-1}(\vec{x})))d\hat{\vec{x}}, \tag{3.80}$$

where $m \in \{1, 2, 3\}$ in 2D, and $m \in \{1, 2, 3, 4, 5, 6\}$ in 3D.

3.6.5 Convergence Analysis of FEM

It is known that FEM approximation provides the best approximation in energy norm to the exact solution from Cea's Lemma, where it is already shown that there exists a unique solution of the related variational formulation from Lax-Milgram Lemma. However, it might not be the case when the operator is not elliptic. In that case, the existence and uniqueness of the related weak form's solution can not be shown by Lax-Milgram Lemma. Therefore, the convergence of FEM approximation can not be proved using Cea's Lemma, where it is the case for convergence analysis of FEM for the Maxwell source problem and EVP.

The convergence analyses of edge-based FEM using the lowest-order Nédélec basis functions for the Maxwell source problem and Maxwell EVP are given in the following chapter. The convergence analysis for the case of the source problem is presented by following the study [16] that depends on an approach which uses an abstract setting defining the solutions of the Maxwell source problem and its FEM formulation implicitly via appropriate nonlinear equation. Moreover, the convergence analysis of the FEM approximation of Maxwell EVP is presented following [15], where it follows a similar strategy to the case of the source problem.

CHAPTER 4

FEM APPROXIMATION OF TIME-HARMONIC MAXWELL'S EQUATIONS USING NÉDÉLEC ELEMENTS

This chapter presents the finite element approximations of the Maxwell source problem and Maxwell EVP using the lowest-order Nédélec basis functions. The related convergence analyses are presented following the studies [15, 16]. Some numerical tests will be given to validate the theoretical convergence properties of FEM approximations in Section 4.1.3 and Section 4.2.3.

4.1 Maxwell's Source Problem

This section deals with Maxwell's source problem (2.22) on a bounded, simply connected, Lipschitz, and polyhedral domain $\Omega \subset \mathbb{R}^{\{2,3\}}$ that is stated as a problem of finding the electric field $\mathbf{E}$ such that

$$\begin{aligned} \nabla \times (\mu_r^{-1} \nabla \times \mathbf{E}) - \kappa^2 \epsilon_r \mathbf{E} &= \mathbf{F} \ \text{ in } \ \Omega, \\ \nabla \cdot (\epsilon_r \mathbf{E}) &= 0 \ \text{ in } \ \Omega, \\ \mathbf{n} \times \mathbf{E} &= 0 \ \text{ on } \ \partial\Omega, \end{aligned}$$

where $\mathbf{F} \in H(\text{div}^0; \Omega)$ is the given source function, and κ^2 is the given constant where it is not a Maxwell eigenvalue in Ω.

4.1.1 Finite Element Formulations

The standard and mixed finite element formulations of Maxwell's source problem are obtained by considering the finite-dimensional subspaces $\mathfrak{U}_h \subset H_0(\text{curl};\Omega)$, $\mathfrak{W}_h \subset H_0^1(\Omega)$. The corresponding variational formulations of Maxwell's source problem given in (3.42) and (3.43) are as follows:

1. The standard formulation:

   Find $\mathbf{E}_h \in \mathfrak{U}_h$ such that

   $$(\mu_r^{-1}\nabla \times \mathbf{E}_h, \nabla \times \mathbf{v}_h) - \kappa^2(\epsilon_r \mathbf{E}_h, \mathbf{v}_h) = (\mathbf{F}, \mathbf{v}_h), \quad \forall \mathbf{v}_h \in \mathfrak{U}_h. \tag{4.1}$$

2. The mixed formulation:

   Find $(\mathbf{E}_h, p_h) \in \mathfrak{U}_h \times \mathfrak{W}_h$ such that

   $$\begin{aligned}(\mu_r^{-1}\nabla \times \mathbf{E}_h, \nabla \times \mathbf{v}_h) - \kappa^2(\epsilon_r \mathbf{E}_h, \mathbf{v}_h) + (\mathbf{v}_h, \nabla p_h) &= (\mathbf{F}, \mathbf{v}_h), \qquad \forall \mathbf{v}_h \in \mathfrak{U}_h, \\ (\mathbf{E}_h, \nabla q_h) &= 0, \qquad \forall q \in \mathfrak{W}_h.\end{aligned} \tag{4.2}$$

It is important to note that, in this study, the standard formulation is used for computational purposes. The divergence-free condition is automatically satisfied using the presented Nédélec basis functions in Chapter 3 to construct the finite-dimensional subspace $\mathfrak{U}_h$. The mixed formulation is introduced to conduct the convergence analysis of the approximation following from [16] since, as already stated, both formulations are equivalent at the discrete and continuous levels [13].

4.1.2 Convergence Analysis of the Source Problem

The Maxwell source problem is presented with the relative parameters ϵ_r, μ_r that are already introduced as:

$$\epsilon_r = \frac{1}{\epsilon_0}\Big(\epsilon + \frac{i\sigma}{\omega}\Big) \text{ and } \mu_r = \frac{\mu}{\mu_0}.$$

The convergence analysis of Maxwell's source problem can be performed in two cases. If the conductivity parameter $\sigma > 0$, then the source problem has unique

solution for any $\kappa^2 > 0$ and $\mathbf{F} \in L^2(\Omega)$. In this case, the bilinear form of the source problem is coercive on $H_0(\text{curl}; \Omega)$ and can be analyzed using Cea's Lemma [76].

In this thesis, the values of the conductivity parameter are considered as $\sigma = 0$. In these cases, the problem becomes more complicated since Maxwell's source problem might not have a solution for any value of κ^2. Specifically, if κ^2 is a Maxwell eigenvalue, then the source problem is not well-posed.

The convergence analysis of Maxwell's source problem with $\sigma = 0$ is presented following from [16]. The convergence analysis strategy depends on an approach that utilizes an abstract setting that will define the solutions to the continuous problems and discrete problems implicitly by appropriate nonlinear equations.

Before moving on to the convergence analysis, assume that the given domain $\Omega \subset \mathbb{R}^{\{2,3\}}$, is an open, bounded, Lipschitz, and the relative parameters ϵ_r, μ_r are not discontinuous. Furthermore, assume that the given source function is divergence-free, *i.e.*, $f \in H(\text{div}^0; \Omega)$.

The linear operator $\mathcal{T} : L^2(\Omega) \to L^2(\Omega)$ that is associated to Maxwell's source problem is defined in the following.

Consider the problem of finding $(\mathbf{E}, p) \in H_0(\text{curl}; \Omega) \times H_0^1(\Omega)$ such that

$$\begin{aligned} (\nabla \times \mathbf{E}, \nabla \times \mathbf{v}) + (\mathbf{v}, \nabla p) &= (f, \mathbf{v}), \quad \forall \mathbf{v} \in H_0(\text{curl}; \Omega), \\ (\mathbf{E}, \nabla q) &= 0, \qquad \forall q \in H_0^1(\Omega). \end{aligned} \tag{4.3}$$

Then, the linear operator is defined as $\mathcal{T} f = \mathbf{E} \in L^2(\Omega)$, for all $f \in L^2(\Omega)$, where $\mathbf{E}$ is the first component of the solution to problem (4.3).

Lemma 4.1.1 ((Lemma 1) [16])**.** *The linear operator $\mathcal{T}$ is **compact** and **self-adjoint**.*

Next, the regularity assumption where $\Omega, \mu_r, \epsilon_r$ are assumed and the space that contains the solutions $\mathbf{E}$ to the problem (4.3) is

$$\mathfrak{U} \subseteq H^s(\Omega), \tag{4.4}$$

for some $s > \frac{1}{2}$. This constructs the assumptions on the domain and the material properties, which are satisfied with the above assumptions.

For introducing the discrete operator associated with the discretized source problem, the finite-dimensional subspaces $\mathfrak{U}_h \subset H_0(\text{curl};\Omega)$ and $\mathfrak{W}_h \subset H_0^1(\Omega)$ are considered.

Let $\mathfrak{T}_h$ be triangulation of Ω, and K an element. Let $k \geq 1$ be a fixed integer, and

$$\mathfrak{U}_h = \{v \in H_0(\text{curl};\Omega) \ : \ v|_K \in \mathcal{E}_k(K), \ \ \forall K \in \mathfrak{T}_h\},$$

$$\mathfrak{W}_h = \{q \in H_0^1(\Omega) \ : \ q|_K \in \mathcal{P}_k(K), \ \ \forall K \in \mathfrak{T}_h\},$$

where $\mathcal{P}_k(K)$ is the set of polynomials of degree less than or equal to k on K. The elements of $\mathcal{E}_k(K)$ have the vector valued form. Specifically, these elements are Nédélec elements of the first type.

Then, the discrete operator $\mathcal{T}_h : L^2(\Omega) \to \mathfrak{U}_h$ is defined as follows.

Consider the discrete counterpart of Problem (4.3), which is the problem of finding $(\mathbf{E}_h, p_h) \in \mathfrak{U}_h \times \mathfrak{W}_h$ such that

$$\begin{aligned} (\nabla \times \mathbf{E}_h, \nabla \times \mathbf{v}_h) + (\mathbf{v}_h, \nabla p_h) &= (f, \mathbf{v}_h), \ \ \forall \mathbf{v}_h \in \mathfrak{U}_h, \\ (\mathbf{E}_h, \nabla q_h) &= 0, \qquad \forall q_h \in \mathfrak{W}_h, \end{aligned} \tag{4.6}$$

where the discrete operator is defined as $\mathcal{T}_h f = \mathbf{E}_h \in \mathfrak{U}_h$, for all $f \in L^2(\Omega)$, where $\mathbf{E}_h$ is the first component of the solution to problem (4.6).

The error estimate for the solutions to Problems (4.3) and (4.6) is given in the following proposition.

Proposition 4.1.2 ((Proposition 2) [16])**.** *Assume that (4.4) is fulfilled and that $f \in H(div^0;\Omega)$. Let $\mathbf{E} \in H_0(curl;\Omega)$ and $\mathbf{E}_h \in \mathfrak{U}_h$ be the first components of the solutions of (4.3) and (4.6), respectively. Then*

$$||\mathbf{E} - \mathbf{E}_h||_0 \leq Ch^s||f||_0,$$

where $||.||_0$ denotes the $L^2(\Omega)$ norm.

Moreover, the uniform convergence of the discrete operator $\mathcal{T}_h$ to $\mathcal{T}$ follows from the convergence of eigenmodes of $\mathcal{T}_h$ to eigenmodes of $\mathcal{T}$, since $\mathcal{T}$ is compact and self-adjoint [16]. Then, the the uniform convergence of $\mathcal{T}_h$ to $\mathcal{T}$ is obtained, which is

$$\lim_{h\to 0} ||\mathcal{T} - \mathcal{T}_h||_0 = 0. \tag{4.7}$$

Now the appropriate nonlinear equation that defines the solution to Maxwell's source problem is given as

$$\mathbf{E} + \mathcal{T} M(\kappa^2, \mathbf{E}) = 0, \tag{4.8}$$

where $\Gamma \subset \mathbb{R}$ is a compact interval, and a C^1 mapping $M : \Gamma \times L^2(\Omega) \to L^2(\Omega)$ is

$$M(\nu, u) = -\nu u - f.$$

Then, the discretization of (4.8) is

$$\mathbf{E}_h + \mathcal{T}_h M(\kappa^2, \mathbf{E}_h) = 0. \tag{4.9}$$

Finally, for the convergence of FEM approximation, the theorem given in the following provides the conclusion carried out in [16].

Theorem 4.1.3 ((Theorem 2) [16])**.** *Suppose that regularity assumption (4.4) is satisfied and let Γ be a closed interval contained in the resolvent set of $\mathcal{T}$. Then for h small enough, there exists a unique C^1 mapping $\kappa^2 \longmapsto \mathbf{E}_h(\kappa^2)$ from Γ to $\mathfrak{U}_h$ such that $\forall \kappa^2 \in \Gamma$*

$$\mathbf{E}_h(\kappa^2) + \mathcal{T}_h M(\kappa^2, \mathbf{E}_h(\kappa^2)) = 0. \tag{4.10}$$

In particular, $\forall \kappa^2 \in \Gamma$, there exists a unique solution $\mathbf{E}_h$ of (4.2) with the following error estimate

$$||\mathbf{E}(\kappa^2) - \mathbf{E}_h(\kappa^2)||_0 \leq C h^s. \tag{4.11}$$

4.1.3 Numerical Results of Maxwell's Source Problem

The numerical results are presented in this section for Maxwell's source problem using the finite element method with the lowest order Nédélec basis functions in a square domain $\Omega = [0, \pi]^2$ with $\epsilon_r = \mu_r = 1$. Consider the Maxwell source problem introduced at (2.22) and stated as follows:

$$\begin{aligned} \nabla \times (\nabla \times \mathbf{E}) - \kappa^2 \mathbf{E} &= \mathbf{F} \ \text{ in } \ \Omega, \\ \nabla \cdot (\mathbf{E}) &= 0 \ \text{ in } \ \Omega, \\ \mathbf{n} \times \mathbf{E} &= 0 \ \text{ on } \ \partial\Omega, \end{aligned}$$

where $\mathbf{F} = -(2\sin(y), 2\sin(x))^T \in H(\text{div}^0; \Omega)$ is the given source function. The constant κ^2 is given as $\kappa^2 = 3$, which is not a Maxwell eigenvalue, as will be shown

in Section 4.2.3.1. Then, the exact solution denoted by $\mathbf{E}_{\text{exact}}$ is introduced as $\mathbf{E}_{\text{exact}} = (\sin(y), \sin(x))^T$.

The standard finite element formulation for the presented source problem is stated as follows:

Find $\mathbf{E}_h \in \mathfrak{U}_h$ such that

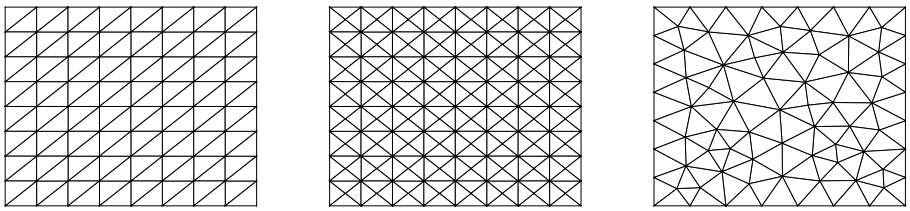
$$(\nabla \times \mathbf{E}_h, \nabla \times \mathbf{v}_h) - 3(\mathbf{E}_h, \mathbf{v}_h) = (\mathbf{F}, \mathbf{v}_h), \quad \forall \mathbf{v}_h \in \mathfrak{U}_h, \tag{4.12}$$

where $\mathbf{E}_h = \sum_{i=1}^{n_e} u_i \Upsilon_i$, and Υ_i are the global Nédélec basis functions that are related to the edge i with the degrees of freedom n_e after imposing Dirichlet boundary condition. Then, the finite element formulation leads to solving the following linear system for u, which contains the coefficients that control the tangential field over the related edge.

$$(\mathbf{K} - 3\mathbf{M})u = \mathbf{b}. \tag{4.13}$$

Here $\mathbf{K}$ is the stiffness matrix introduced in (3.76), $\mathbf{M}$ is the mass matrix introduced in (3.79), and $\mathbf{b}$ is the load vector introduced in (3.80).

The mentioned calculations are performed using the given exact solution together with the approximated ones on a sequence of uniform, unstructured, and criss-cross meshes that are presented in Figure 4.1.



(a) level 1 (b) level 1 (c) level 1

Figure 4.1: Uniform, criss-cross, and unstructured meshes of the square domain.

A comparison of the exact solution and the numerical solution is provided in Table 4.1

in terms of the errors defined as:

$$L^2 - \text{Error} := \Big(\int_\Omega (\mathbf{E}_{exact} - \mathbf{E}_h)^2 dx \Big)^{1/2}.$$

$$H(\text{curl}) - \text{Error} := \Big(\int_\Omega ((\nabla \times \mathbf{E}_{exact}) - (\nabla \times \mathbf{E}_h))^2 dx \Big)^{1/2} + \Big(\int_\Omega (\mathbf{E}_{exact} - \mathbf{E}_h)^2 dx \Big)^{1/2}.$$

$$H(\text{curl}) - \text{Seminorm Error} := \Big(\int_\Omega ((\nabla \times \mathbf{E}_{exact}) - (\nabla \times \mathbf{E}_h))^2 dx \Big)^{1/2}.$$

Also, the convergence rates CR_i are calculated as

$$CR_i = \frac{\ln \mathrm{e}_{i-1} - \ln \mathrm{e}_i}{\ln \mathrm{h}_{i-1} - \ln \mathrm{h}_i}, \ i = 2, 3, 4,$$

where i is the index of mesh refinement levels, e_i is the error between the approximate and exact solution when the mesh's maximum edge length is h_i.

Table 4.1: Errors and convergence rates in the L^2-norm, $H(\text{curl})$-norm, and $H(\text{curl})$-seminorm for different meshes in square domain $[0, \pi]^2$.

Mesh	level	DOF	L^2-Error	$H(\text{curl})$-Error	$H(\text{curl})$-Seminorm Error
Uniform	1	176	0.354136 -	0.420298 -	0.226359 -
	2	736	0.177813 (0.99)	0.210351 (1.00)	0.112384 (1.01)
	3	3008	0.089002 (1.00)	0.105205 (1.00)	0.056094 (1.00)
	4	12160	0.044513 (1.00)	0.052606 (1.00)	0.028035 (1.00)
Criss-Cross	1	368	0.178125 -	0.271904 -	0.205435 -
	2	1504	0.089041 (1.00)	0.135990 (1.00)	0.102785 (1.00)
	3	6080	0.044518 (1.00)	0.068000 (1.00)	0.051401 (1.00)
	4	24448	0.022259 (1.00)	0.034000 (1.00)	0.025702 (1.00)
Unstructured	1	159	0.301497 -	0.425932 -	0.300862 -
	2	799	0.135968 (1.03)	0.194824 (1.01)	0.139532 (0.99)
	3	2889	0.073262 (1.01)	0.102786 (1.04)	0.072094 (1.08)
	4	11832	0.036166 (1.02)	0.051041 (1.01)	0.036016 (1.00)

As presented in the convergence analysis (see Theorem 4.1.3), the expected convergence rate is uniform, matching with the numerical results presented in Table 4.1.

The plots of approximated and exact solutions are presented in Figure 4.2 and Figure 4.3, where the approximated solution is obtained on the criss-cross mesh (level 4).

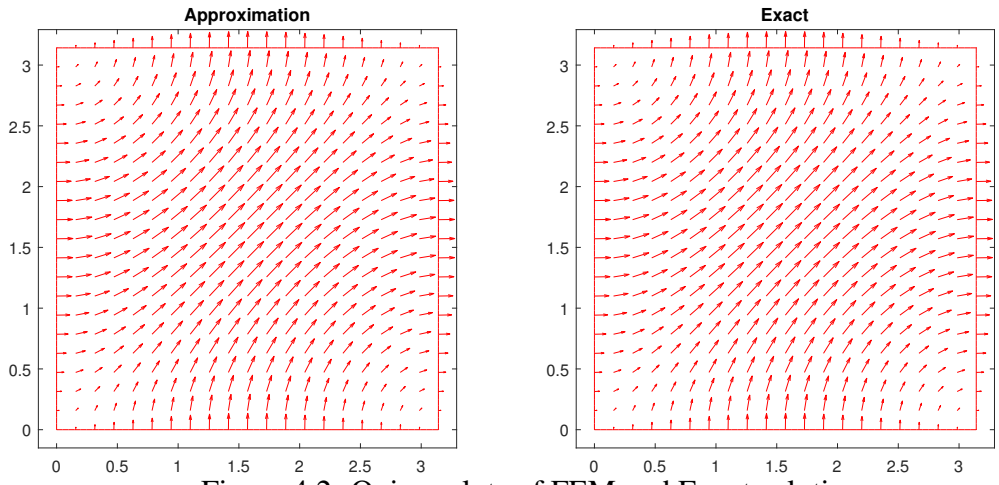
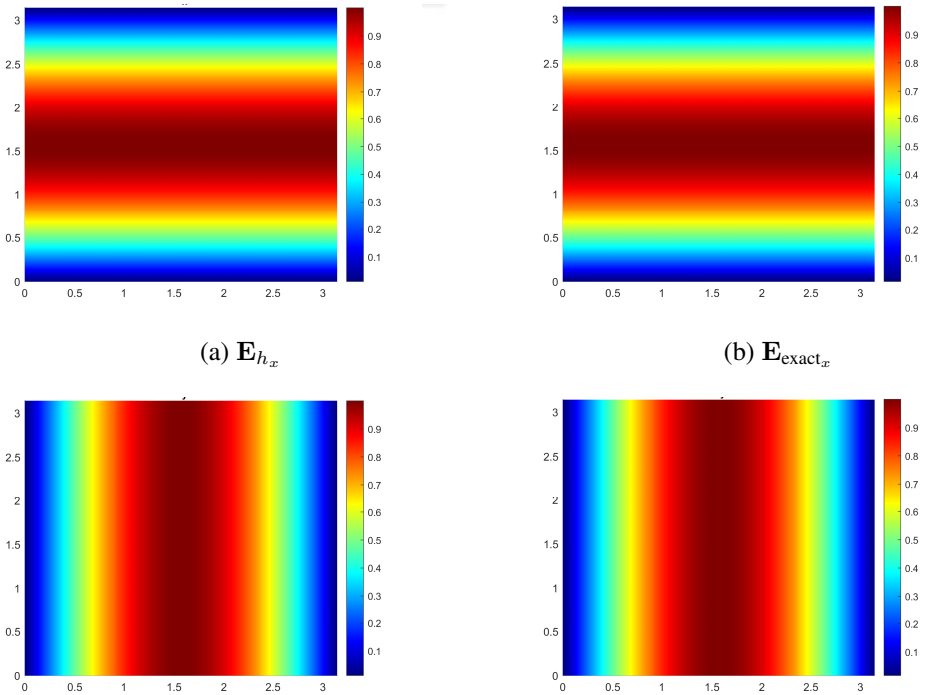


Figure 4.2: Quiver plots of FEM and Exact solutions.

In Figure 4.2, the approximated and exact electric fields are shown using the quiver plot that shows the vector lines as arrows. From this figure it can be easily seen that the vectors directions of the approximate and exact solutions agree well with each other. Moreover, the contours of each component of the electric fields are presented in Figure 4.3, from which a well agreement is also observed.



(a) $\mathbf{E}_{h_x}$ (b) $\mathbf{E}_{\text{exact}_x}$

(c) $\mathbf{E}_{h_y}$ (d) $\mathbf{E}_{\text{exact}_y}$

Figure 4.3: Contours of FEM and Exact solutions.

4.2 The Maxwell EVP

This section presents the results concerning the Maxwell EVP (2.21) on a bounded, simply connected, Lipschitz, and polyhedral domain $\Omega \subset \mathbb{R}^{\{2,3\}}$ that is stated as a problem of finding $\lambda \in \mathbb{R}$ and $\mathbf{u} \neq 0$ such that

$$\nabla \times (\mu_r^{-1} \nabla \times \mathbf{u}) = \lambda(\epsilon_r \mathbf{u}) \text{ in } \Omega,$$

$$\nabla \cdot (\epsilon_r \mathbf{u}) = 0 \text{ in } \Omega,$$

$$\mathbf{n} \times \mathbf{u} = 0 \text{ on } \partial\Omega.$$

As mentioned earlier, standard formulations are preferred to be employed in the computation of approximations. The reason and the results of choosing the standard formulation for the approximation of Maxwell EVP are presented in the following.

Consider the following variational formulation of Maxwell EVP for finding $\lambda \in \mathbb{R}$ and $\mathbf{u} \in H_0(\text{curl}; \Omega) \cap H(\text{div}^0; \Omega)$ such that $\mathbf{u} \neq 0$,

$$(\mu_r^{-1} \nabla \times \mathbf{u}, \nabla \times \mathbf{v}) = \lambda(\epsilon_r \mathbf{u}, \mathbf{v}), \qquad \forall \mathbf{v} \in H_0(\text{curl}; \Omega) \cap H(\text{div}^0; \Omega). \tag{4.15}$$

A countable set of real and positive eigenvalues are admissible in the problem (4.15), and each eigenspace is finite-dimensional. It is because of the fact that the bilinear form $(\mu_r^{-1} \nabla \times \mathbf{u}, \nabla \times \mathbf{v})$ is continuous, symmetric, and coercive on the space $H_0(\text{curl}; \Omega) \cap H(\text{div}^0; \Omega)$ (see, e.g., [46, 50]) and to the compact embedding of $H_0(\text{curl}; \Omega) \cap H(\text{div}^0; \Omega)$ in $L^2(\Omega)$, also the operator associated with problem (4.15) is compact and self-adjoint [15].

Furthermore, assume that $\lambda = 0$, then taking $\mathbf{v} = \mathbf{u}$ in (4.15) implies $(\mu_r^{-1} \nabla \times \mathbf{u}, \nabla \times \mathbf{u}) = 0$, that is $\nabla \times \mathbf{u} = 0$. Moreover, since $\mathbf{u} \in H_0(\text{curl}; \Omega) \cap H(\text{div}^0; \Omega)$ and Ω is simply connected, $\nabla \times \mathbf{u} = 0$ implies $\mathbf{u} = 0$. Thus, $\lambda = 0$ is not an eigenvalue of (4.15). Moreover, considering the case $\lambda \neq 0$, then (2.21b) becomes a consequence of (2.21a). For this reason, the constraint (2.21b) can be dropped, and, equivalently, it is possible to seek $\mathbf{u} \in H_0(\text{curl}; \Omega)$ in problem (4.15). However, by doing this, $\lambda = 0$ is included to the operator's spectrum, and the corresponding space is infinite-dimensional coinciding with $H_0(\text{curl}^0; \Omega) = \nabla H_0^1(\Omega)$ [13]. In addition, the operator's compactness and the related eigensolution's physical meaning

are lost. However, the eigensolutions associated with $\lambda \neq 0$ remain unchanged. For this reason, the standard formulation is preferred in the computation of the Maxwell eigenvalue problem since it is easy to ignore the zero eigenvalues, and associated eigenvectors. Also, the numerical treatment of the constraint (2.21b) and the construction of the finite element space for $H_0(\text{curl};\Omega) \cap H(\text{div}^0;\Omega)$ are difficult.

4.2.1 The Finite Element Formulations

The standard and mixed finite element formulations of the Maxwell EVP are obtained by considering the finite-dimensional subspaces $\mathfrak{U}_h \subset H_0(\text{curl};\Omega)$, $\Sigma_h \subset H_0(\text{div}^0;\Omega;\mu_r^{1/2})$, and the corresponding variational formulations of Maxwell EVP problem that are stated in (3.44) and (3.46).

(1) The standard formulation: find $\lambda_h \in \mathbb{R}$ and $\mathbf{u}_h \in \mathfrak{U}_h \subset H_0(\text{curl};\Omega)$ with $\mathbf{u}_h \neq 0$ such that

$$(\mu_r^{-1}\nabla \times \mathbf{u}_h, \nabla \times \mathbf{v}_h) = \lambda_h(\epsilon_r \mathbf{u}_h, \mathbf{v}_h), \qquad \forall \mathbf{v}_h \in \mathfrak{U}_h, \tag{4.16}$$

(2) The mixed formulation introduced in [15]: find $\lambda_h \in \mathbb{R}$ and $\mathbf{u}_h \in \mathfrak{U}_h \subset H_0(\text{curl};\Omega)$ with $\mathbf{u}_h \neq 0$, such that for $\mathbf{s}_h \in \Sigma_h \subset H_0(\text{div}^0;\Omega;\mu_r^{1/2})$,

$$\begin{aligned} (\epsilon_r \mathbf{u}_h, \mathbf{v}_h) - (\mu_r^{-1/2}\nabla \times \mathbf{v}_h, \mathbf{s}_h) &= \mathbf{0}, & \forall \mathbf{v}_h \in \mathfrak{U}_h, \\ (\mu_r^{-1/2}\nabla \times \mathbf{u}_h, \mathbf{t}_h) &= \lambda_h(\mathbf{s}_h, \mathbf{t}_h), & \forall \mathbf{t}_h \in \Sigma_h, \end{aligned} \tag{4.17}$$

4.2.2 Convergence Analysis of the Maxwell EVP

The convergence analysis of the mixed Maxwell EVP formulation given in (4.17) is presented. In [15], the discrete equivalence of the mixed formulation (4.17) and the standard formulation (4.16) is shown, and the convergence properties are analyzed by utilizing the spectral theory with the associated source problem.

The discrete equivalence between the finite element formulations (4.16) and (4.17) is followed from Theorem 4.2.1.

Theorem 4.2.1 ((Theorem 2.1) [15]). *If $(\lambda_h, \mathbf{u}_h) \in \mathbb{R} \times \mathfrak{U}_h$, with $\lambda_h \neq 0$ is an eigensolution of the problem (4.16), then there exists $\mathbf{s}_h \in \Sigma_h$ such that $(\lambda_h, \mathbf{u}_h, \mathbf{s}_h)$ is an eigensolution of problem (4.17). Also, the converse holds.*

Next, the abstract setting on bilinear forms and operators are given in the following. These will be useful to prove the convergence of FEM employed in this study.
Let A, B be Hilbert spaces and $\mathfrak{a}(\cdot,\cdot) : A \times A \to \mathbb{R}$, $\mathfrak{b}(\cdot,\cdot) : A \times B \to \mathbb{R}$ be bilinear forms, which are continuous. Assume that the symmetric bilinear form $\mathfrak{a}(\cdot,\cdot)$ satisfies

$$\begin{aligned} &\mathfrak{a}(\mathbf{v},\mathbf{v}) \geq 0 \qquad \forall \mathbf{v} \in A, \\ &\mathfrak{a}(\mathbf{v},\mathbf{v}) \geq \alpha ||\mathbf{v}||_A^2 \quad \forall \mathbf{v} \in \mathbb{A}, \end{aligned} \tag{4.18}$$

where $\mathbb{A} = \{\mathbf{v} \in A : \mathfrak{b}(\mathbf{v},\mathbf{t}) = 0 \ \ \forall \mathbf{t} \in B\}$. Following the given bilinear forms, the eigenvalue problem is stated in the following: Find $\lambda \in \mathbb{C}$, and non-zero $(\mathbf{u},\mathbf{s}) \in A \times B$:

$$\begin{aligned} &\mathfrak{a}(\mathbf{u},\mathbf{v}) + \mathfrak{b}(\mathbf{v},\mathbf{s}) = 0, \qquad \forall \mathbf{v} \in A, \\ &\mathfrak{b}(\mathbf{u},\mathbf{t}) = -\lambda(\mathbf{s},\mathbf{t})_B, \qquad \forall \mathbf{t} \in B. \end{aligned} \tag{4.19}$$

The source problem that associates with the eigenvalue problem (4.19) can be introduced as follows:

$$\begin{aligned} &\mathfrak{a}(\mathbf{u},\mathbf{v}) + \mathfrak{b}(\mathbf{v},\mathcal{T}f) = 0, \qquad \forall v \in A, \\ &\mathfrak{b}(\mathbf{u},\mathbf{t}) = -(f,\mathbf{t})_B, \qquad \forall \mathbf{t} \in B, \end{aligned} \tag{4.20}$$

where $\mathcal{T} : B \to B$ is a self-adjoint and compact operator, which associates with every $f \in B$ and $\mathcal{T}f \in B$ is the solution to the problem (4.20).

In particular, it is assumed that (4.20) has a unique solution for all $f \in B$. In this case, the estimate stated in the following holds:

$$||(\mathbf{u},\mathcal{T}f)||_{A\times B} \leq C||f||_B. \tag{4.21}$$

If the construction and assumptions on $\mathfrak{a}(\cdot,\cdot)$ are considered, then all eigenvalues of (4.19) are positive and real. Additionally, noting the compactness of $\mathcal{T}$, consequently, the problem (4.19) leads to a countable set of eigenvalues with multiplicity m_i on each of them, which can be ordered as

$$0 < \lambda_1 < \lambda_2 < \cdots < \lambda_n < \ldots. \tag{4.22}$$

After the continuous framework, to move on to the discrete case, considering the finite-dimensional subspaces $A_h \subseteq A$ and $B_h \subseteq B$, the finite element discretization

of the problem (4.19) is derived as:
Find $\lambda_h \in \mathbb{R}$, and $(\mathbf{u}_h, \mathbf{s}_h) \neq 0 \in A_h \times B_h$ such that

$$\begin{aligned} \mathfrak{a}(\mathbf{u}_h, \mathbf{v}_h) + \mathfrak{b}(\mathbf{v}_h, \mathbf{s}_h) &= 0, \qquad \forall \mathbf{v}_h \in A_h, \\ \mathfrak{b}(\mathbf{u}_h, \mathbf{t}_h) &= -\lambda(\mathbf{s}_h, \mathbf{t}_h)_B, \qquad \forall \mathbf{t}_h \in B_h. \end{aligned} \tag{4.23}$$

Note that the eigenvalues of problem (4.23) are denoted by $0 < \lambda_{h,1} < \lambda_{h,2} < \cdots < \lambda_{h,N} < \ldots$, and N is the dimension of B_h.

Then, the source problem associated with (4.23) is:

$$\begin{aligned} \mathfrak{a}(\mathbf{u}_h, \mathbf{v}_h) + \mathfrak{b}(\mathbf{v}_h, \mathcal{T}_h f) &= 0, \qquad \forall \mathbf{v}_h \in A_h, \\ \mathfrak{b}(\mathbf{u}_h, \mathbf{t}_h) &= -(f, \mathbf{t}_h)_B, \qquad \forall \mathbf{t}_h \in B, \end{aligned} \tag{4.24}$$

where $\mathcal{T}_h : B \to B_h \subset B$ is the discrete operator such that $\mathcal{T}_h f$ is the solution to the problem (4.24).

Problem (4.24) can be solved uniquely if the followings are satisfied:

$$\mathfrak{a}(\mathbf{u}_h, \mathbf{u}_h) \geq \alpha_h ||\mathbf{u}_h||_A^2, \qquad \forall \mathbf{u}_h \in \mathbb{A}_h, \tag{4.25}$$

$$\inf_{\mathbf{t}_h \in B_h} \sup_{\mathbf{v}_h \in A_h} \frac{|\mathfrak{b}(\mathbf{v}_h, \mathbf{t}_h)|}{||\mathbf{t}_h||_B ||\mathbf{v}_h||_A} \geq \beta_h > 0, \tag{4.26}$$

where $\mathbb{A}_h = \{\mathbf{v}_h \in A_h \ : \ \mathfrak{b}(\mathbf{v}_h, \mathbf{t}_h) = 0 \ \ \forall \mathbf{t}_h \in B_h\}$.
Additionally, from [24], if

$$\alpha_h \geq \alpha_0 > 0, \tag{4.27}$$

$$\beta_h \geq \beta_0 > 0, \tag{4.28}$$

uniformly in h, and if

$$\lim_{h \to 0} \Big(\inf_{\mathbf{v}_h \in A_h} ||\mathbf{u} - \mathbf{v}_h||_A + \inf_{\mathbf{t}_h \in B_h} ||\mathbf{s} - \mathbf{t}_h||_B \Big) = 0, \qquad \forall \mathbf{u} \in A, \ \forall \mathbf{s} \in B, \tag{4.29}$$

then the solution obtained from the problem (4.24) converges to the solution to the problem (4.20).

As the main goal to obtain convergence of the eigensolutions, assume that the uniform convergence of discrete operator $\mathcal{T}_h$ to the continuous operator is obtained, which can be stated as

$$||\mathcal{T} - \mathcal{T}_h||_B \to 0 \ \text{ for } \ h \to 0. \tag{4.30}$$

To be specific, consider the following setting about the spaces, and the bilinear forms as follows:

$$\begin{aligned} A &= H_0(\text{curl};\Omega), \\ B &= H_0(\text{div}^0;\Omega;\mu_r^{1/2}), \\ \mathfrak{a}(\mathbf{u},\mathbf{v}) &= (\epsilon_r\mathbf{u},\mathbf{v}), \\ \mathfrak{b}(\mathbf{u},\mathbf{s}) &= -(\mu_r^{-1/2}\nabla\times\mathbf{u},\mathbf{s}), \end{aligned} \tag{4.31}$$

and the assumptions needed for regularity on the domain and on the coefficients:

$$\begin{aligned} &\text{i) The domain } \Omega\subset\mathbb{R}^3 \text{ is a convex polyhedron,} \\ &\text{ii) } \mu_r \text{ and } \epsilon_r \text{ are scalar valued Lipschitz continuous functions.} \end{aligned} \tag{4.32}$$

Following the introduced settings (4.31) and (4.32), L^2-norm becomes the natural norm of B. Also, the seminorm related with $\mathfrak{a}(\cdot,\cdot)$ is identical to the L^2-norm since the assumption on the relative permittivity and the relative permeability is scalar-valued Lipschitz continuous functions. Moreover, Problem (4.20) is well-posed and the operator $\mathcal{T}$ associated with the problem (4.20) is continuous from B to $H_0(\text{div}^0;\Omega;\mu_r^{1/2})\cap H(\text{curl};\Omega;\mu_r^{-1/2})$.

The operator $\mathcal{T}$ is compact, since the space satisfies:

$$H_0(\text{div}^0;\Omega;\mu_r^{1/2})\cap H(\text{curl};\Omega;\mu_r^{-1/2})\subset H^1(\Omega),$$

where it follows from the assumption on Ω.

The discrete counterpart follows from the "edge" and "face" element spaces of order $k\geq 0$ that approximate $H_0(\text{curl};\Omega)$ and $H_0(\text{div};\Omega)$, respectively. These element spaces are defined in the following where $\mathfrak{T}_h$ is a given *regular* family of triangulations of Ω. Also, let K be a tetrahedron of $\mathfrak{T}_h$, and define:

$$\begin{aligned} \mathcal{E}^k &= \{\mathbf{u}\in H_0(\text{curl};\Omega)\ :\ \mathbf{u}|_K\ \in\ \mathcal{E}^k(K)\ \forall K \text{ in } \mathfrak{T}_h\}, \\ \mathcal{F}^k &= \{\mathbf{u}\in H_0(\text{div};\Omega)\ :\ \mathbf{u}|_K\ \in\ \mathcal{F}^k(K)\ \forall K \text{ in } \mathfrak{T}_h\}, \end{aligned} \tag{4.33}$$

where

$$\begin{aligned} \mathcal{E}^k(K) &= [\mathcal{P}_k(K)]^3\oplus\mathbf{x}\times\left[\tilde{\mathcal{P}}_k(K)\right]^3, \\ \mathcal{F}^k(K) &= [\mathcal{P}_k(K)]^3\oplus\tilde{\mathcal{P}}_k(K)\mathbf{x}. \end{aligned} \tag{4.34}$$

In equations (4.34), $\mathcal{P}_k(K)$ is the space of polynomials with degree $\leq k$ on K, $\tilde{\mathcal{P}}_k(K)$ is the polynomial space in $\mathcal{P}_k(K)$, which are homogeneous. Note that the elements

of $\mathcal{F}^k$ have a normal component, and the elements of $\mathcal{E}^k$ have a tangential component that are continuous across the interelement boundaries.

Considering the given settings associated with the case in this thesis, the following theorem is presented, whose proof can be found in [12].

Theorem 4.2.2 ((Theorem 4.3) [15]). *Let Ω be a convex polyhedron, and μ_r, ϵ_r be Lipschitz continuous scalar valued functions, for every $v \in H_0(curl;\Omega) \cap H(div^0;\Omega;\epsilon_r)$ there exists $I_h\mathbf{v} \in A_h$ such that*

$$\begin{aligned}(\mu_r^{-1/2}\nabla \times (\mathbf{v} - I_h\mathbf{v}), \mathbf{t}_h) = 0, \quad \forall \mathbf{t}_h \in B_h,\\ ||I_h\mathbf{v}||_A \leq C||\mathbf{v}||_{A_0}.\end{aligned} \tag{4.35}$$

Moreover, there exists $\varrho_2(h)$ tending to zero as h goes to zero such that

$$||v - I_h\mathbf{v}||_0 \leq \varrho_2(h)||\mathbf{v}||_{A_0}, \tag{4.36}$$

where $I_h : H_0(curl;\Omega) \cap H(div^0;\Omega;\epsilon_r) \to A_h$ is Fortin operator [47].

Now, consider the following theorem that combines the results obtained in [15] with those of [7].

Theorem 4.2.3 ((Theorem 4.4) [15]). *Let m_i be the multiplicity of λ_i, where λ_i is an eigenvalue of problem (4.19), and Θ_i be the associated eigenspace. Then exactly, m_i eigenvalues of problem (4.23) λ_{h,i_j} converge to λ_i. Denoting by $\Theta_{h,i}$ the direct sum of the eigenspaces corresponding to λ_{h,i_j}, it follows that there exists h_0 such that for $0 < h < h_0$ the following inequalities hold:*

$$\begin{aligned}|\lambda_i - \lambda_{h,i_j}| \leq C(\varrho_2(h) + h)^2, \quad \forall j = 1, \ldots, m_i,\\ \varpi(\Theta_i, \Theta_{h,i}) \leq C((\varrho_2(h) + h)),\end{aligned} \tag{4.37}$$

where C is a constant, which is not dependent of. Also, $\varpi(\Theta_i, \Theta_{h,i})$ is the gap between Θ_i and $\Theta_{h,i}$.
Lastly, consider the operator associated with the problem (4.19) and its real compact subset of the resolvent set denoted by $\mathfrak{R}$. Accordingly, all the nonzero eigenvalues of (4.23) remain outside of $\mathfrak{R}$, whenever $0 < h < h_0$.

Finally, it is important to consider also the two-dimensional case, where Theorem 4.2.3 is more precise. To be specific, the operator is a *Fortin operator*, where the assump-

tions are always satisfied since A_0 is compactly embedded in $[L^2(\Omega)^2]$. In addition, $\varrho_2(h)$ has an order of s if A_0 is a subset of $H^s(\Omega)$ [15].

4.2.3 Numerical Results of the Maxwell Eigenvalue Problem

This section presents the numerical results obtained by using standard FEM formulation given in (4.16) with the lowest-order first kind Nédélec basis functions. The Maxwell EVP is considered on the following domains with provided material properties that are presented as

- Square domain $\Omega_1 = [0, \pi]^2$ with $\mu_r = \epsilon_r = 1$.
- L-shape domain $\Omega_2 = [-1, 1]^2 \setminus ([0, 1] \times [0, -1])$ with $\mu_r = \epsilon_r = 1$.
- Cracked square domain $\Omega_3 = [-1, 1]^2$ with $\mu_r = \epsilon_r = 1$ and crack on a line between the points $(0, 0)$ and $(1, 0)$.
- Square domain with two different materials $\Omega_4 = [-1, 1]^2$ with $\mu_{r_1} = \mu_{r_2} = \epsilon_{r_2} = 1$ and $\epsilon_{r_1} = 0.5, 0.1$.
- Rectangular domain with two different materials $\Omega_5 = [0, 1] \times [0, 0.6]$ with $\mu_{r_1} = \mu_{r_2} = \epsilon_{r_1} = 1$ and $\epsilon_{r_2} = 6$.
- Cube domain $\Omega_6 = [0, \pi]^3$ with $\mu_r = \epsilon_r = 1$.
- Thick L-shape domain $\Omega_7 = \Omega_2 \times [0, 1]$ with $\mu_r = \epsilon_r = 1$.
- Fichera corner domain $\Omega_8 = [-1, 1]^3 \setminus [-1, 0]^3$ with $\mu_r = \epsilon_r = 1$.

The square domain Ω_1 and the cube domain Ω_5 are considered for validation since the exact solutions are known. The L-shape and cracked square domains are considered for testing the numerical method on singular solutions. The square domain with two different materials Ω_4 is chosen to validate that the method well approximates the singularity coming from material properties. The numerical results are obtained for Ω_4 using artificial relative permittivity values so that the validation can be presented by comparing the results with the ones presented in benchmarks [34, 40]. Next, the rectangular domain with two different materials Ω_5 is considered for the problem

of finding cutoff wavenumbers and TE modes for the dielectric-loaded waveguide, which involves solving the Maxwell EVP. This case is also considered to validate the same situation encountered in the previous domain with physically possible parameter values. Finally, tests on 3D domains are included to verify that the constructed frame can handle extension to the third dimension.

The numerical tests are performed on several meshes for the presented domains. Uniform, criss-cross, and unstructured meshes are used for the numerical tests on Ω_1, Ω_2, Ω_4, and Ω_5. Uniform and criss-cross meshes are used for Ω_3. Lastly, uniform and unstructured meshes are tested for all three-dimensional domains $\Omega_6, \Omega_7, \Omega_8$.

Moreover, based on the results in [19] that present the convergence of first-order Lagrange basis functions satisfying certain attributes on Powell-Sabin triangulations, a comparison is performed on Ω_3. The FEM approximations using the edge elements and a sort of nodal elements introduced in [19] for the cracked square domain.

The convergence behavior of the FEM approximation of eigenvalues to the exact eigenvalues is investigated in the square and cube domains. The reference eigenvalues from the benchmark presented in [40] are followed for other cases, and the convergence rates of the approximations to these reference eigenvalues are examined. Furthermore, the plots of approximate eigenfunctions are compared with the benchmark presented in [34].

4.2.3.1 Numerical Results of 2D Domains

The numerical results of finite element approximation of Maxwell EVP using Nédélec basis functions in two-dimensional domains are presented. The standard finite element formulation is used since Nédélec basis functions are discretely divergence-free. The approximated eigenvalues are compared with the exact and reference ones, and the convergence rate of the approximation is discussed in consideration of the theoretical results presented previously. Also, as expected, the number of zero eigenvalues equals the number of internal nodes. The standard finite element formulation introduced in (4.16) is used for the following numerical experiments and again given in the following.

Find $\lambda_h \in \mathbb{R},\ \lambda_h \neq 0$ and $\mathbf{u}_h \in \mathfrak{U}_h$ with $\mathbf{u}_h \neq 0$ such that

$$(\mu_r^{-1}\nabla \times \mathbf{u}_h, \nabla \times \mathbf{v}_h) = \lambda_h(\mathbf{u}_h, \mathbf{v}_h)\ \ \forall \mathbf{v}_h \in \mathfrak{U}_h,$$

where $\mathfrak{U}_h$ is the finite-dimensional subspace of $H_0(\text{curl}; \Omega)$ constructed using Nédélec edge elements. It is known that $\mathbf{u}_h \in \mathfrak{U}_h$ is expressed as $\mathbf{u}_h = \sum_{m=1}^{n_e} u_m \Upsilon_m$, where Υ_m are the global Nédélec basis functions that are related to the edge m with the degrees of freedom n_e after imposing Dirichlet boundary condition, and u_m are the coefficients to be found that control the tangential field over the edge m. This leads to the following generalized eigenvalue problem of finding $\lambda \in \mathbb{R}$, and corresponding eigenvector u that is stated as

$$\mathbf{K}u = \lambda \mathbf{M}u, \tag{4.38}$$

where $\mathbf{K}$ is the stiffness matrix, $\mathbf{M}$ is the mass matrix.

After obtaining the approximate nonzero eigenvalues λ_h and corresponding eigenvectors u_h of Problem (4.38), the visualization of eigenfunctions is performed as

$$\mathbf{u}_h^n = \sum_{m=1}^{n_e} \frac{u_{h,m}^n}{||u_{h,m}^n||} \Upsilon_m, \tag{4.39}$$

where $u_{h,m}^n$ is the n-th eigenvector obtained from the approximation of the EVP where each element of the n-th eigenvector corresponds to the m-th edge. Additionally, Υ_m is the global Nédélec basis function related to the edge m; each is computed at the centroid of the triangles (elements) in the mesh.

Also, the convergence rates CR_i of approximate eigenvalues are calculated as

$$CR_i = \frac{\ln \mathrm{e}_{i-1} - \ln \mathrm{e}_i}{\ln \mathrm{h}_{i-1} - \ln \mathrm{h}_i},\ i = 2, 3, 4, 5, \tag{4.40}$$

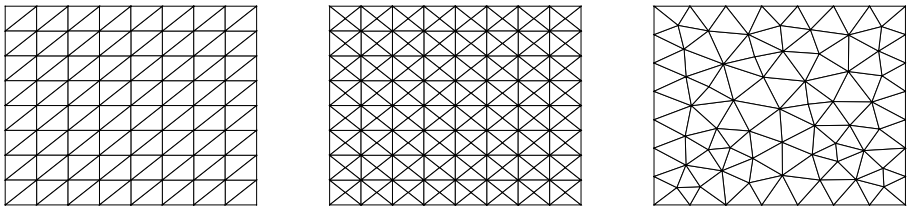
where e_i is the error between the approximate and exact (or reference) eigenvalue at i-th FEM approximation with the maximum edge length h_i in the mesh.

4.2.3.1.1 Square Domain Maxwell's EVP on $\Omega_1 = [0, \pi]^2$ with $\epsilon_r = \mu_r = 1$ is approximated with the lowest-order first kind Nédélec elements on the uniform, criss-cross and unstructured meshes.

The exact eigenvalues with the corresponding eigenvectors are given as [19]

$$\begin{aligned} \lambda^{m,n} &= m^2 + n^2, \\ \mathbf{u}^{m,n} &= (-m\sin(my)\cos(nx), n\sin(nx)\cos(my))^T, \end{aligned} \tag{4.41}$$

where $m, n = 0, 1, 2, \ldots,\ m + n \neq 0$.



(a) $N = 8$ (b) $N = 8$ (c) $h_{max} = 0.331$

Figure 4.4: Uniform, criss-cross, and unstructured meshes of the square domain.

The results of first ten approximate eigenvalues on uniform and criss-cross meshes are given in Table 4.2 and Table 4.3 after eliminating the zero eigenvalues. It is important to note that the results provided in Table 4.2 obtained by the present scheme agree very well with those reported in [13].

Table 4.2: The first ten exact and approximated eigenvalues on a sequence of uniform meshes with the convergence rates.

Exact	N = 4	N = 8	N = 16	N = 32	N = 64
1	0.9702	0.9923(2.0)	0.9981(2.0)	0.9995(2.0)	0.9999(2.0)
1	0.9960	0.9991(2.2)	0.9998(2.1)	0.9999(2.0)	1.0000(2.0)
2	2.0288	2.0082(1.8)	2.0021(2.0)	2.0005(2.0)	2.0001(2.0)
4	3.7227	3.9316(2.0)	3.9829(2.0)	3.9957(2.0)	3.9989(2.0)
4	3.7339	3.9325(2.0)	3.9829(2.0)	3.9957(2.0)	3.9989(2.0)
5	4.7339	4.9312(2.0)	4.9826(2.0)	4.9956(2.0)	4.9989(2.0)
5	5.1702	5.0576(1.6)	5.0151(1.9)	5.0038(2.0)	5.0010(2.0)
8	7.4306	8.1016(2.5)	8.0322(1.7)	8.0084(1.9)	8.0021(2.0)
9	7.5231	8.6292(2.0)	8.9061(2.0)	8.9764(2.0)	8.9941(2.0)
9	7.9586	8.6824(1.7)	8.9211(2.0)	8.9803(2.0)	8.9951(2.0)
zeros	9	49	225	961	3969
DOF	40	176	736	3008	12160

Table 4.3: The first ten exact and approximated eigenvalues on a sequence of criss-cross meshes with the convergence rates.

Exact	N = 4	N = 8	N = 16	N = 32	N = 64
1	1.0042	1.0011(2.0)	1.0003(2.0)	1.0001(2.0)	1.0000(2.0)
1	1.0042	1.0011(2.0)	1.0003(2.0)	1.0001(2.0)	1.0000(2.0)
2	1.9655	1.9914(2.0)	1.9979(2.0)	1.9995(2.0)	1.9999(2.0)
4	4.0602	4.0167(1.9)	4.0043(2.0)	4.0011(2.0)	4.0003(2.0)
4	4.0602	4.0167(1.9)	4.0043(2.0)	4.0011(2.0)	4.0003(2.0)
5	4.8929	4.9749(2.1)	4.9938(2.0)	4.9985(2.0)	4.9996(2.0)
5	4.8929	4.9749(2.1)	4.9938(2.0)	4.9985(2.0)	4.9996(2.0)
8	7.4306	7.8619(2.0)	7.9657(2.0)	7.9914(2.0)	7.9979(2.0)
9	9.2283	9.0811(1.5)	9.0213(1.9)	9.0054(2.0)	9.0014(2.0)
9	9.2283	9.0811(1.5)	9.0213(1.9)	9.0054(2.0)	9.0014(2.0)
zeros	25	113	481	1985	8065
DOF	88	368	1504	6080	24448

It is seen from Table 4.2 and Table 4.3 that the convergence rates of the FEM approximation in uniform and criss-cross meshes are quadratic, as demonstrated in the theoretical results. Moreover, the results of approximations in unstructured meshes are presented in Table 4.4 from which it is observed that the convergence rates vary and are mostly higher than degree 2 for the unstructured mesh.

Table 4.4: The first ten exact and approximated eigenvalues on a sequence of unstructured meshes with the convergence rates.

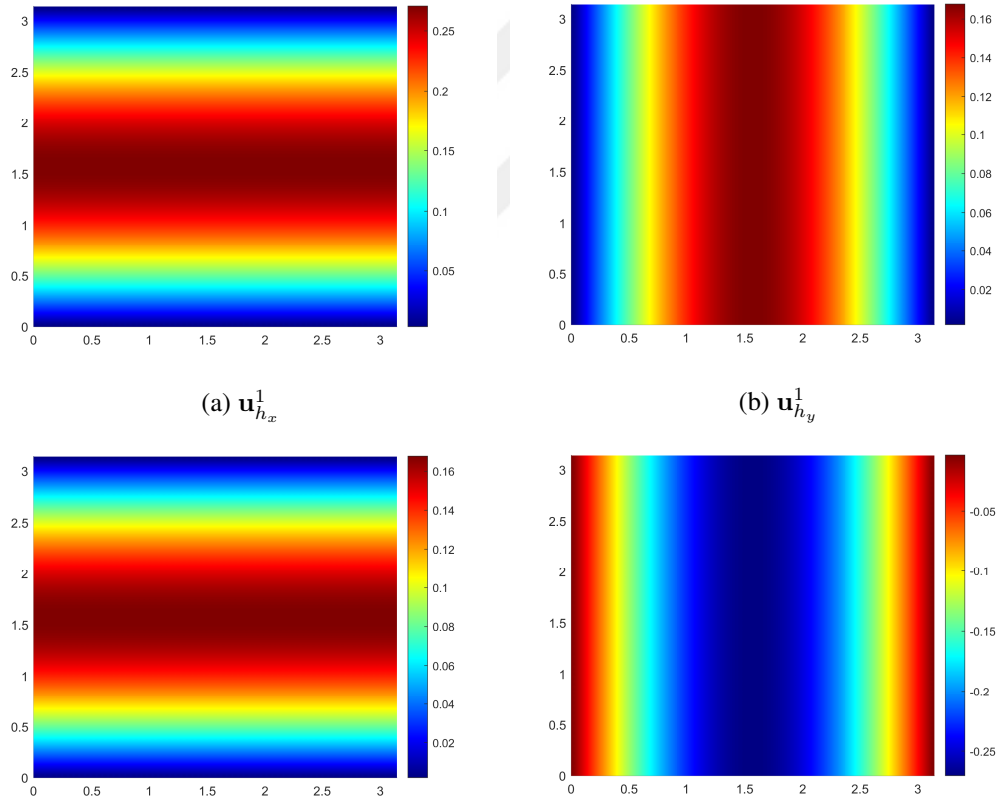
Exact	h_{max} = 0.7	h_{max} = 0.331	h_{max} = 0.1628	h_{max} = 0.0814	h_{max} = 0.0407
1	0.9961	1.0007(2.4)	0.9999(3.2)	1.0000(1.0)	1.0000(3.6)
1	0.9961	1.0009(2.0)	1.0001(2.6)	1.0000(2.7)	1.0000(3.9)
2	2.0320	1.9957(2.7)	1.9998(4.2)	2.0001(0.6)	2.0000(3.9)
4	3.7601	3.9926(4.6)	3.9982(2.0)	3.9993(1.4)	3.9999(3.4)
4	4.1918	3.9938(4.6)	4.0007(3.1)	3.9999(3.6)	4.0000(0.3)
5	5.0896	4.9871(2.6)	4.9995(4.5)	5.0002(1.4)	5.0000(2.1)
5	5.0896	4.9927(3.3)	5.0044(0.7)	5.0005(3.1)	5.0001(3.2)
8	8.6577	7.9793(4.6)	7.9995(5.3)	8.0021(2.1)	8.0002(3.2)
9	8.6577	8.9611(2.9)	8.9935(2.5)	8.9961(0.8)	8.9996(3.3)
9	8.7057	9.0020(6.6)	8.9958(1.0)	8.9973(0.6)	8.9998(3.9)
zeros	9	49	226	988	4006
DOF	36	172	727	3061	12215

Considering the theoretical convergence properties of approximate eigenvalues, quadratic convergence rates are expected if the triangulation of the convex domain is regular. Therefore, varying convergence rates are also expected in the case of an unstruc-

tured mesh.

As seen from the numerical results, the approximate eigenvalues converge to the exact ones in uniform, criss-cross, and unstructured meshes. Also, as expected, the number of zero eigenvalues equals the number of internal vertices.

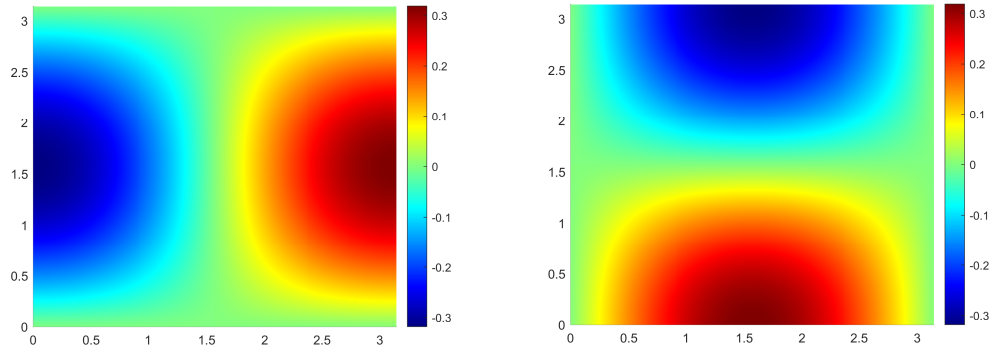
Furthermore, the plots of the approximated first five eigenfunctions are presented as contours of each component in Figure 4.5. In these figures, the behaviors of eigenfunctions associated with the same eigenvalues with multiplicity 2 are similar. Also, the approximate eigenfunctions agree well with the exact ones given in (4.41). Additionally, the quiver plots of divergence-free eigenfunctions with zero tangential components on the boundary are presented in Figure 4.6.



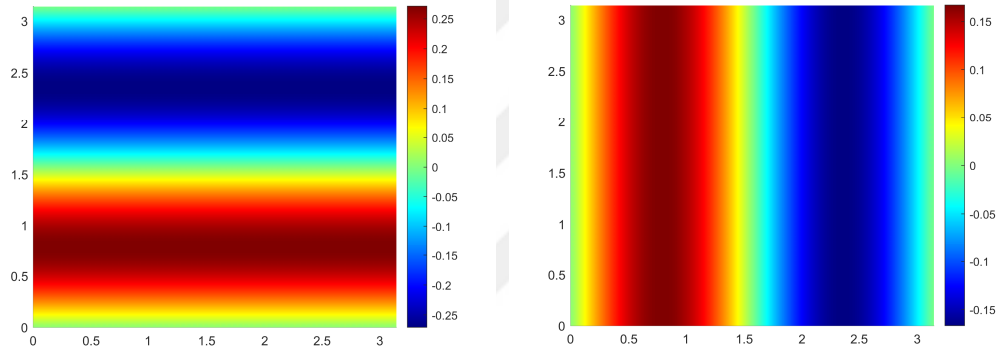
(a) $\mathbf{u}_{h_x}^1$ (b) $\mathbf{u}_{h_y}^1$

(c) $\mathbf{u}_{h_x}^2$ (d) $\mathbf{u}_{h_y}^2$

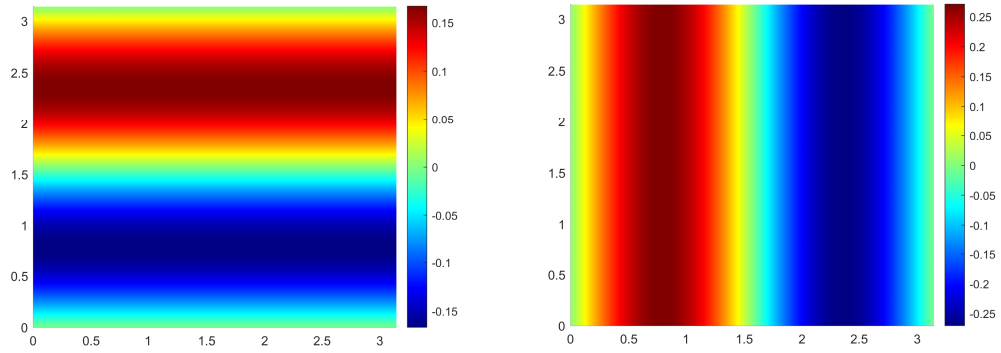
Figure 4.5: Contours of the first five approximated eigenfunctions using criss-cross mesh with 24448 DOF on Ω_1.



(e) $\mathbf{u}^3_{h_x}$ (f) $\mathbf{u}^3_{h_y}$

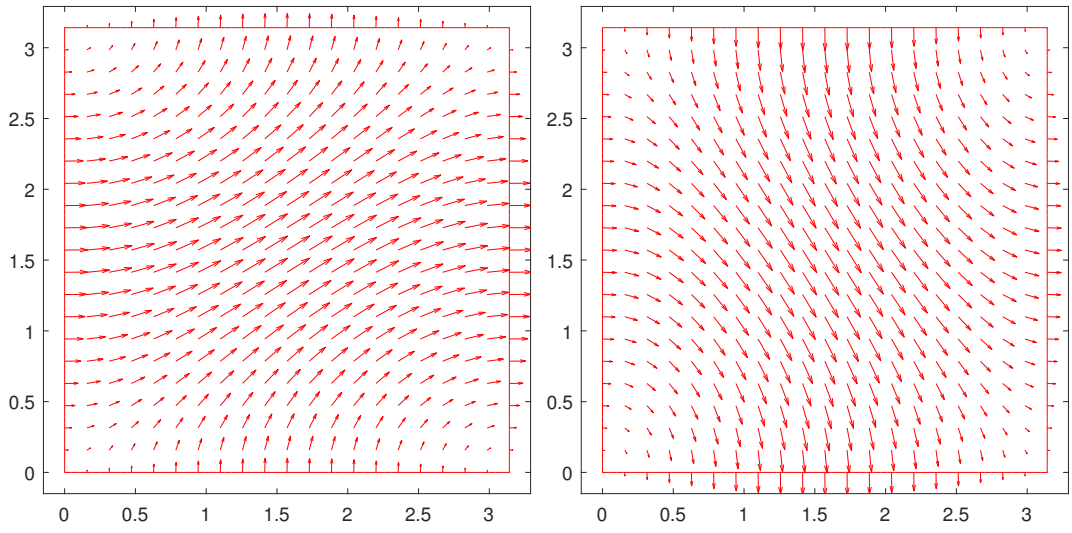


(g) $\mathbf{u}^4_{h_x}$ (h) $\mathbf{u}^4_{h_y}$



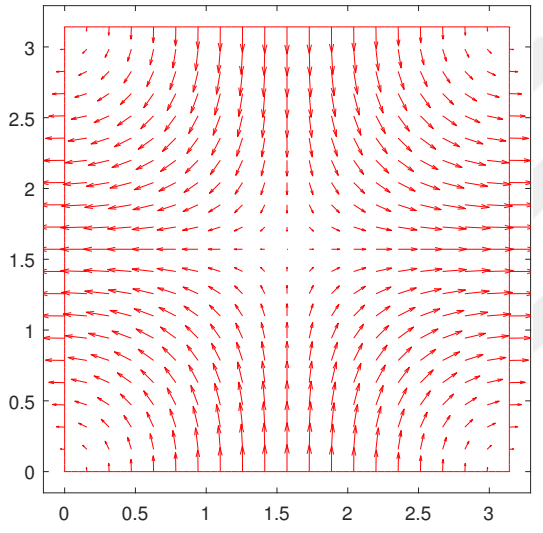
(i) $\mathbf{u}^5_{h_x}$ (j) $\mathbf{u}^5_{h_y}$

Figure 4.5: Contours of the first five approximated eigenfunctions using criss-cross mesh with 24448 DOF on Ω_1. (cont.)

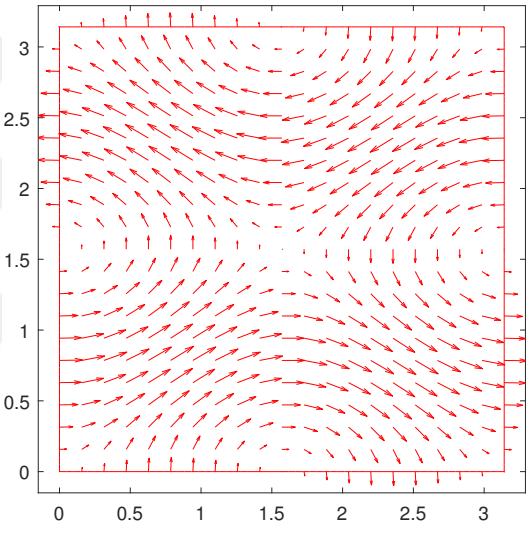


(a) $\mathbf{u}_h^1$

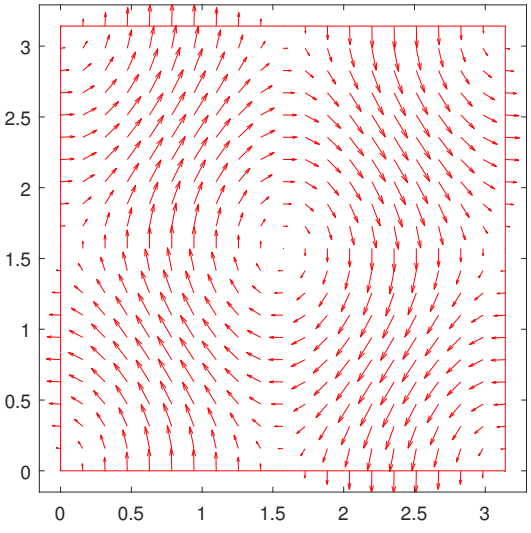
(b) $\mathbf{u}_h^2$



(c) $\mathbf{u}_h^3$



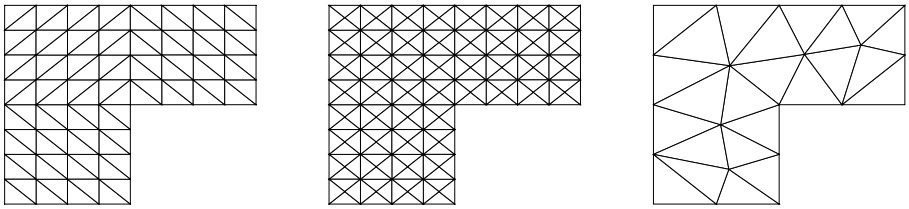
(d) $\mathbf{u}_h^4$



(e) $\mathbf{u}_h^5$

Figure 4.6: Quivers of the first five approximated eigenfunctions using criss-cross mesh with 24448 DOF on Ω_1.

4.2.3.1.2 L-Shape Domain Maxwell's EVP on $\Omega_2 = [-1,1]^2 \setminus ([0,1] \times [0,-1])$ with $\epsilon_r = \mu_r = 1$ is approximated on the uniform, criss-cross, and unstructured meshes given in Figure 4.7.



(a) $N = 8$ (b) $N = 8$ (c) $h_{max} = 0.062$

Figure 4.7: Uniform, criss-cross, and unstructured meshes of the L-shape domain.

The results of the first five approximate eigenvalues after eliminating the zero eigenvalues on a sequence of three different meshes are presented in Table 4.5, Table 4.6, and Table 4.7. The reference eigenvalues are followed from the benchmark presented in [40].

Table 4.5: The first five reference and approximated eigenvalues on a sequence of uniform meshes with the convergence rates.

Reference Eigenvalues	N =4	N = 8	N = 16	N = 32	N = 64
1.4756	1.3227	1.4165(1.4)	1.4527(1.4)	1.4667(1.4)	1.4721(1.4)
3.5340	3.5181	3.5281(1.4)	3.5322(1.6)	3.5335(1.8)	3.5339(1.9)
9.8696	8.8082	9.5751(1.8)	9.7938(2.0)	9.8505(2.0)	9.8648(2.0)
9.8696	9.5999	9.8306(2.8)	9.8612(2.2)	9.8676(2.1)	9.8691(2.0)
11.3894	11.3299	11.4011(2.4)	11.3932(1.7)	11.3904(2.0)	11.3897(2.1)
zeros	5	33	161	705	2945
DOF	28	128	544	2240	9088

The numerical results in uniform and criss-cross meshes show that the rates of convergence are quadratic except for the first and second approximate eigenvalues since the L-shape domain contains a singularity at the point $(0,0)$.

Table 4.6: The first five reference and approximated eigenvalues on a sequence of criss-cross meshes with the convergence rates.

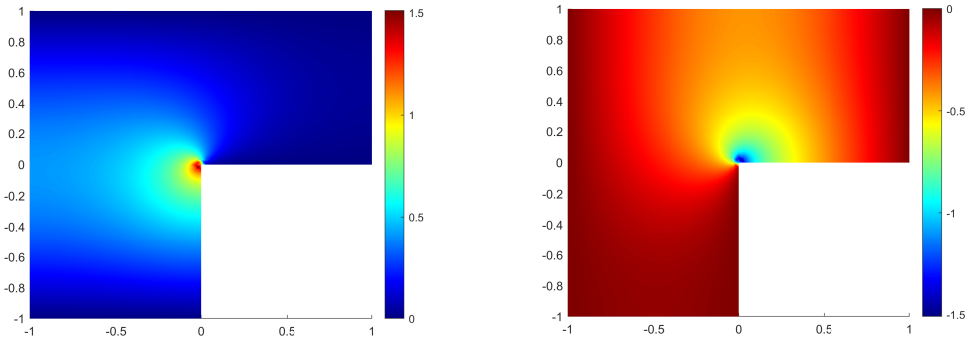
Reference Eigenvalues	N = 4	N = 8	N = 16	N = 32	N = 64
1.4756	1.3992	1.4439(1.3)	1.4626(1.3)	1.4704(1.3)	1.4735(1.3)
3.5340	3.5423	3.5349(3.2)	3.5341(4.7)	3.5340(0.7)	3.5340(1.1)
9.8696	10.0182	9.9107(1.9)	9.8801(2.0)	9.8722(2.0)	9.8703(2.0)
9.8696	10.0182	9.9107(1.9)	9.8801(2.0)	9.8722(2.0)	9.8703(2.0)
11.3894	11.2985	11.3687(2.1)	11.3842(2.0)	11.3881(2.0)	11.3891(2.0)
zeros	17	81	353	1473	6017
DOF	64	272	1120	4544	18304

Table 4.7: The first five reference and approximated eigenvalues on a sequence of unstructured meshes with the convergence rates.

Reference Eigenvalues	Hmax=0.62	Hmax=0.32	Hmax=0.1614	Hmax = 0.0811	Hmax = 0.0412
1.4756	1.3427	1.4227(1.4)	1.4567(1.5)	1.4679(1.3)	1.4727(1.4)
3.5340	3.5247	3.5312(1.8)	3.5351(1.4)	3.5341(5.6)	3.5340(0.5)
9.8696	9.4193	9.8186(3.3)	9.8680(5.1)	9.8682(0.1)	9.8694(3.0)
9.8696	9.7364	9.8341(2.0)	9.8737(3.2)	9.8689(2.5)	9.8695(3.6)
11.3894	11.2400	11.3698(3.1)	11.3952(1.8)	11.3892(4.4)	11.3894(2.8)
zeros	5	33	164	713	2963
DOF	28	128	545	2240	9086

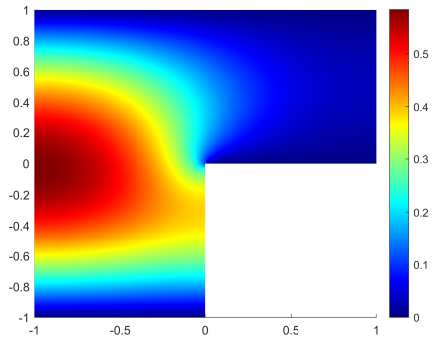
Moreover, it is seen that the convergence rates vary in the unstructured meshes even for the approximate eigenvalues with quadratic convergence rates in uniform and criss-cross meshes, as in the case of Ω_1.

Considering the numerical results in three different meshes, it is confirmed that the approximate eigenvalues converge to the reference eigenvalues for this domain with a singular point. Furthermore, the contours of the first five approximated eigenfunctions' components are presented in Figure 4.8, where these figures agree well with the benchmark contours of eigenfunctions presented in [34]. The presence of singularity in the first eigenfunction can be seen from these figures. Also, the third and the fourth eigenfunctions' behaviors are similar since they correspond to the same eigenvalue with multiplicity 2. Lastly, the quiver plots that present the divergence-free vector fields of eigenfunctions with zero tangential components on the boundary are given in Figure 4.9.

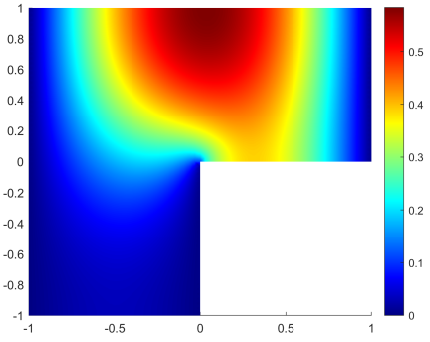


(a) $\mathbf{u}^1_{h_x}$ (b) $\mathbf{u}^1_{h_y}$

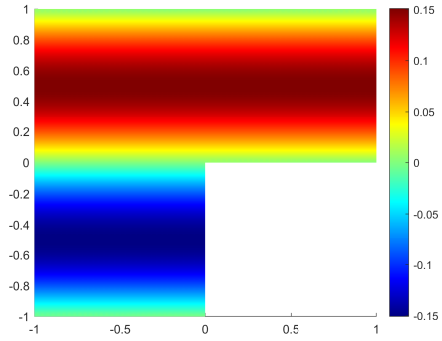
Figure 4.8: Contours of the first five approximated eigenfunctions using criss-cross mesh with 18304 DOF on Ω_2.



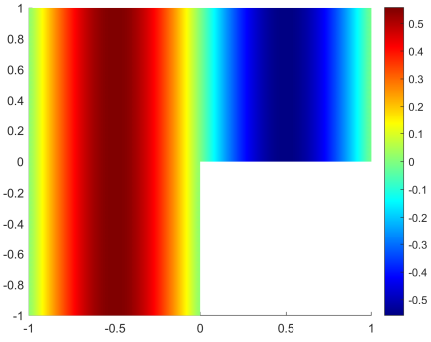
(c) $\mathbf{u}_{h_x}^2$



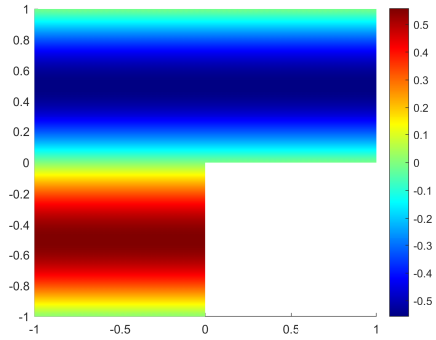
(d) $\mathbf{u}_{h_y}^2$



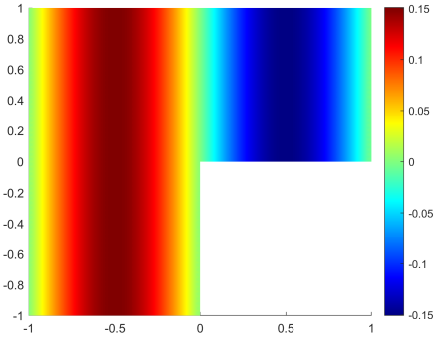
(e) $\mathbf{u}_{h_x}^3$



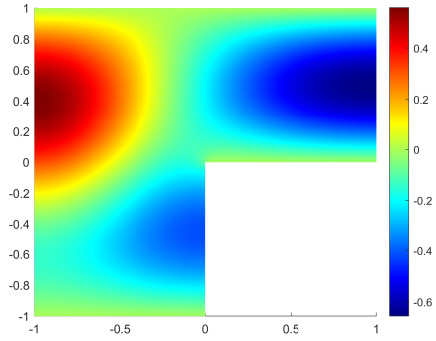
(f) $\mathbf{u}_{h_y}^3$



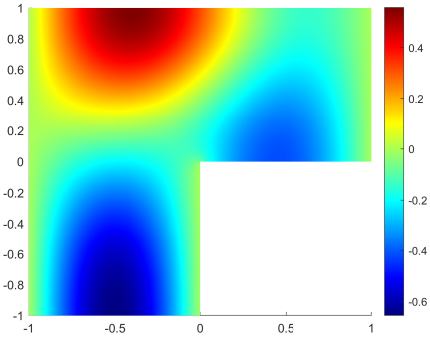
(g) $\mathbf{u}_{h_x}^4$



(h) $\mathbf{u}_{h_y}^4$

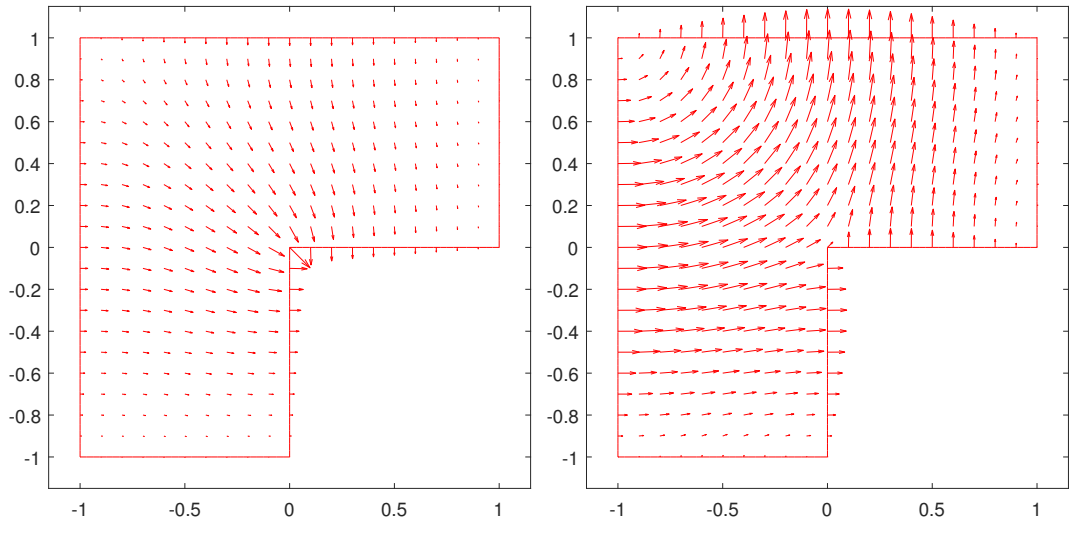


(i) $\mathbf{u}_{h_x}^5$



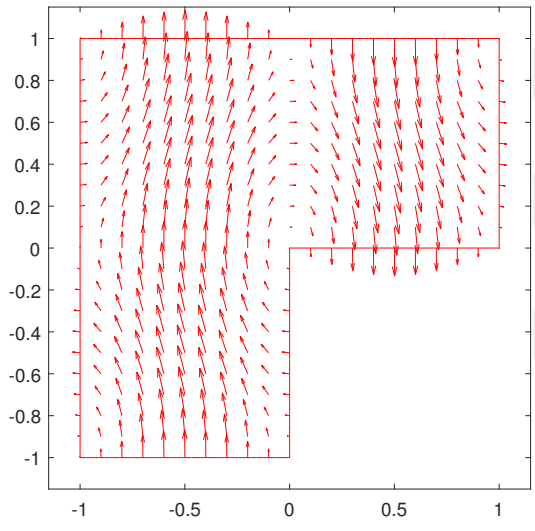
(j) $\mathbf{u}_{h_y}^5$

Figure 4.8: Contours of the first five approximated eigenfunctions using criss-cross mesh with 18304 DOF on Ω_2. (cont.)

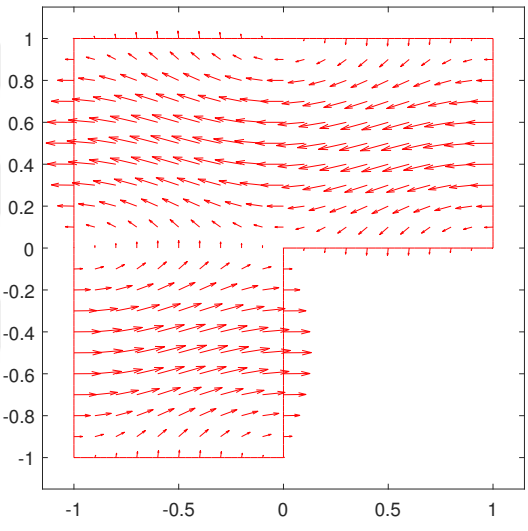


(a) $\mathbf{u}_h^1$

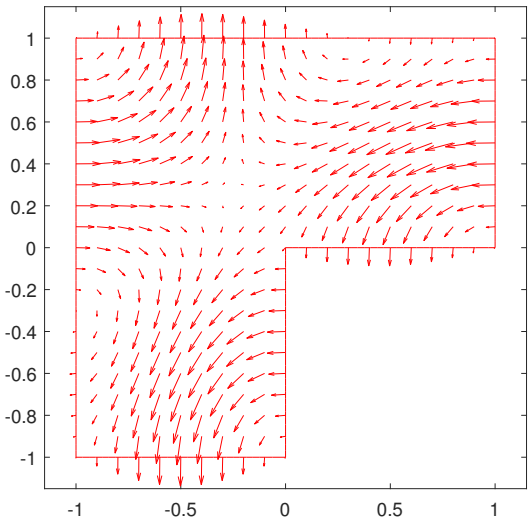
(b) $\mathbf{u}_h^2$



(c) $\mathbf{u}_h^3$



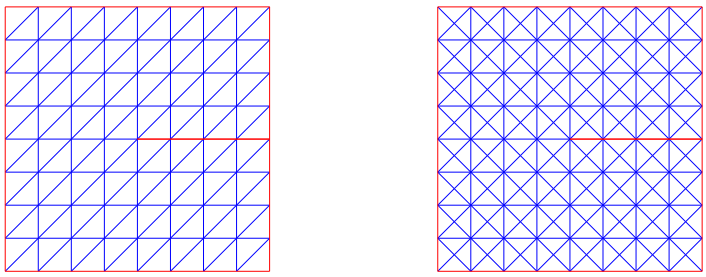
(d) $\mathbf{u}_h^4$



(e) $\mathbf{u}_h^5$

Figure 4.9: Quivers of the first five approximated eigenfunctions using criss-cross mesh with 18304 DOF on Ω_2.

4.2.3.1.3 Cracked Square Domain The Maxwell EVP on the cracked square domain $\Omega_3 = [-1, 1]^2$ that contains a crack on a line between the points $(0, 0)$ and $(1, 0)$ with $\mu_r = \epsilon_r = 1$ is approximated on the uniform, and criss-cross meshes given in Figure 4.10.



(a) $N = 8$ (b) $N = 8$

Figure 4.10: Uniform and criss-cross meshes of the cracked square domain where the red part indicates the boundary.

Table 4.8 and Table 4.9 present the first ten approximate eigenvalues on uniform and criss-cross meshes, respectively. Note that the zero eigenvalues are eliminated where their number equals the number of internal vertices. Also, in the followed benchmark presented in [40], the reference values are obtained using locally refined mesh around the points $(0, 0)$ and polynomials of degree 10.

This domain contains a strong singularity. Therefore, it is expected to observe that some approximate eigenvalues will not converge with order 2.

Table 4.8: The first ten reference and approximated eigenvalues on a sequence of uniform meshes with the convergence rates.

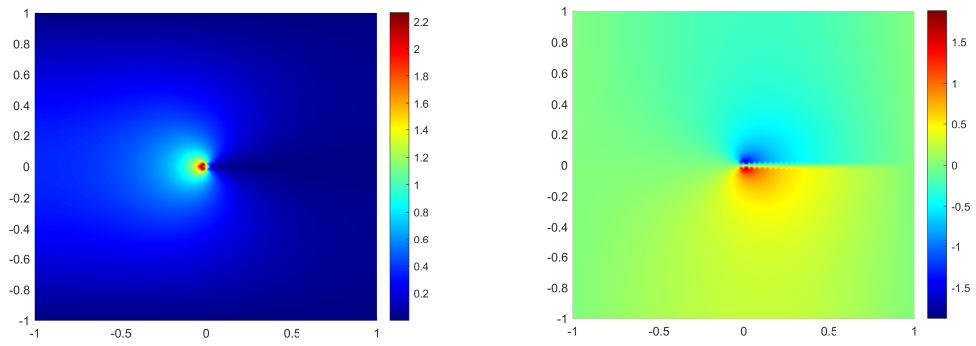
Reference Eigenvalues	N = 4	N = 8	N = 16	N = 32	N = 64
1.0341	0.8116	0.9198(1.0)	0.9761(1.0)	1.0049(1.0)	1.0194(1.0)
2.4674	2.4248	2.4568(2.0)	2.4648(2.0)	2.4667(2.0)	2.4672(2.0)
4.0469	4.0601	4.0474(4.9)	4.0467(0.8)	4.0468(1.2)	4.0469(1.7)
9.8696	9.1384	9.6956(2.1)	9.8270(2.0)	9.8590(2.0)	9.8670(2.0)
9.8696	9.1960	9.7018(2.0)	9.8274(2.0)	9.8590(2.0)	9.8670(2.0)
10.8448	10.3745	10.7444(2.2)	10.8197(2.0)	10.8385(2.0)	10.8433(2.0)
12.2648	10.7093	11.6717(1.4)	12.0087(1.2)	12.1451(1.1)	12.2068(1.0)
12.3370	12.3677	12.3514(1.1)	12.3377(4.4)	12.3367(1.1)	12.3369(1.2)
19.7392	17.8267	19.9690(3.1)	19.8185(1.5)	19.7600(1.9)	19.7445(2.0)
21.2441	18.7588	20.1235(1.1)	20.7501(1.2)	21.0172(1.1)	21.1363(1.1)
zeros	7	45	217	945	3937
DOF	38	172	728	2992	12128

Table 4.9: The first ten reference and approximated eigenvalues on a sequence of criss-cross meshes with the convergence rates.

Reference Eigenvalues	N = 4	N = 8	N = 16	N = 32	N = 64
1.0341	0.8860	0.9557(0.9)	0.9937(1.0)	1.0136(1.0)	1.0238(1.0)
2.4674	2.4777	2.4700(2.0)	2.4681(2.0)	2.4676(2.0)	2.4674(2.0)
4.0469	4.0326	4.0423(1.6)	4.0456(1.8)	4.0466(1.9)	4.0468(2.0)
9.8696	10.0182	9.9107(1.9)	9.8801(2.0)	9.8722(2.0)	9.8703(2.0)
9.8696	10.0182	9.9107(1.9)	9.8801(2.0)	9.8722(2.0)	9.8703(2.0)
10.8448	10.8387	10.8456(3.1)	10.8451(1.9)	10.8449(2.5)	10.8449(2.5)
12.2648	11.5398	11.9253(1.1)	12.0997(1.0)	12.1835(1.0)	12.2245(1.0)
12.3370	12.0727	12.2750(2.1)	12.3217(2.0)	12.3332(2.0)	12.3361(2.0)
19.7392	18.3344	19.3985(2.0)	19.6545(2.0)	19.7181(2.0)	19.7339(2.0)
21.2441	19.4186	20.6098(1.5)	20.9520(1.1)	21.1003(1.0)	21.1724(1.0)
zeros	23	109	473	1969	8033
DOF	86	364	1496	6064	24416

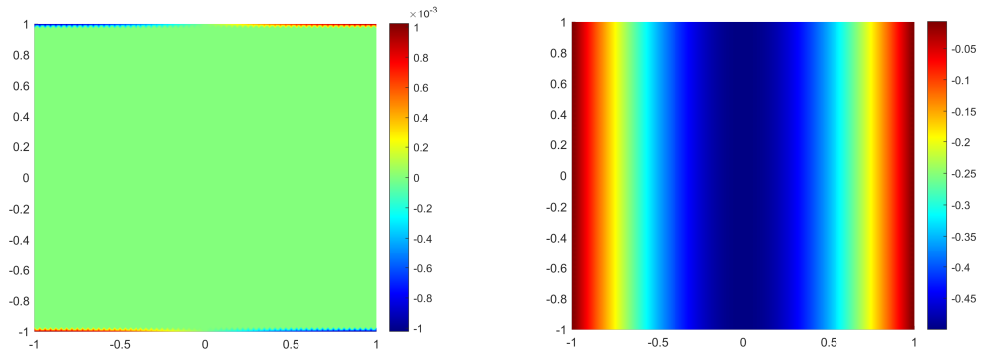
As expected, the approximation converges with the quadratic rate of convergence except for some eigenvalues. For example, the first eigenvalue is approximated with order 1 because this eigenvalue corresponds to an eigenvector with low regularity. The others that approximate with quadratic convergence rates correspond to eigenvectors in H^1 [19].

The plots of the first five eigenfunctions are presented as contours of each component in Figure 4.11, and as vector fields in Figure 4.12. The contours are in good agreement with the benchmark [34]. Figure 4.11 shows the singularity of the first eigenfunction. Also, $\mathbf{u}^2_{h_x}$ can be neglected since it is approximately zero. Lastly, the fourth and fifth eigenfunctions that correspond to the same eigenvalue value with multiplicity 2 show the same behavior, as observed in the previous cases.

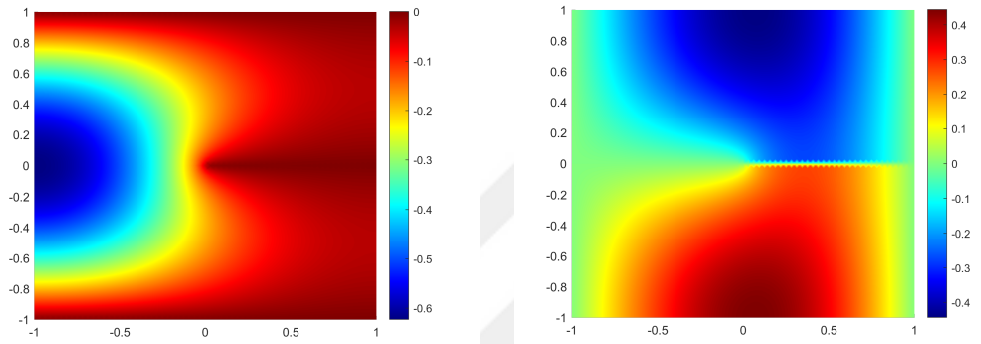


(a) $\mathbf{u}^1_{h_x}$ (b) $\mathbf{u}^1_{h_y}$

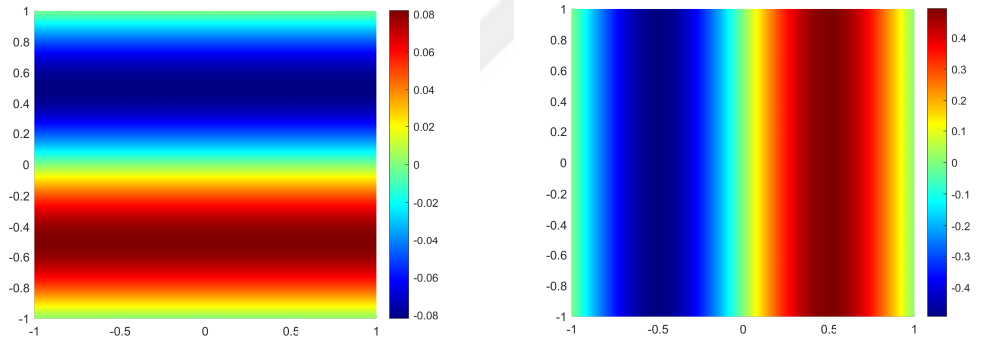
Figure 4.11: Contours of the first five approximated eigenfunctions using criss-cross mesh with 24416 DOF on Ω_3.



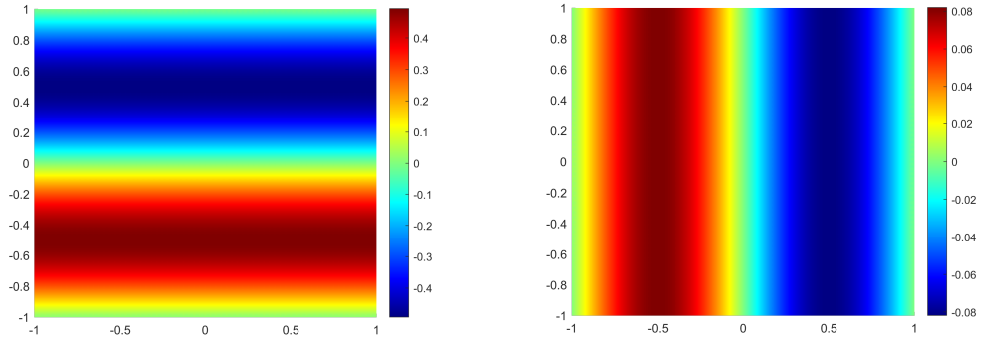
(c) $\mathbf{u}_{h_x}^2$ (d) $\mathbf{u}_{h_y}^2$



(e) $\mathbf{u}_{h_x}^3$ (f) $\mathbf{u}_{h_y}^3$

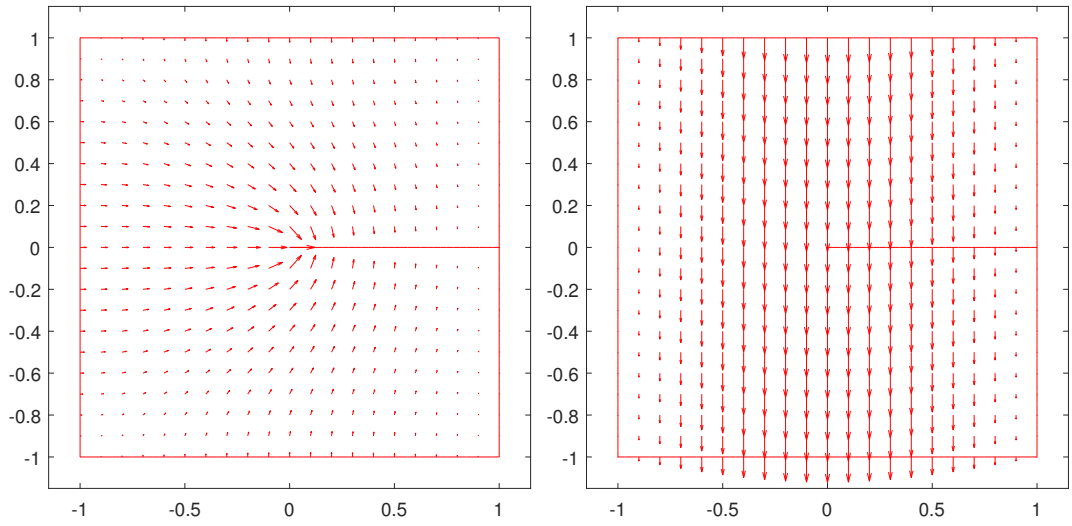


(g) $\mathbf{u}_{h_x}^4$ (h) $\mathbf{u}_{h_y}^4$



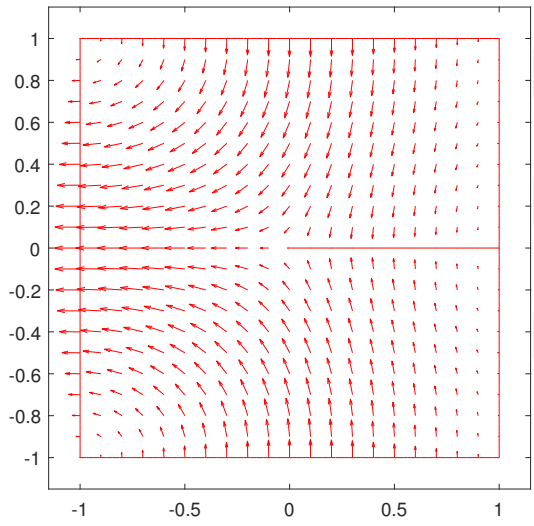
(i) $\mathbf{u}_{h_x}^5$ (j) $\mathbf{u}_{h_y}^5$

Figure 4.11: Contours of the first five approximated eigenfunctions using criss-cross mesh with 24416 DOF on Ω_3. (cont.)

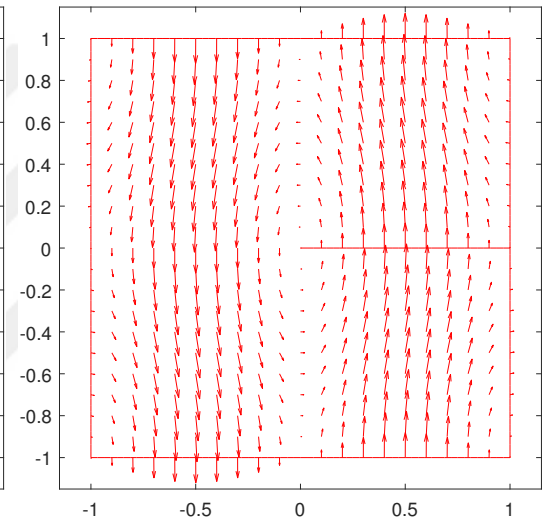


(a) $\mathbf{u}_h^1$

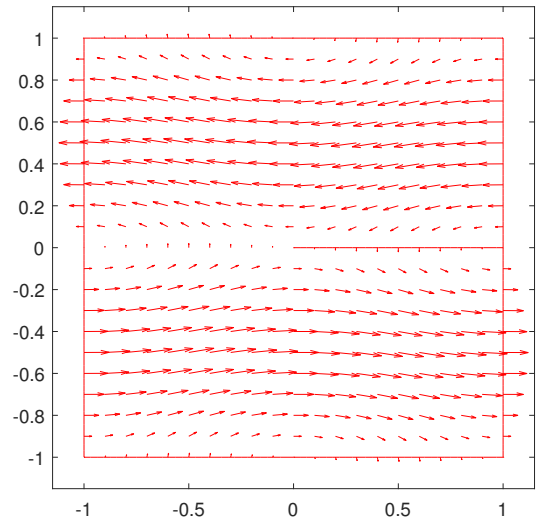
(b) $\mathbf{u}_h^2$



(c) $\mathbf{u}_h^3$



(d) $\mathbf{u}_h^4$

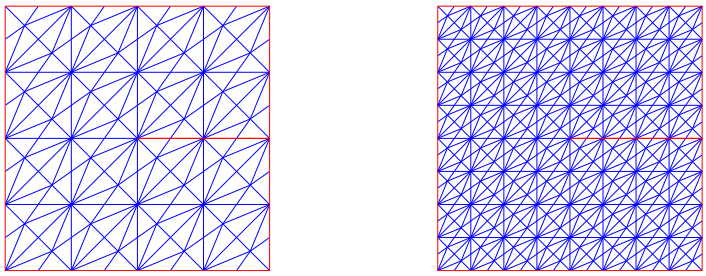


(e) $\mathbf{u}_h^5$

Figure 4.12: Quivers of the first five approximated eigenfunctions using criss-cross mesh with 24416 DOF on Ω_3.

4.2.3.1.4 Cracked Domain with Powell-Sabin Triangulation

The Maxwell EVP on the cracked square domain $\Omega_3 = [-1,1]^2$ that contains a crack on a line between the points $(0,0)$ and $(1,0)$ with $\mu_r = \epsilon_r = 1$ is approximated using Nédélec edge elements and linear Lagrange basis functions satisfying specific properties on Powell-Sabin triangulations, which are shown in Figure 4.13.



(a) $N = 4$ (b) $N = 8$

Figure 4.13: Powell-Sabin triangulation of the cracked square domain where the boundary is indicated in red.

Powell-Sabin triangulations are obtained by employing a refinement procedure on the uniform triangulations. Firstly, consider an element K in uniform triangulation $\mathfrak{T}_h$ (see, Figure 4.10a), where the incenter and midpoints of each edge of $K \in \mathfrak{T}_h$ are determined. It follows that the incenter is connected to each vertex of K. Lastly, the midpoints of edges are connected to the incenter. This way, Powell-Sabin triangulation $\mathfrak{T}_h^{\text{ps}}$ is obtained (see, Figure 4.13b), where each element $K \in \mathfrak{T}_h$ is split into six triangles.

The convergence of FEM using linear Lagrange basis functions satisfying special properties on Powell-Sabin triangulations is presented in [19] by using the same equivalent mixed formulations (3.46) and (4.17) of the Maxwell EVP. In the analyses, the similar structure studied in [15] is used, which is also presented in Section 4.2.2. In order to prove the convergence of discrete eigenvalues to the correct ones, the uniform convergence of the associated discrete source problem is shown with the help of the modified Scott-Zhang interpolant at the corners of Ω. The modified Scott-Zhang interpolant can be found in [22].

The two convergent FEM approximations of the Maxwell EVP utilizing edge elements and nodal elements on Powell-Sabin triangulations are compared. The approximate eigenvalues that are obtained by employing FEM using edge elements together with the convergence rates are given in Table 4.10.

Table 4.10: The first ten reference and approximated eigenvalues using edge elements on a sequence of Powell-Sabin meshes with the convergence rates.

Reference Eigenvalues	N = 4	N = 8	N = 16	N = 32	N = 64
1.03407	0.92707	0.97912 (1.0)	1.00617 (1.0)	1.02001 (1.0)	1.02701 (1.0)
2.46740	2.46619	2.46743 (5.6)	2.46745 (-1.0)	2.46742 (1.5)	2.46741 (1.8)
4.04693	4.03756	4.04446 (1.9)	4.04630 (2.0)	4.04677 (2.0)	4.04689 (2.0)
9.86960	9.83673	9.86881 (5.4)	9.87029 (0.2)	9.86988 (1.3)	9.86969 (1.7)
9.86960	9.83911	9.86936 (6.9)	9.87037 (-1.6)	9.86990 (1.4)	9.86969 (1.8)
10.84485	10.77217	10.83281 (2.6)	10.84257 (2.4)	10.84437 (2.2)	10.84475 (2.1)
12.26490	11.68279	12.02106 (1.3)	12.15073 (1.1)	12.20923 (1.0)	12.23736 (1.0)
12.33701	12.23001	12.31106 (2.0)	12.33062 (2.0)	12.33543 (2.0)	12.33662 (2.0)
19.73921	19.19342	19.62068 (2.2)	19.71082 (2.1)	19.73219 (2.0)	19.73746 (2.0)
21.24411	20.07198	20.79632 (1.4)	21.03868 (1.1)	21.14429 (1.0)	21.19472 (1.0)
zeros	77	345	1457	5985	24257
DOF	268	1112	4528	18272	73408

The results in Table 4.10 show the expected convergence behaviors as in the criss-cross mesh case shown in the previous subsection.

Next, based on the study [19], the standard finite element formulation (4.16) is considered with the finite-dimensional subspace $\mathfrak{U}_h = \mathbf{P}_1(\mathfrak{T}_h^{\text{ps}}) \cap H_0(\text{curl}; \Omega)$ where $\mathbf{P}_1(\mathfrak{T}_h^{\text{ps}})$ is the vector-valued space of first-order Lagrange basis functions defined on Powell-Sabin triangulations. It is important to emphasize that the degrees of freedom are related to the vertices of the mesh, and the homogeneous Dirichlet boundary conditions are imposed, including the tip of the crack, where the nodes on the crack are doubled to allow discontinuity. The results of nonzero approximate eigenvalues with the convergence rates obtained from the nodal FEM are given in Table 4.11.

Considering Table 4.10 and Table 4.11, the results of both approximations are convergent and validate the related theories. The convergence rates of nodal-based approximations are quadratic after the mesh is fine enough, except for some eigenvalues discussed above. However, the convergence rates of edge-based approximations vary

Table 4.11: The first ten reference and approximated eigenvalues using nodal elements on a sequence of Powell-Sabin meshes with the convergence rates.

Reference Eigenvalues	N = 4	N = 8	N = 16	N = 32	N = 64
1.03407	0.74638	0.87712 (0.9)	0.95194 (0.9)	0.99204 (1.0)	1.01281 (1.0)
2.46740	2.36898	2.44378 (2.1)	2.46158 (2.0)	2.46595 (2.0)	2.46704 (2.0)
4.04693	4.08067	4.05810 (1.6)	4.04999 (1.9)	4.04772 (1.9)	4.04713 (2.0)
9.86960	10.15882	9.94696 (1.9)	9.88917 (2.0)	9.87451 (2.0)	9.87083 (2.0)
9.86960	10.17006	9.94745 (1.9)	9.88920 (2.0)	9.87451 (2.0)	9.87083 (2.0)
10.84485	11.15079	10.93483 (1.8)	10.86812 (2.0)	10.85073 (2.0)	10.84633 (2.0)
12.26490	11.28987	11.70011 (0.8)	11.95953 (0.9)	12.10596 (0.9)	12.18380 (1.0)
12.33701	12.42849	12.39541 (0.6)	12.35338 (1.8)	12.34118 (2.0)	12.33805 (2.0)
19.73921	20.13388	20.03430 (0.4)	19.81674 (1.9)	19.75879 (2.0)	19.74411 (2.0)
21.24411	20.56615	20.41823 (-0.3)	20.74111 (0.7)	20.96971 (0.9)	21.10120 (0.9)
zeros	34	168	724	2988	12124
DOF	187	763	3067	12283	49147

and produce more accurate results than the nodal-based approximation on the same mesh. On the other hand, more degrees of freedom are involved in the edge FEM approximation than the nodal one. Even though both approximations have advantages and disadvantages, these approaches provide accurate results on the two-dimensional domain containing a strong singularity.

4.2.3.1.5 Square Domain with Two Different Materials The Maxwell EVP is approximated on domain $\Omega_4 = [-1, 1]^2$ having a non-homogeneous material property (see, Figure 4.14). The material properties are denoted by ϵ_{r_m}, μ_{r_m}, $m = 1, 2$ for each material. Numerical results are presented for two cases using uniform, criss-cross, and unstructured meshes that are shown in Figure 4.4.

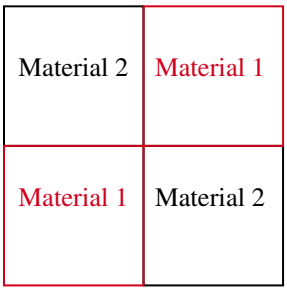


Figure 4.14: Square domain with two different materials.

The numerical tests on domain Ω_4 consist of three cases, which are:

- **Case I:** $\mu_{r_1} = \mu_{r_2} = \epsilon_{r_2} = 1$, and $\epsilon_{r_1} = 0.5$.
- **Case II:** $\mu_{r_1} = \mu_{r_2} = \epsilon_{r_2} = 1$, and $\epsilon_{r_1} = 0.1$.

In these cases, the relative permittivity values are artificial and they are taken so that the method's efficacy can be validated in the case of a singularity coming from material properties. The reference eigenvalues presented in the benchmark [40] and the benchmark contours of eigenfunctions given in [34] are considered to validate.

Case I: $\mu_{r_1} = \mu_{r_2} = \epsilon_{r_2} = 1$ and $\epsilon_{r_1} = 0.5$.

The results of first ten approximate eigenvalues on uniform, criss-cross, and unstructured meshes are given in Table 4.12, Table 4.13, and Table 4.14, respectively.

Table 4.12: The first ten reference and approximated eigenvalues on a sequence of uniform meshes with the convergence rates ($\epsilon_{r_1} = 0.5$).

Reference Eigenvalues	N = 4	N = 8	N = 16	N = 32	N = 64
3.3175	3.2462	3.2978(1.9)	3.3122(1.9)	3.3161(2.0)	3.3171(2.1)
3.3663	3.2578	3.3269(1.5)	3.3521(1.5)	3.3613(1.5)	3.3646(1.5)
6.1864	6.1823	6.1893(0.5)	6.1874(1.6)	6.1866(2.0)	6.1865(2.2)
13.9263	12.8589	13.6778(2.1)	13.8649(2.0)	13.9109(2.0)	13.9225(2.0)
15.0829	14.0947	14.8544(2.1)	15.0251(2.0)	15.0684(2.0)	15.0793(2.0)
15.7789	14.4520	15.4372(2.0)	15.6910(2.0)	15.7565(2.0)	15.7732(2.0)
18.6433	17.8104	18.6213(5.2)	18.6448(3.9)	18.6437(2.0)	18.6433(3.5)
25.7975	23.3400	25.2141(2.1)	25.6619(2.1)	25.7643(2.0)	25.7893(2.0)
29.8524	27.3159	29.1609(1.9)	29.6734(1.9)	29.8067(2.0)	29.8409(2.0)
30.5379	28.0668	29.7940(1.7)	30.3201(1.8)	30.4733(1.8)	30.5185(1.7)
zeros	9	48	225	961	3969
DOF	40	176	736	3008	12160

In this case, the convergence rates of approximate eigenvalues are not quadratic for all, even when uniform and criss-cross meshes are used in a convex domain, as can be seen in Table 4.12 and Table 4.13. This behavior of approximate eigenvalues results from the formed singularity in a domain because of the parameters.

Table 4.13: The first ten reference and approximated eigenvalues on a sequence of criss-cross meshes with the convergence rates ($\epsilon_{r_1} = 0.5$).

Reference Eigenvalues	N = 4	N = 8	N = 16	N = 32	N = 64
3.3175	3.3126	3.3169(2.9)	3.3172(1.2)	3.3174(2.2)	3.3175(1.9)
3.3663	3.3181	3.3457(1.2)	3.3587(1.4)	3.3636(1.5)	3.3654(1.5)
6.1864	6.1046	6.1662(2.0)	6.1814(2.0)	6.1851(2.0)	6.1861(2.0)
13.9263	13.9785	13.9516(1.0)	13.9333(1.9)	13.9281(2.0)	13.9268(1.9)
15.0829	15.1648	15.1089(1.7)	15.0896(2.0)	15.0846(1.9)	15.0834(1.8)
15.7789	15.4880	15.7168(2.2)	15.7633(2.0)	15.7749(2.0)	15.7778(1.9)
18.6433	18.0223	18.5116(2.2)	18.6109(2.0)	18.6350(2.0)	18.6411(1.9)
25.7975	24.1154	25.4240(2.2)	25.7071(2.0)	25.7751(2.0)	25.7919(2.0)
29.8524	30.6613	30.0687(1.9)	29.9080(2.0)	29.8662(2.0)	29.8558(2.0)
30.5379	31.2220	30.6223(3.0)	30.5448(3.6)	30.5342(0.9)	30.5351(0.4)
zeros	25	113	481	1985	8065
DOF	88	368	1504	6080	24448

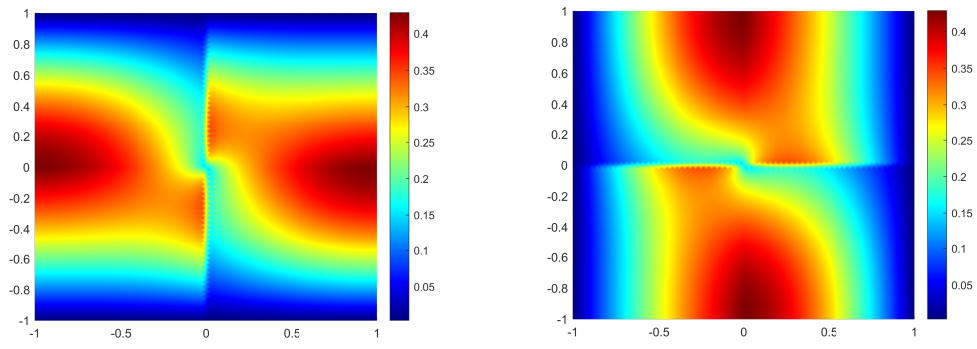
Also, looking at Table 4.14, in the unstructured mesh, accurate approximate eigenvalues are obtained with varying convergence rates as usual.

Table 4.14: The first ten reference and approximated eigenvalues on a sequence of unstructured meshes with the convergence rates ($\epsilon_{r_1} = 0.5$).

Reference Eigenvalues	h_{max} = 0.7	h_{max} = 0.331	h_{max} = 0.1628	h_{max} = 0.0814	h_{max} = 0.0407
3.3175	3.1628	3.3615(1.7)	3.3199(4.1)	3.3146(-0.3)	3.3173(4.1)
3.3663	3.4241	3.4098(0.4)	3.3802(1.6)	3.3577(0.7)	3.3643(2.1)
6.1864	6.3847	6.2570(1.4)	6.1921(3.6)	6.1896(0.8)	6.1887(0.5)
13.9263	12.8595	13.8978(4.8)	13.8938(-0.2)	13.9061(0.7)	13.9197(1.6)
15.0829	15.6584	15.0666(4.8)	15.0413(-1.3)	15.0541(0.5)	15.0746(1.8)
15.7789	16.5203	15.8322(3.5)	15.7923(2.0)	15.7617(-0.4)	15.7731(1.6)
18.6433	18.2280	18.6489(5.8)	18.6338(-0.8)	18.6433(8.7)	18.6461(-6.9)
25.7975	29.4615	25.7844(7.5)	25.7529(-1.7)	25.7438(-0.3)	25.7807(1.7)
29.8524	29.6292	29.9476(1.1)	29.8569(4.3)	29.8115(-3.2)	29.8428(2.1)
30.5379	30.4979	30.6021(-0.6)	30.6711(-1.0)	30.5053(2.0)	30.5350(3.5)
zeros	9	49	226	988	4006
DOF	36	172	727	3061	12215

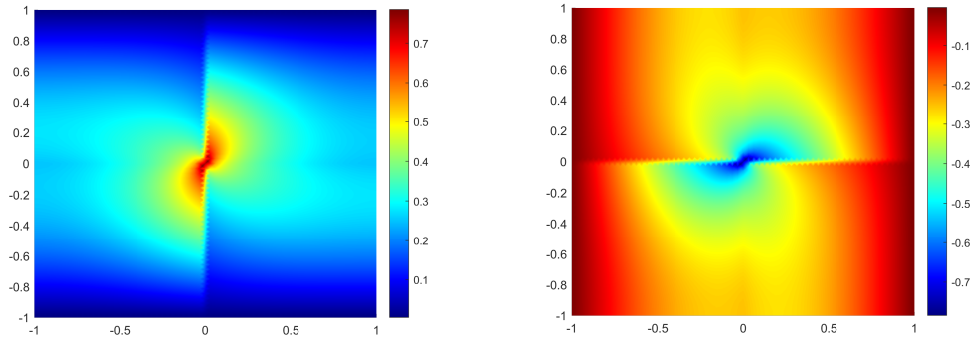
The numerical results show that the method provides accurate approximations in a domain that contains a singularity coming from the parameters.

For the first case, the contours of the approximated eigenfunctions are presented in Figure 4.15. As seen these figures, the second eigenfunction has a singularity around the point $(0, 0)$, and this leads to lower than quadratic convergence rate for the second approximate eigenvalue, which can be seen in Table 4.12 and Table 4.13. Besides this, the rest of the first five eigenfunctions are regular, and their corresponding approximate eigenvalues converge with a quadratic convergence rate.

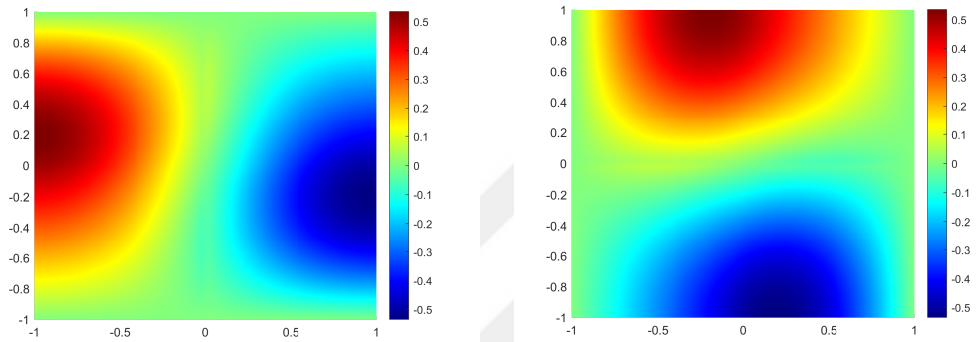


(a) $\mathbf{u}^1_{h_x}$ (b) $\mathbf{u}^1_{h_y}$

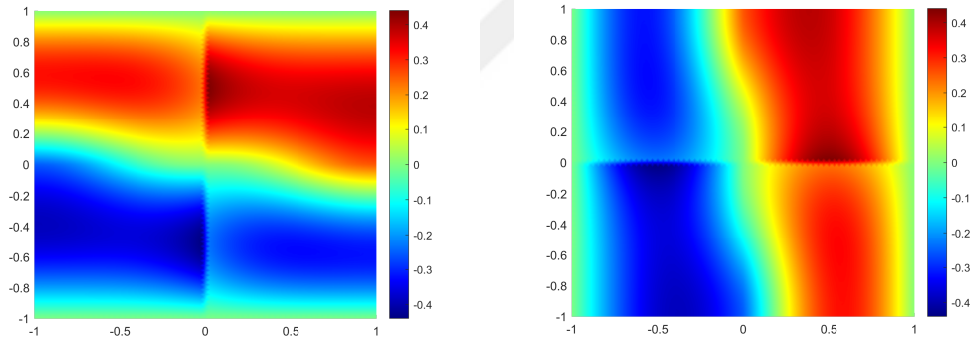
Figure 4.15: Contours of the first five approximated eigenfunctions using criss-cross mesh with 24416 DOF on Ω_4 ($\epsilon_{r_1} = 0.5$).



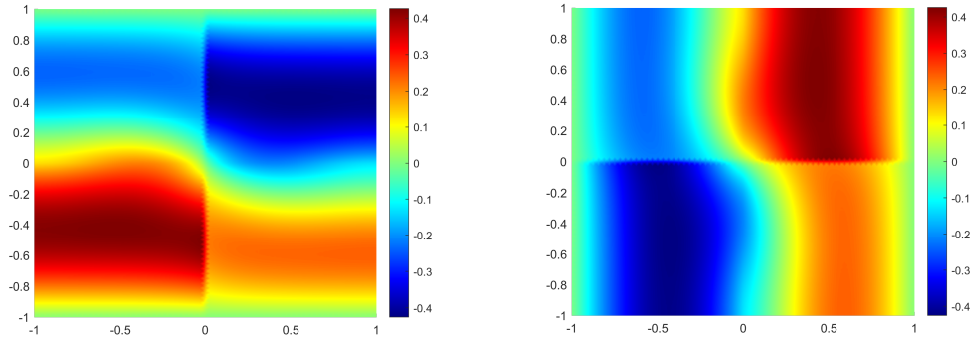
(c) $\mathbf{u}_{h_x}^2$ (d) $\mathbf{u}_{h_y}^2$



(e) $\mathbf{u}_{h_x}^3$ (f) $\mathbf{u}_{h_y}^3$



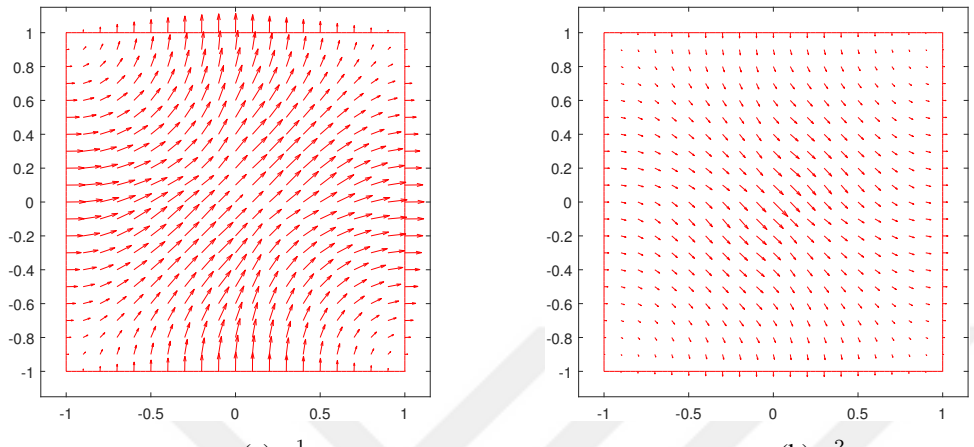
(g) $\mathbf{u}_{h_x}^4$ (h) $\mathbf{u}_{h_y}^4$



(i) $\mathbf{u}_{h_x}^5$ (j) $\mathbf{u}_{h_y}^5$

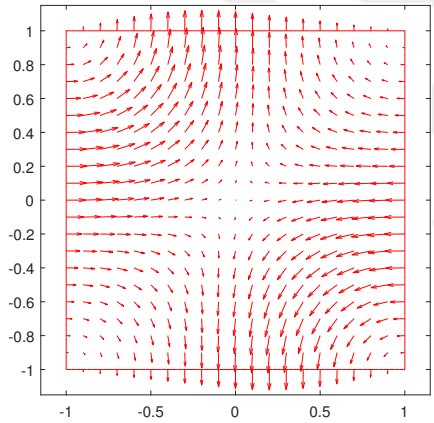
Figure 4.15: Contours of the first five approximated eigenfunctions using criss-cross mesh with 24416 DOF on Ω_4 ($\epsilon_{r_1} = 0.5$). (cont.)

Moreover, the vector fields of eigenfunctions are presented in Figure 4.16. In these figures, the eigenfunctions are partially similar to the eigenfunctions of the square domain with homogeneous material property, which are given in Figure 4.6. However, the effect of the inhomogeneous material property dramatically changes some of the eigenfunctions, for instance, the second and the fifth ones.

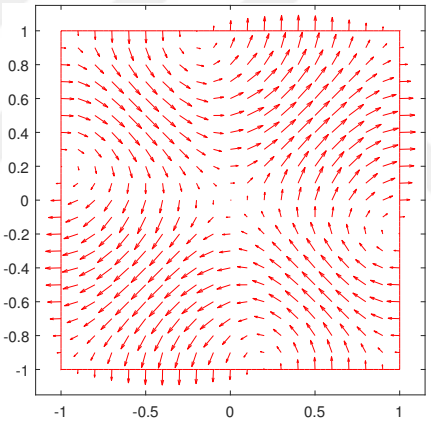


(a) $\mathbf{u}_h^1$

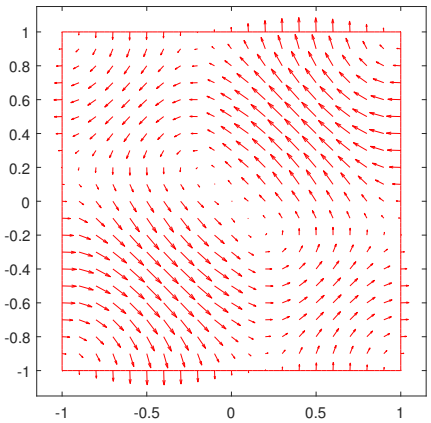
(b) $\mathbf{u}_h^2$



(c) $\mathbf{u}_h^3$



(d) $\mathbf{u}_h^4$



(e) $\mathbf{u}_h^5$

Figure 4.16: Quivers of the first five approximated eigenfunctions using criss-cross mesh with 24416 DOF on Ω_4 ($\epsilon_{r_1} = 0.5$).

Case II: $\mu_{r_1} = \mu_{r_2} = \epsilon_{r_2} = 1$ and $\epsilon_{r_1} = 0.1$.

In this case, it is expected that the regularity of eigenfunctions that had low regularity in the first case will be decreased even more with the decreasing value of ϵ_{r_1}, since the singularity around the point $(0, 0)$ becomes stronger.

Table 4.15, Table 4.16, and Table 4.17 present the approximate eigenvalues after eliminating the zero eigenvalues on a sequence of three different meshes in the following.

Table 4.15: The first ten reference and approximated eigenvalues on a sequence of uniform meshes with the convergence rates ($\epsilon_{r_1} = 0.1$).

Reference Eigenvalues	N = 4	N = 8	N = 16	N = 32	N = 64
4.5339	4.4923	4.5245(2.1)	4.5314(1.9)	4.5332(1.9)	4.5337(1.7)
6.2503	4.5787	5.1161(0.6)	5.5283(0.7)	5.8093(0.7)	5.9870(0.7)
7.0371	7.0697	7.0487(1.5)	7.0401(1.9)	7.0378(2.0)	7.0373(2.2)
22.3419	18.8850	21.7271(2.5)	22.2613(2.9)	22.3226(2.1)	22.3372(2.0)
22.6792	19.7049	21.9615(2.1)	22.4347(1.6)	22.6174(2.0)	22.6637(2.0)
26.0952	23.1896	25.6683(2.8)	25.9461(1.5)	26.0229(1.0)	26.0559(0.9)
26.5090	23.2312	25.6698(2.0)	26.2926(2.0)	26.4544(2.0)	26.4953(2.0)
40.4878	37.9470	40.9432(2.5)	40.6636(1.4)	40.5354(1.9)	40.500(2.0)
42.6507	38.9771	43.3365(2.4)	42.9157(1.4)	42.7215(1.9)	42.6686(2.0)
55.8823	66.6656	50.5431(1.0)	54.6522(2.1)	55.5787(2.0)	55.8066(2.0)
zeros	9	48	225	961	3969
DOF	40	176	736	3008	12160

Table 4.16: The first ten reference and approximated eigenvalues on a sequence of criss-cross meshes with the convergence rates ($\epsilon_{r_1} = 0.1$).

Reference Eigenvalues	N = 4	N = 8	N = 16	N = 32	N = 64
4.5339	4.4721	4.5178(1.9)	4.5298(2.0)	4.5328(1.9)	4.5336(1.8)
6.2503	4.7451	5.3032(0.7)	5.6742(0.7)	5.9064(0.7)	6.0472(0.8)
7.0371	6.9892	7.0252(2.0)	7.0341(2.0)	7.0363(2.0)	7.0369(1.9)
22.3419	21.7969	22.2655(2.8)	22.3254(2.2)	22.3380(2.1)	22.3410(2.1)
22.6792	22.1042	22.5928(2.7)	22.6595(2.1)	22.6743(2.0)	22.6780(2.0)
26.0952	26.0953	26.0309(-9.7)	26.0338(0.1)	26.0522(0.5)	26.0681(0.7)
26.5090	26.5843	26.5521(0.8)	26.5217(1.8)	26.5123(1.9)	26.5098(2.0)
40.4878	34.5312	39.0211(2.0)	40.1198(2.0)	40.3957(2.0)	40.4648(2.0)
42.6507	35.9017	41.0912(2.1)	42.2618(2.0)	42.5533(2.0)	42.6263(2.0)
55.8823	54.7233	55.7952(3.7)	55.9229(1.1)	55.8956(1.6)	55.8858(1.9)
zeros	25	113	481	1985	8065
DOF	88	368	1504	6080	24448

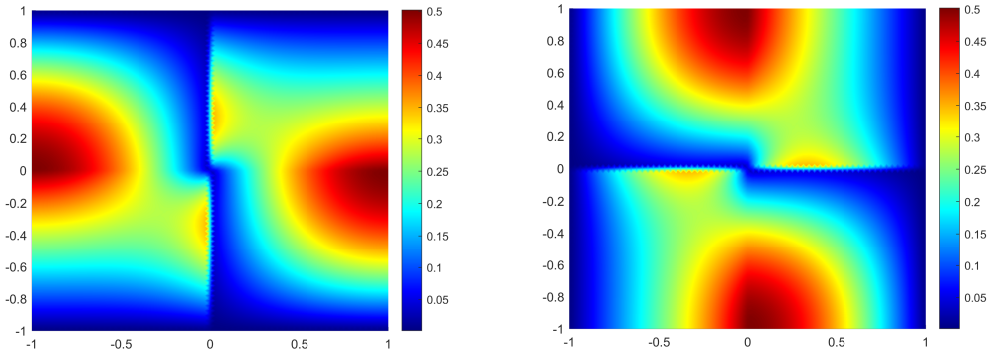
As seen from Table 4.15 and Table 4.16, the convergence rates are quadratic for most of the eigenvalues when the uniform and criss-cross meshes are used. However, it is observed that the convergence rates decrease dramatically for the second and sixth eigenvalues when the value of ϵ_{r_1} decreases compared with the first case. The reason is the occurrence of singularity in the asymptotics of the corresponding eigenfunction at $(0, 0)$ [40].

Table 4.17: The first ten reference and approximated eigenvalues on a sequence of unstructured meshes with the convergence rates ($\epsilon_{r_1} = 0.1$).

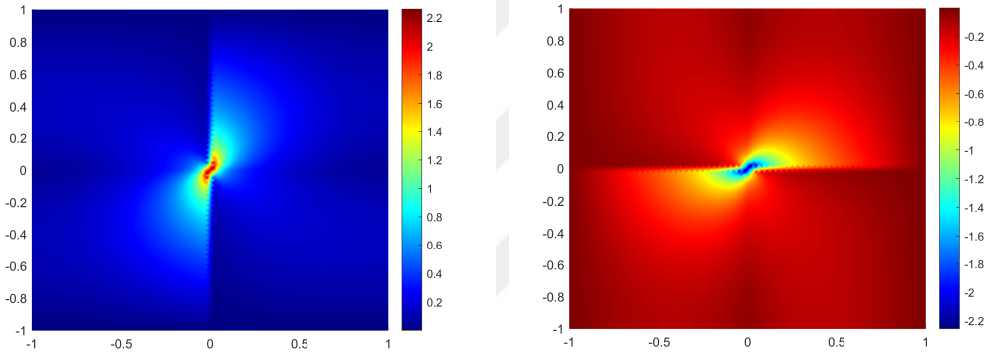
Reference Eigenvalues	h_{max} = 0.7	h_{max} = 0.331	h_{max} = 0.1628	h_{max} = 0.0814	h_{max} = 0.0407
4.5339	4.2499	4.6907(0.8)	4.5482(3.4)	4.5380(1.8)	4.5399(-0.6)
6.2503	4.9032	5.5221(0.8)	5.8785(0.9)	5.8522(-0.1)	6.0989(1.4)
7.0371	7.5563	7.2602(1.1)	7.0652(2.9)	7.0480(1.4)	7.0454(0.4)
22.3419	20.4167	22.4779(3.5)	22.3405(6.5)	22.3328(-2.7)	22.3656(-1.4)
22.6792	23.1155	23.1195(0.0)	22.6778(8.1)	22.6554(-4.0)	22.6961(0.5)
26.0952	32.0775	27.1655(2.3)	26.1705(3.7)	26.1071(2.7)	26.1224(-1.2)
26.5090	36.3014	27.3017(3.4)	26.5827(3.3)	26.5400(2.7)	26.5460(-1.2)
40.4878	44.9938	40.3531(4.7)	40.3385(-0.1)	40.2887(-0.4)	40.4330(1.9)
42.6507	46.7377	43.9648(1.5)	42.7355(3.9)	42.6031(0.8)	42.6478(4.0)
55.8823	60.9993	53.7116(1.1)	55.5082(2.5)	55.7289(1.3)	55.8835(6.9)
zeros	9	49	226	988	4006
DOF	36	172	727	3061	12215

On the other hand, in the sequence of unstructured meshes, the approximate eigenvalues are closer to the reference ones for the second and sixth eigenvalues, even though the convergence rates vary, as seen in Table 4.17.

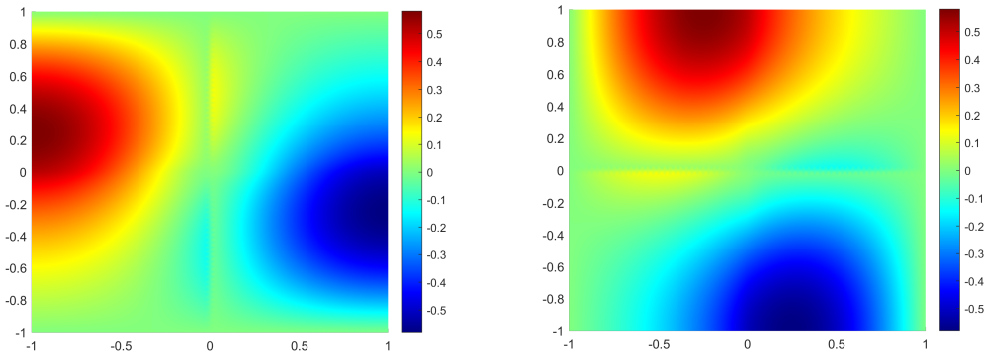
The contours of the first five approximated eigenfunctions are presented in Figure 4.17 for the second case. The approximate eigenfunctions presented in this figure agree with the benchmark contours given in [34]. It can also be observed that the singularity of the second eigenfunction becomes stronger compared with the first case, as expected. Next, the vector fields of eigenfunctions given in Figure 4.18 are considered. The dramatic change in the first five eigenfunctions is observed compared with the first case, and it can be seen mainly in the second and the fifth eigenfunctions, as it was already distinguished in the first case.



(a) $\mathbf{u}_{h_x}^1$ (b) $\mathbf{u}_{h_y}^1$

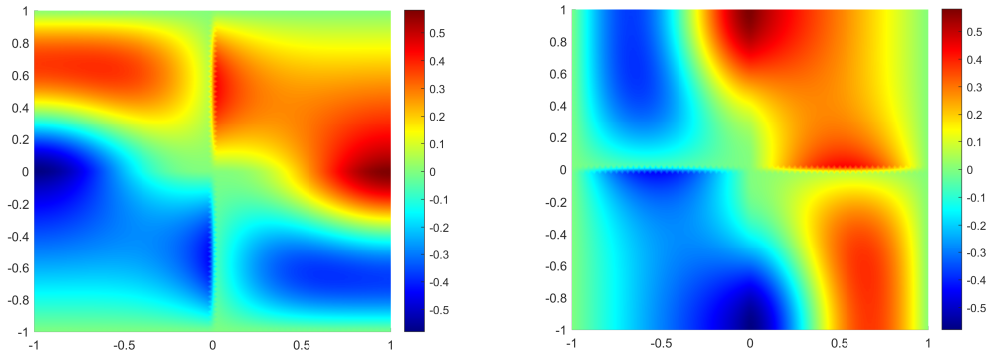


(c) $\mathbf{u}_{h_x}^2$ (d) $\mathbf{u}_{h_y}^2$

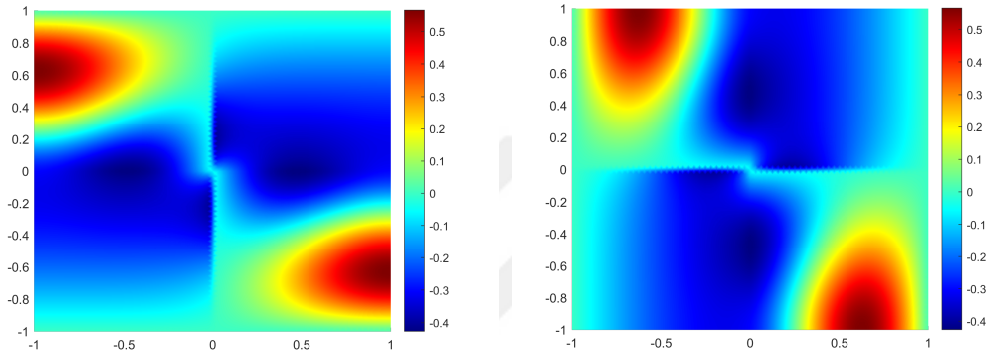


(e) $\mathbf{u}_{h_x}^3$ (f) $\mathbf{u}_{h_y}^3$

Figure 4.17: Contours of the first five approximated eigenfunctions using criss-cross mesh with 24416 DOF on Ω_4 ($\epsilon_{r_1} = 0.1$).

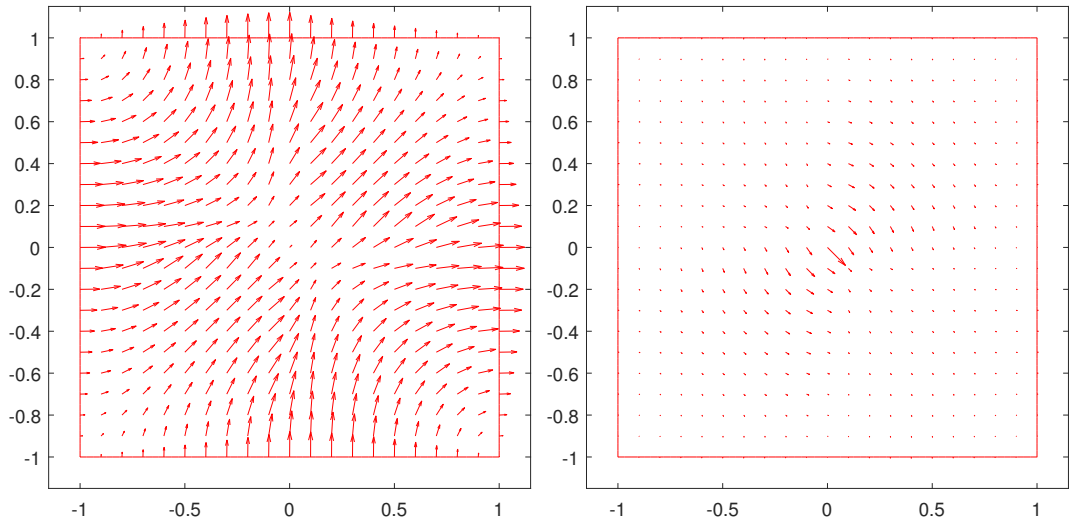


(g) $\mathbf{u}_{h_x}^4$ (h) $\mathbf{u}_{h_y}^4$



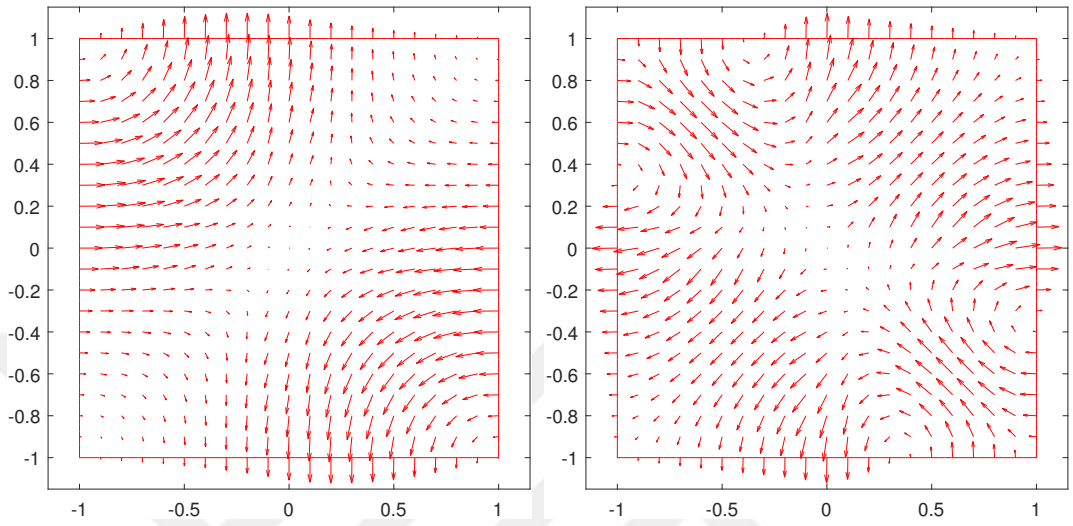
(i) $\mathbf{u}_{h_x}^5$ (j) $\mathbf{u}_{h_y}^5$

Figure 4.17: Contours of the first five approximated eigenfunctions using criss-cross mesh with 24416 DOF on Ω_4 ($\epsilon_{r_1} = 0.1$). (cont.)

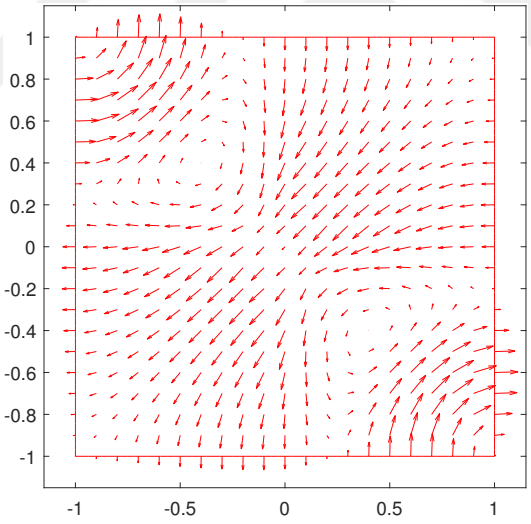


(a) $\mathbf{u}_h^1$ (b) $\mathbf{u}_h^2$

Figure 4.18: Quivers of the first five approximated eigenfunctions using criss-cross mesh with 24416 DOF on Ω_4 ($\epsilon_{r_1} = 0.1$).



(c) $\mathbf{u}_h^3$ (d) $\mathbf{u}_h^4$



(e) $\mathbf{u}_h^5$

Figure 4.18: Quivers of the first five approximated eigenfunctions using criss-cross mesh with 24416 DOF on Ω_4 ($\epsilon_{r_1} = 0.1$).

4.2.3.1.6 Rectangular Domain with Two Different Materials

The Maxwell EVP is approximated on domain $\Omega_5 = [0,1] \times [0,0.6]$ having a non-homogeneous material property. The material properties are denoted by ϵ_{r_m}, μ_{r_m}, $m = 1,2$ for each material that are located as given in Figure 4.19. The material parameters are $\epsilon_{r_1} = \mu_{r_1} = \mu_{r_2} = 1$, and $\epsilon_{r_2} = 6$.

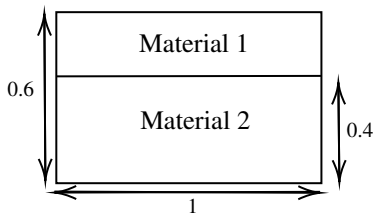


Figure 4.19: Rectangle domain with two different materials.

This example is used as a test case for dielectric-loaded waveguides in the literature, which involves the Maxwell EVP for finding cutoff wavenumbers and modes [61, 83]. In Table 4.18, the first five approximate cutoff wavenumbers (square root of eigenvalues) are presented to compare them with the analytical ones provided in [61].

Table 4.18: The first five analytical and approximated cutoff wavenumbers on the uniform, criss-cross, and unstructured meshes.

Analytical	N = 64 Uniform	N = 64 Criss-Cross	$h_{max} = 0.0407$ Unstructured
1.7666	1.7597	1.7631	1.7654
2.3053	2.2980	2.3035	2.3054
2.9548	2.9495	2.9528	2.9549
3.2987	3.2885	3.2913	3.2948
4.1380	4.1343	4.1370	4.1387
zeros	3969	8065	3526
DOF	12160	2448	12215

As can be seen in Table 4.18, the approximations are accurate when compared with the analytical ones. The results of unstructured mesh are closer to the analytical cutoff wavenumbers in this case.

Next, the squares of analytical cutoff wavenumbers are obtained to consider approximate eigenvalues and corresponding convergence rates on a sequence of different triangulations. Therefore, Table 4.19 and Table 4.20 present the approximate eigenvalues on a sequence of uniform and criss-cross meshes, respectively.

Table 4.19: The first five analytical and approximated eigenvalues on a sequence of uniform meshes with the convergence rates.

Analytical	N = 4	N = 8	N = 16	N = 32	N = 64
3.1209	2.7579	2.9104 (0.8)	3.0252 (1.1)	3.0692 (0.9)	3.0966 (1.1)
5.3144	4.7265	5.1210 (1.6)	5.1777 (0.5)	5.2772 (1.9)	5.2810 (0.2)
8.7308	8.3530	8.5753 (1.3)	8.6165 (0.4)	8.6840 (1.3)	8.6993 (0.6)
10.8814	9.5137	9.9905 (0.6)	10.5971 (1.6)	10.6717 (0.4)	10.8142 (1.6)
17.1230	16.3340	17.0519 (3.5)	17.0282 (-0.4)	17.0856 (1.3)	17.0923 (0.3)
zeros	9	48	225	961	3969
DOF	40	176	736	3008	12160

Table 4.20: The first five analytical and approximated eigenvalues on a sequence of criss-cross meshes with the convergence rates.

Analytical	N = 4	N = 8	N = 16	N = 32	N = 64
3.1209	2.9415	3.1373 (3.5)	3.0727 (-1.6)	3.1244 (3.8)	3.1086 (-1.8)
5.3144	5.1714	5.3759 (1.2)	5.2804 (0.9)	5.3306 (1.1)	5.3060 (0.9)
8.7308	8.6136	8.7884 (1.0)	8.6866 (0.4)	8.7430 (1.9)	8.7193 (0.1)
10.8814	9.9261	10.7882 (3.4)	10.6770 (-1.1)	10.8666 (3.8)	10.8325(-1.7)
17.1230	17.5148	17.3297 (0.9)	17.1173 (5.2)	17.1469 (-2.1)	17.1148 (1.5)
zeros	25	113	481	1985	8065
DOF	88	368	1504	6080	24448

It is observed from Table 4.19 and Table 4.20 that the convergence rates are not quadratic in uniform triangulations of the convex domain. As already mentioned in the previous cases, this results from a singularity in the domain coming from the material parameters. Moreover, the numerical results on a sequence of unstructured meshes are shown in Table 4.21.

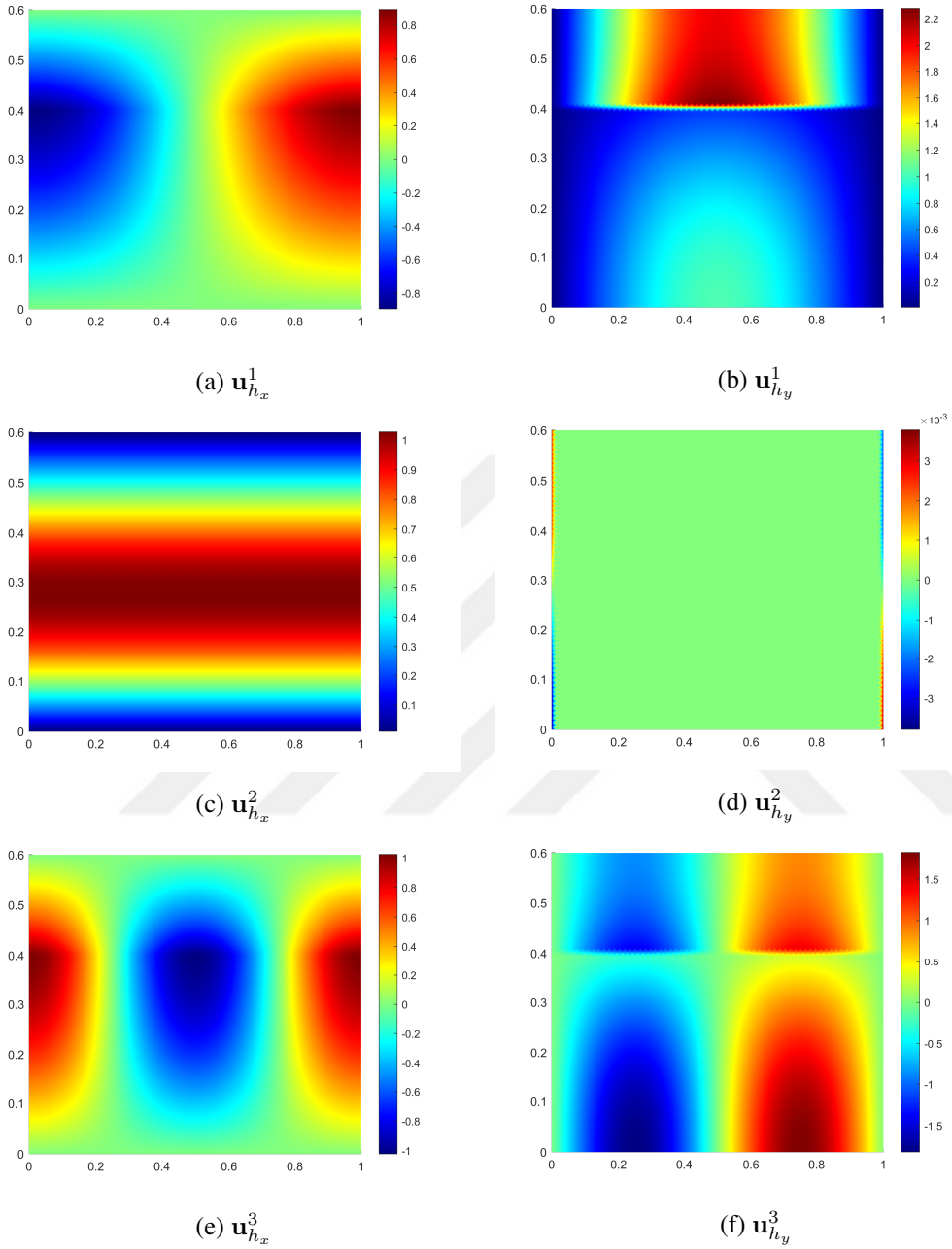
Table 4.21: The first five analytical and approximated eigenvalues on a sequence of unstructured meshes with the convergence rates.

Analytical	$h_{max} = 0.7$	$h_{max} = 0.331$	$h_{max} = 0.1628$	$h_{max} = 0.0814$	$h_{max} = 0.0407$
3.1209	3.0949	3.1254 (2.5)	3.1142 (-0.6)	3.1095 (-0.8)	3.1168 (1.5)
5.3144	5.2460	5.3379 (1.5)	5.3152 (4.9)	5.3171 (-1.8)	5.3149 (2.6)
8.7308	8.7923	8.7262 (3.7)	8.7448 (-1.6)	8.7265 (1.7)	8.7314 (3.0)
10.8814	10.3743	10.9355 (3.2)	10.8156 (-0.3)	10.8032 (-0.2)	10.8556 (1.6)
17.1230	20.4894	17.2934 (4.3)	17.1700 (1.9)	17.1403 (1.4)	17.1289 (1.6)
zeros	9	49	229	988	3526
DOF	36	172	736	3061	12215

Table 4.21 shows that the unstructured triangulation of Ω_5 provides the best approximations compared to the results of the other two triangulations for this case.

The contours of each component for the first five eigenfunctions are presented in Figure 4.20. In the considered studies for this case, there are no visuals of eigenfunc-

tions. Therefore, the contours are presented without comparison since the validation is confirmed by comparing the approximate and analytical cutoff wavenumbers.

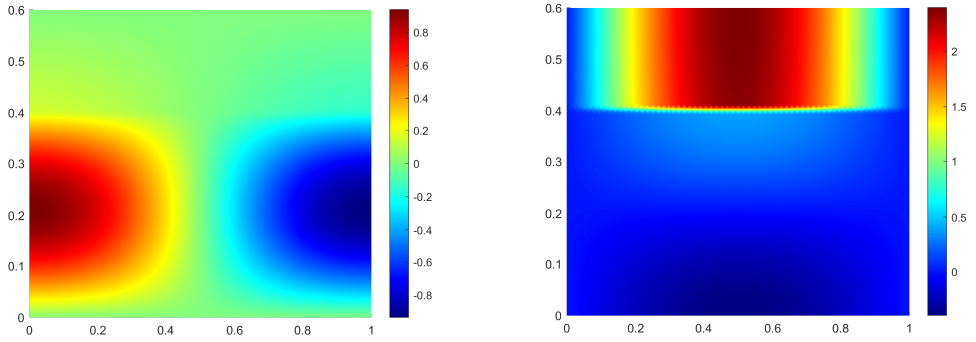


(a) $\mathbf{u}^1_{h_x}$ (b) $\mathbf{u}^1_{h_y}$

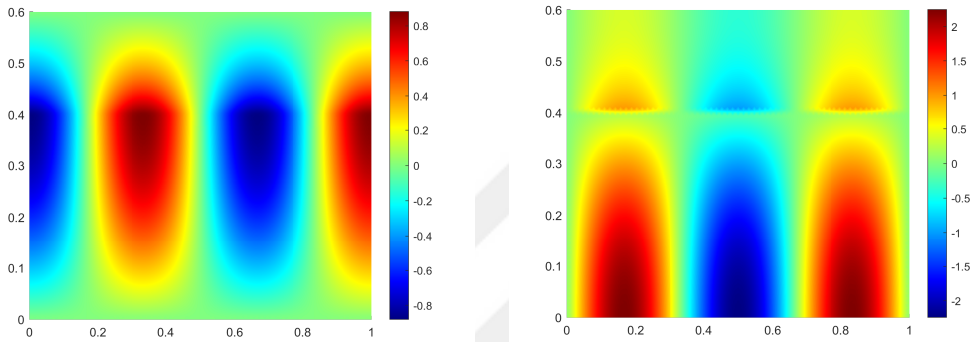
(c) $\mathbf{u}^2_{h_x}$ (d) $\mathbf{u}^2_{h_y}$

(e) $\mathbf{u}^3_{h_x}$ (f) $\mathbf{u}^3_{h_y}$

Figure 4.20: Contours of the first five approximated eigenfunctions using criss-cross mesh with 24416 DOF on Ω_5.



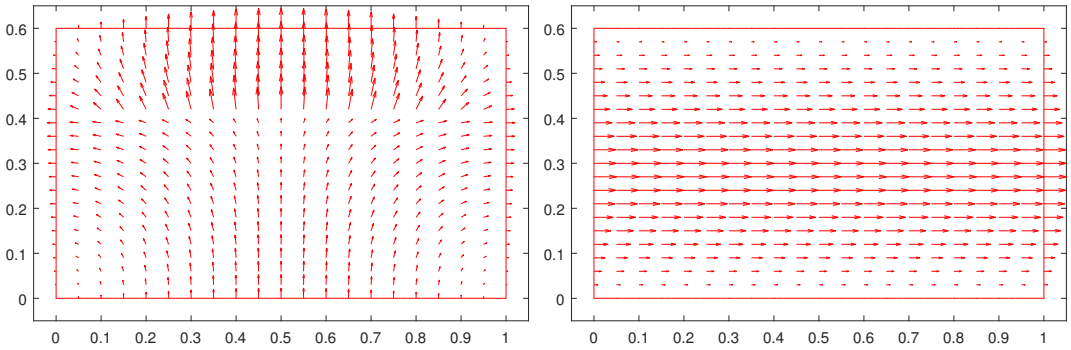
(g) $\mathbf{u}_{h_x}^4$ (h) $\mathbf{u}_{h_y}^4$



(i) $\mathbf{u}_{h_x}^5$ (j) $\mathbf{u}_{h_y}^5$

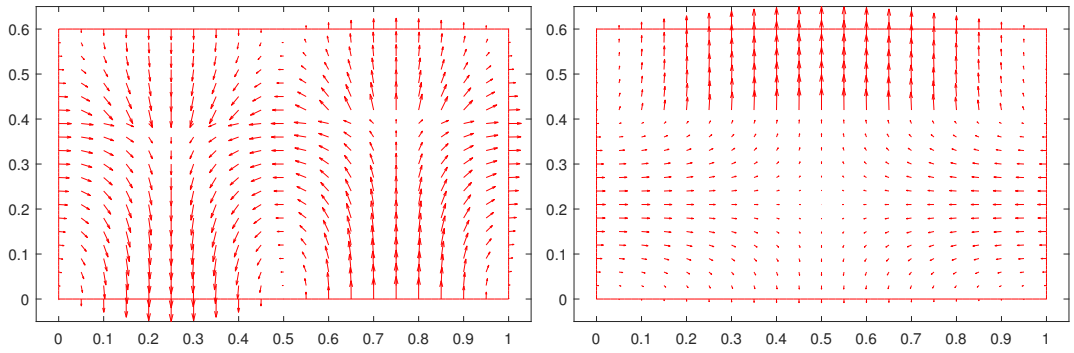
Figure 4.20: Contours of the first five approximated eigenfunctions using criss-cross mesh with 24448 DOF on Ω_5. (cont.)

Additionally, the vector fields of these eigenfunctions are given in Figure 4.21, where these fields are divergence-free and have zero tangential components on the boundary.



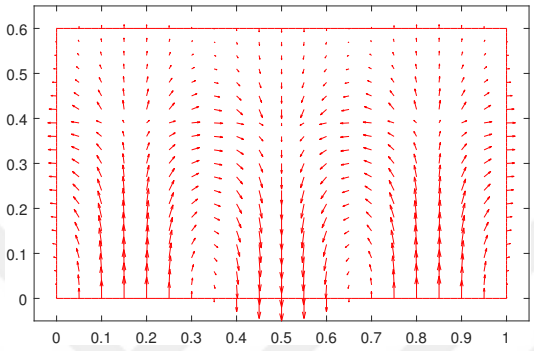
(a) $\mathbf{u}_h^1$ (b) $\mathbf{u}_h^2$

Figure 4.21: Quivers of the first five approximated eigenfunctions using criss-cross mesh with 24416 DOF on Ω_5.



(c) $\mathbf{u}_h^3$

(d) $\mathbf{u}_h^4$



(e) $\mathbf{u}_h^5$

Figure 4.21: Quivers of the first five approximated eigenfunctions using criss-cross mesh with 24416 DOF on Ω_5. (cont.)

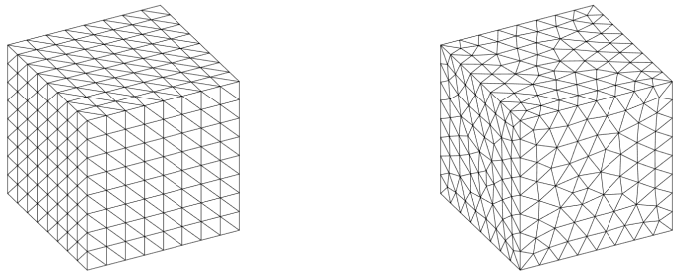
4.2.3.2 Numerical Results of 3D Domains

The numerical results of finite element approximation of Maxwell EVP introduced in (2.21) using Nédélec basis functions in three-dimensional domains are presented. In the numerical experiments, procedures made for two-dimensional domains are followed similarly, with modifications to the visualization process.

The visualization of eigenfunctions is performed in two steps. Firstly, eigenfunctions ($\mathbf{u}_h^n$) are obtained following the same steps given in (4.39), where the global basis functions are computed at the centroid of tetrahedrons (elements) in the mesh. Next, to visualize the eigenfunctions in MATLAB, the nodal values are extrapolated from the RBF interpolation functions. These interpolation functions are computed following the idea studied in [95].

As mentioned earlier, for the validation of the constructed frame that can handle extension to the third dimension, tests on 3D domains are included. Numerical tests in 3D domains consist of cube domain Ω_6, thick L-shape domain Ω_7, and Fichera corner domain Ω_8. In all these numerical experiments, relative parameters $\epsilon_r = \mu_r = 1$ are considered. The cube domain is considered for the validation since the exact eigenpairs are known. Additionally, it is considered to validate the presented theory of convergence properties, where it is expected to have quadratic convergence rates for the approximate eigenvalues in uniform meshes of the 3D convex domain. Moreover, the other two domains that contain strong singularities are considered to show the method's efficacy in 3D, as it was performed in 2D cases. For the last two cases, the reference values are considered, which are provided in [40], and the approximate eigenfunctions' slice contours are presented for the comparison with the benchmark contours presented in [34].

4.2.3.2.1 Cube The Maxwell EVP on $\Omega_5 = [0, \pi]^3$ with $\epsilon_r = \mu_r = 1$ is approximated on the uniform and unstructured meshes given in Figure 4.22.



(a) $N = 8$ (b) $h_{max} = 0.1335$

Figure 4.22: Uniform and unstructured meshes of the cube domain.

The exact eigenfunctions denoted by $\mathbf{u}_{\text{cube}}$ are presented in [9] and stated as

$$\mathbf{u}_{\text{cube}} = \begin{bmatrix} d_1 \cos(ax_1)\sin(bx_2)\sin(cx_3) \\ d_2 \sin(ax_1)\cos(bx_2)\sin(cx_3) \\ d_3 \sin(ax_1)\sin(bx_2)\cos(cx_3) \end{bmatrix}, \qquad \forall \begin{bmatrix} d_1 \\ d_2 \\ d_3 \end{bmatrix} \cdot \begin{bmatrix} a \\ b \\ c \end{bmatrix} = 0, \tag{4.42}$$

where $\{a, b, c\} \subset \mathbb{N}_0$ where two of the indices are not allowed to vanish at the same time with the exact eigenvalues $\lambda = \sqrt{a^2 + b^2 + c^2}$. Here the multiplicity of the eigenvalues with respect to this consideration is determined by the vector $(d_1, d_2, d_3)^T$.

The results of first ten approximate eigenvalues on uniform and unstructured meshes are given in Table 4.22, and Table 4.23.

Table 4.22: The first eleven exact and approximated eigenvalues on a sequence of uniform meshes with the convergence rates.

Exact	N = 2	N = 4	N = 8	N = 16	N = 32
2	1.4254	1.8490(1.9)	1.9629(2.0)	1.9906(2.0)	1.9976(2.0)
2	1.4677	1.8889(2.3)	1.9657(1.7)	1.9907(1.9)	1.9977(2.0)
2	1.8841	1.9862(3.1)	1.9978(2.6)	1.9995(2.0)	1.9999(1.9)
3	2.6767	2.6035(-0.3)	2.8798(1.7)	2.9677(1.9)	2.9917(2.0)
3	2.9874	2.9015(-3.0)	2.9847(2.7)	2.9965(2.1)	2.9991(2.0)
5	3.8996	3.9539(0.1)	4.7147(1.9)	4.9238(1.9)	4.9802(1.9)
5	4.7327	3.9672(-1.9)	4.7284(1.9)	4.9260(1.9)	4.9813(2.0)
5	6.2997	4.2261(0.7)	4.7727(1.8)	4.9448(2.0)	4.9855(1.9)
5	7.2686	4.2307(1.6)	4.7989(1.9)	4.9463(1.9)	4.9868(2.0)
5	7.8402	4.5673(2.7)	4.9043(2.2)	4.9768(2.0)	4.9941(2.0)
5	7.9701	4.7757(3.7)	4.9154(1.4)	4.9799(2.1)	4.9952(2.1)
zeros	1	27	343	3375	29791
DOF	26	316	3032	26416	220256

Table 4.23: The first eleven exact and approximated eigenvalues on a sequence of unstructured meshes with the convergence rates.

Exact	$h_{max} = 0.4$	$h_{max} = 0.27$	$h_{max} = 0.1335$	$h_{max} = 0.072$	$h_{max} = 0.035$
2	1.8289	1.9557(3.4)	1.9936(2.7)	1.9991(3.2)	1.9999(3.4)
2	1.9020	1.9653(2.6)	1.9951(2.8)	1.9992(2.9)	1.9999(3.6)
2	1.9288	1.9701(2.2)	1.9967(3.1)	1.9993(2.5)	1.9999(3.5)
3	2.6280	2.8965(3.3)	2.9926(3.7)	2.9991(3.5)	3.0000(6.7)
3	2.8474	2.9292(2.0)	2.9959(4.0)	2.9997(4.4)	3.0000(3.9)
5	3.8351	4.7025(3.5)	4.9498(2.5)	4.9923(3.0)	4.9987(2.5)
5	3.9377	4.7462(3.6)	4.9544(2.4)	4.9930(3.0)	4.9989(2.5)
5	4.0426	4.7793(3.7)	4.9599(2.4)	4.9934(2.9)	4.9989(2.5)
5	4.3500	4.7904(2.9)	4.9685(2.7)	4.9940(2.7)	4.9993(2.9)
5	4.7077	4.8613(1.9)	4.9795(2.7)	4.9947(2.2)	4.9993(2.8)
5	4.8328	4.9373(2.5)	4.9829(1.8)	4.9954(2.1)	4.9993(2.7)
zeros	5	26	378	3002	29330
DOF	111	354	3366	23453	215470

The numerical results in Table 4.22 validate the theory, showing that the convergence rates are getting quadratic after the fine enough uniform mesh. On the other hand, seeing in Table 4.23, the convergence rates in a sequence of unstructured meshes are mostly higher than the quadratic, which results in better approximations of eigenvalues when compared with the uniform mesh.

The slice contours of approximate eigenfunctions' components are given in Figure 4.23 using the slices on the domain Ω_5 and the extrapolated nodal values from RBF interpolation. It should be noted that the RBF interpolation is constructed using the results of approximation at uniform mesh with $\mathrm{N} = 16$ $(\mathrm{DOF} = 26416)$. From these figures, it is observed that the approximate eigenfunctions are in good agreement with the exact eigenfunctions denoted by $\mathbf{u}_{\text{cube}}$ given in (4.42).

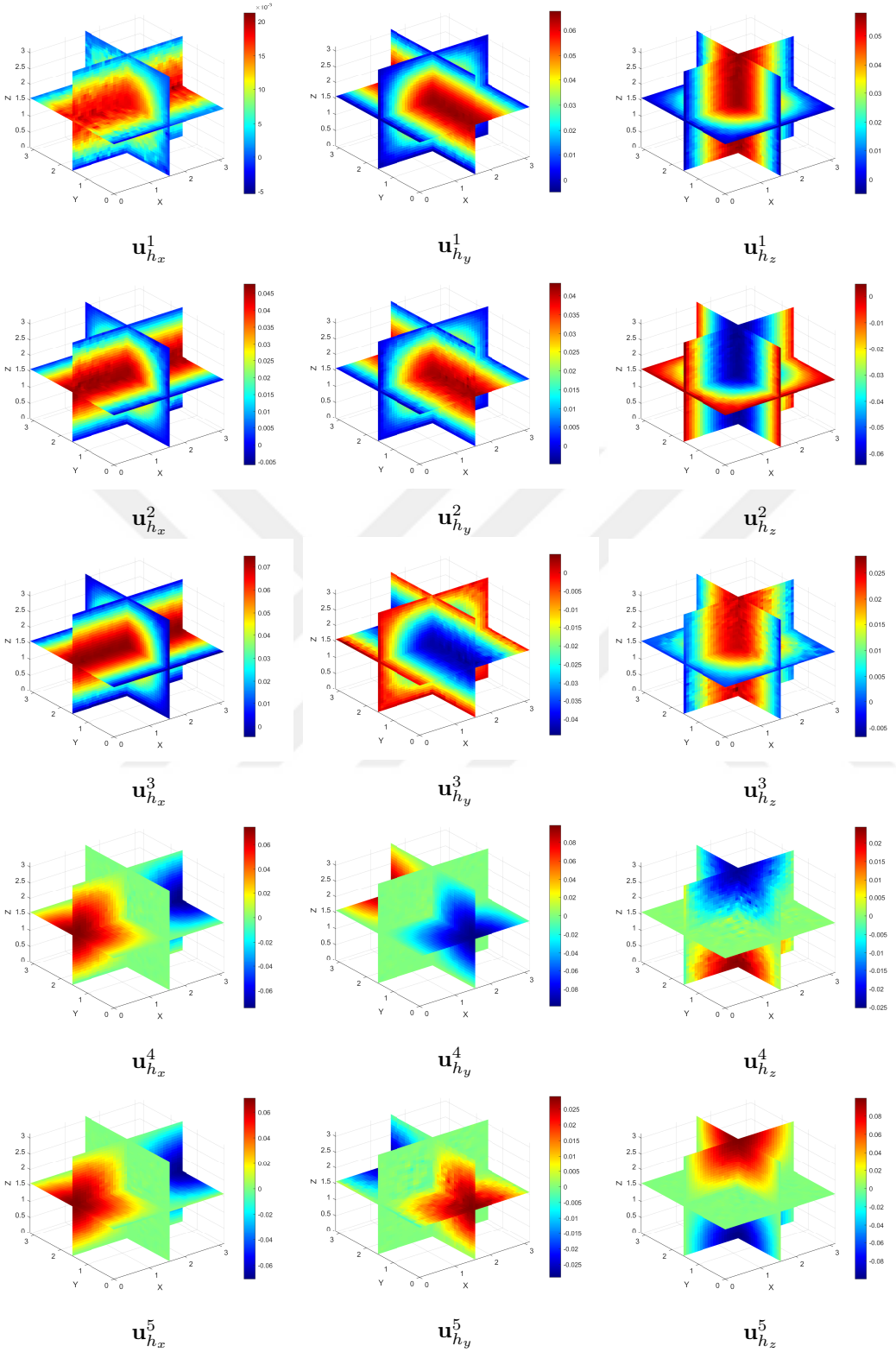
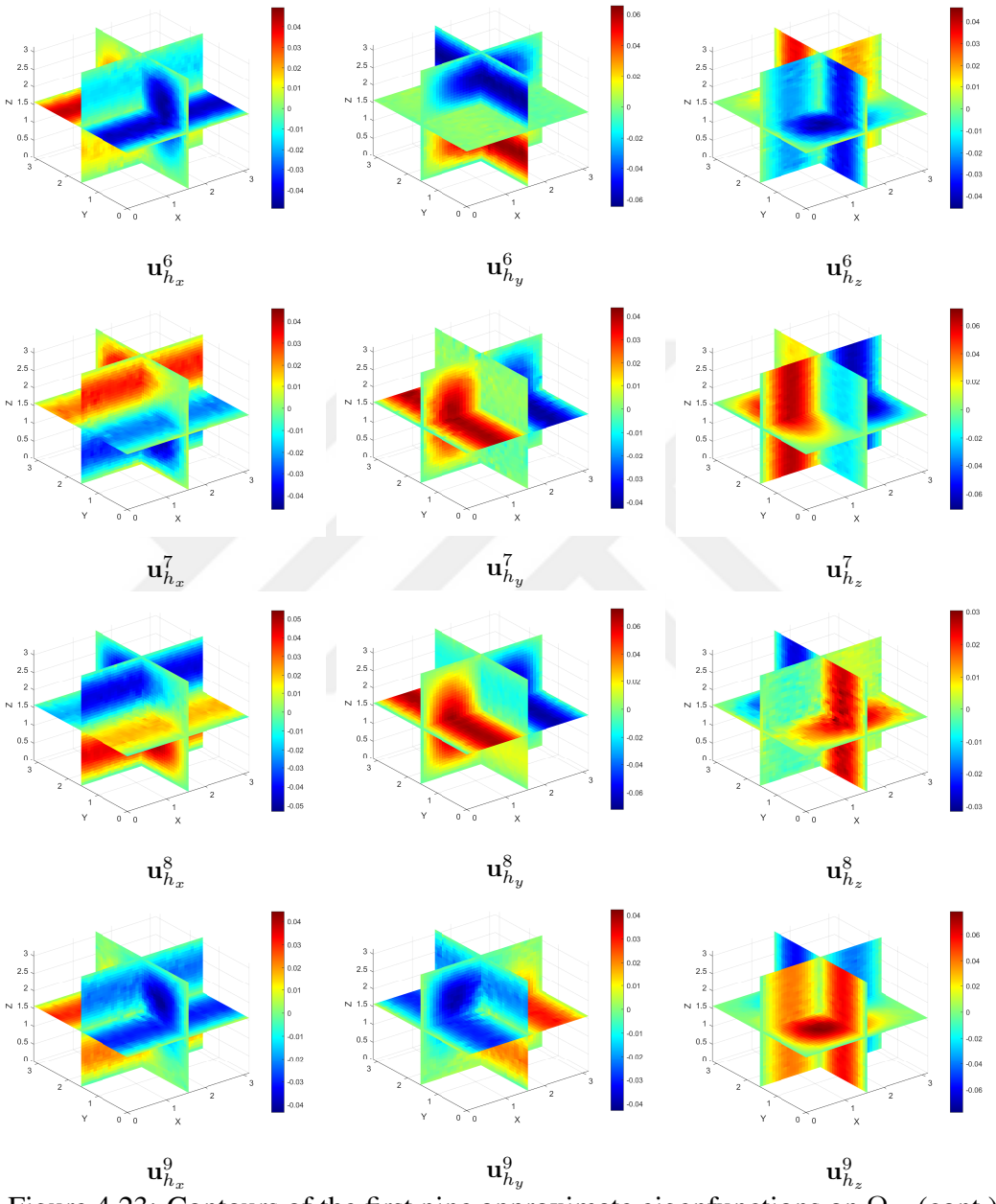


Figure 4.23: Contours of the first nine approximate eigenfunctions on Ω_6.



$\mathbf{u}_{h_x}^6$ $\mathbf{u}_{h_y}^6$ $\mathbf{u}_{h_z}^6$

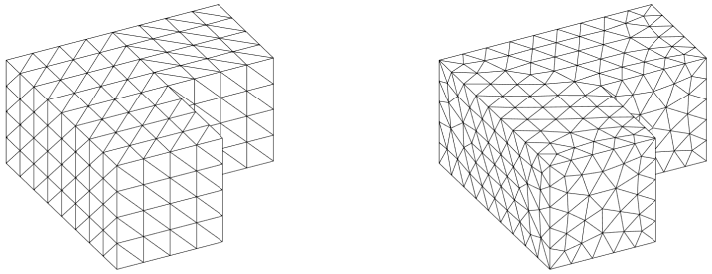
$\mathbf{u}_{h_x}^7$ $\mathbf{u}_{h_y}^7$ $\mathbf{u}_{h_z}^7$

$\mathbf{u}_{h_x}^8$ $\mathbf{u}_{h_y}^8$ $\mathbf{u}_{h_z}^8$

$\mathbf{u}_{h_x}^9$ $\mathbf{u}_{h_y}^9$ $\mathbf{u}_{h_z}^9$

Figure 4.23: Contours of the first nine approximate eigenfunctions on Ω_6. (cont.)

4.2.3.2.2 Thick L Shape The Maxwell EVP on $\Omega_6 = \Omega_2 \times [0,1]$ with $\mu_r = \epsilon_r = 1$ is approximated on the uniform and unstructured meshes, which are given in Figure 4.24.



(a) $N = 8$ (b) $h_{max} = 0.2175$

Figure 4.24: Uniform and unstructured meshes of the thick L-shape domain.

The results of the first nine approximate eigenvalues on the uniform and unstructured meshes are given in Table 4.24 and Table 4.25.

Table 4.24: The first nine reference and approximated eigenvalues on a sequence of uniform meshes with the convergence rates.

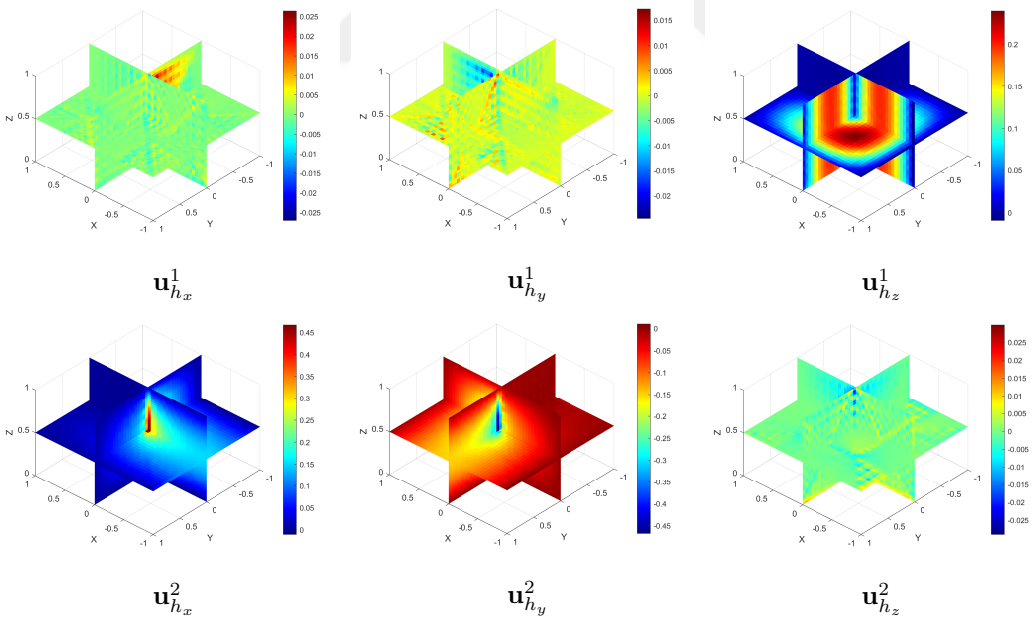
Reference	N = 2	N = 4	N = 8	N = 16	N = 32
9.6397	11.9572	10.1694(2.1)	9.7992(1.7)	9.6964(1.5)	9.6615(1.4)
11.3452	13.5661	11.1938(3.9)	11.2399(0.5)	11.3001(1.2)	11.3279(1.4)
13.4036	14.3921	13.6787(1.8)	13.4398(2.9)	13.4071(3.4)	13.4037(5.7)
15.1973	16.2610	15.3134(3.2)	15.1967(7.7)	15.1927(-3.0)	15.1954(1.3)
19.5093	17.8734	19.2597(2.7)	19.5901(1.6)	19.5540(0.9)	19.5245(1.6)
19.7392	18.0777	19.5328(3.0)	19.6999(2.4)	19.7135(0.6)	19.7310(1.6)
19.7392	18.9114	19.8908(2.4)	19.7441(5.0)	19.7308(-0.8)	19.7355(1.2)
19.7392	20.1286	20.5434(-1.0)	19.9029(2.3)	19.7684(2.5)	19.7451(2.3)
21.2591	20.7522	21.9943(-0.5)	21.3445(3.1)	21.2656(3.7)	21.2584(3.2)
zeros	3	29	291	2663	22683
DOF	26	262	2372	20200	166736

The benchmark [40] is considered to provide the reference eigenvalues. In Table 4.24, the convergence rates are not quadratic even in a sequence of uniform mesh, as expected, since the geometry contains singular corners and edges. Also, Table 4.25 presents the varying convergence rates in unstructured mesh, as usual. However, it can be observed from these numerical results that the computed eigenvalues approximate the reference ones in both meshes.

Table 4.25: The first nine reference and approximated eigenvalues on a sequence of unstructured meshes with the convergence rates.

Reference	$h_{max} = 0.7000$	$h_{max} = 0.4100$	$h_{max} = 0.2175$	$h_{max} = 0.1100$	$h_{max} = 0.0550$
9.6397	9.1280	9.7582(2.1)	9.7225(0.5)	9.6946(0.6)	9.6622(1.3)
11.3452	10.3504	10.6814(0.6)	11.1337(1.6)	11.2920(2.0)	11.3245(1.4)
13.4036	12.9617	13.0840(0.5)	13.3434(2.4)	13.3968(3.1)	13.3988(0.5)
15.1973	13.5410	14.4701(1.2)	15.0016(1.9)	15.1765(3.2)	15.1923(2.1)
19.5093	14.3975	17.8428(1.6)	19.4303(4.4)	19.5566(0.7)	19.5247(1.6)
19.7392	17.3634	18.7517(1.3)	19.5825(2.7)	19.7103(2.4)	19.7336(2.4)
19.7392	17.5969	18.8138(1.2)	19.5992(2.7)	19.7116(2.3)	19.7349(2.7)
19.7392	18.5868	19.2807(1.3)	19.6198(1.9)	19.7156(2.3)	19.7361(2.9)
21.2591	20.5063	19.8974(-0.9)	21.0768(2.9)	21.2374(3.1)	21.2541(2.1)
zeros	2	15	224	2302	21641
DOF	77	238	2182	18400	161032

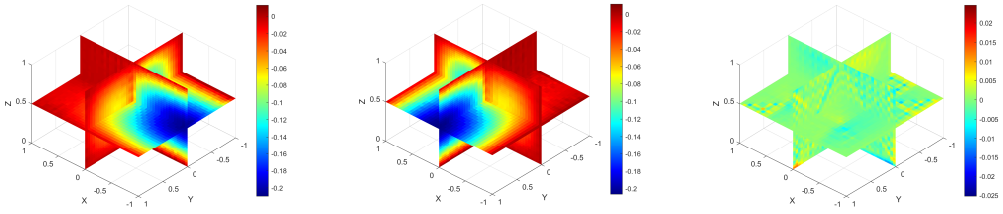
The plots of approximate eigenfunctions are given in Figure 4.25 as the contours of each component using the slices on the domain Ω_6 using the extrapolated nodal values from RBF interpolation. Here, the RBF interpolation is obtained using the results of approximation at uniform mesh with N $= 16$ (DOF $= 20200$). These approximate eigenfunctions agree with the benchmarks presented in [34].



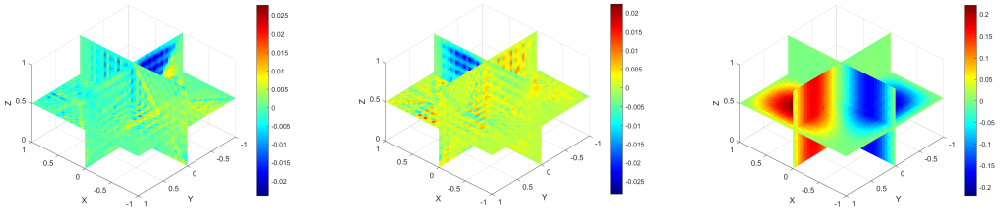
$\mathbf{u}^1_{h_x}$ $\mathbf{u}^1_{h_y}$ $\mathbf{u}^1_{h_z}$

$\mathbf{u}^2_{h_x}$ $\mathbf{u}^2_{h_y}$ $\mathbf{u}^2_{h_z}$

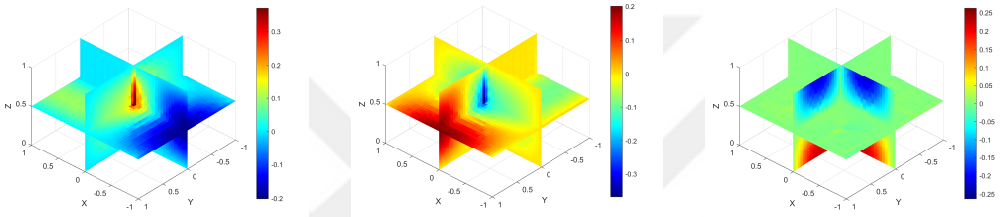
Figure 4.25: Contours of the first eight approximate eigenfunctions on Ω_7.



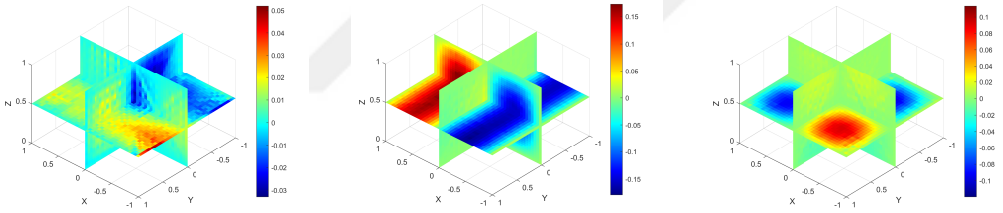
$\mathbf{u}^3_{h_x}$ $\mathbf{u}^3_{h_y}$ $\mathbf{u}^3_{h_z}$



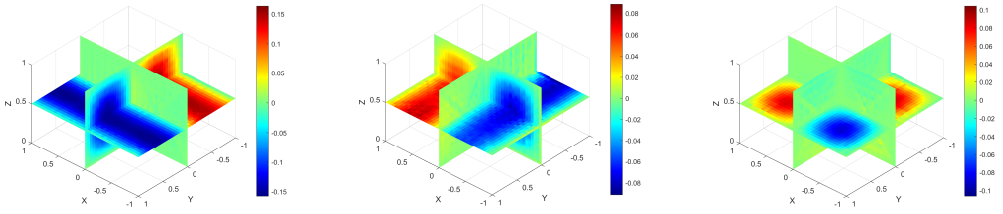
$\mathbf{u}^4_{h_x}$ $\mathbf{u}^4_{h_y}$ $\mathbf{u}^4_{h_z}$



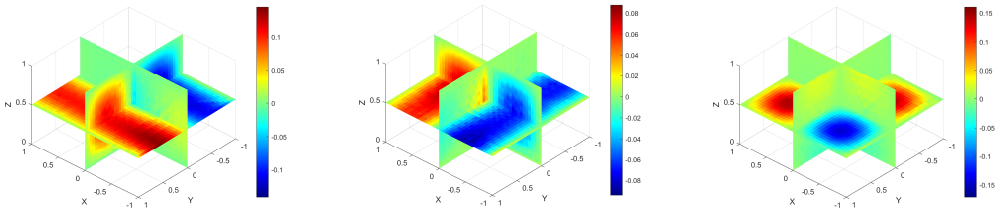
$\mathbf{u}^5_{h_x}$ $\mathbf{u}^5_{h_y}$ $\mathbf{u}^5_{h_z}$



$\mathbf{u}^6_{h_x}$ $\mathbf{u}^6_{h_y}$ $\mathbf{u}^6_{h_z}$



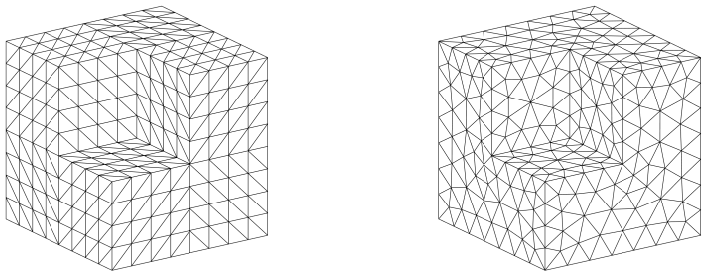
$\mathbf{u}^7_{h_x}$ $\mathbf{u}^7_{h_y}$ $\mathbf{u}^7_{h_z}$



$\mathbf{u}^8_{h_x}$ $\mathbf{u}^8_{h_y}$ $\mathbf{u}^8_{h_z}$

Figure 4.25: Contours of the first eight approximate eigenfunctions on Ω_7. (cont.)

4.2.3.2.3 Fichera Corner The Maxwell EVP on $\Omega_7 = [-1,1]^3 \setminus [-1,0]^3$ with $\mu_r = \epsilon_r = 1$ is approximated using uniform and unstructured meshes, which are shown in Figure 4.26. Also, note that all the visualizations are presented using the reversed $Z-$direction to provide a better understanding of the domain and the approximate eigenfunctions.



(a) $N = 8$ (b) $h_{max} = 0.2175$

Figure 4.26: Uniform and unstructured meshes of the fichera corner domain.

The reference eigenvalues from the benchmark [40] are considered. Note that a good accuracy could not be achieved using locally refined mesh and polynomials of degree 5 even in the benchmark. However, it is indicated that at least the first four digits are reliable for all reference eigenvalues.

Considering these reference eigenvalues and the convergence of approximate eigenvalues to them, the numerical results on a sequence of uniform and unstructured meshes are presented in Table 4.26 and Table 4.27, respectively.

Table 4.26: The first eight reference and approximated eigenvalues on a sequence of uniform meshes with the convergence rates.

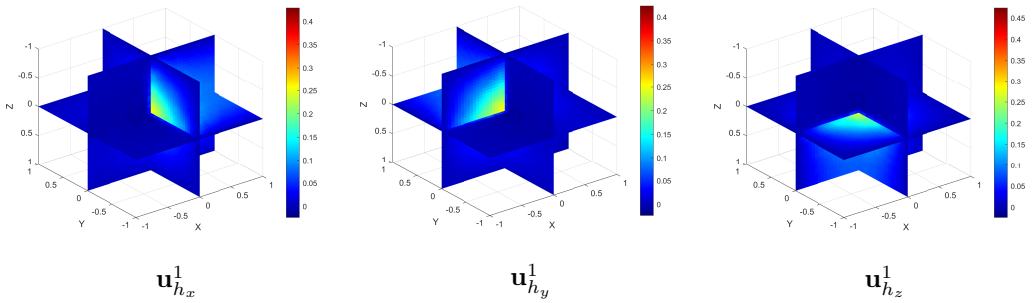
Reference	N = 2	N = 4	N = 8	N = 16	N = 32
3.2199	2.1768	2.6485(0.9)	2.9322(1.0)	3.0923(1.2)	3.1675(1.3)
5.8804	6.1011	5.5825(-0.4)	5.7406(1.1)	5.8331(1.6)	5.8659(1.7)
5.8804	7.7757	6.1040(3.1)	5.8765(5.9)	5.8650(-2.0)	5.8745(1.4)
10.6855	13.3375	8.6072(0.4)	10.2922(2.4)	10.5645(1.7)	10.6513(1.8)
10.6938	14.6571	9.7542(2.1)	10.4012(1.7)	10.6219(2.0)	10.6839(2.9)
10.6938	14.9805	9.94817(2.5)	10.5898(2.8)	10.6732(2.3)	10.6967(2.8)
12.3165	15.5559	10.2204(0.6)	11.1250(0.8)	11.8986(1.5)	12.1857(1.7)
12.3165	16.2068	10.5009(1.1)	11.7960(1.8)	12.1661(1.8)	12.2707(1.7)
zeros	0	19	279	2863	25695
DOF	19	260	2584	22832	191584

Table 4.27: The first eight reference and approximated eigenvalues on a sequence of unstructured meshes with the convergence rates.

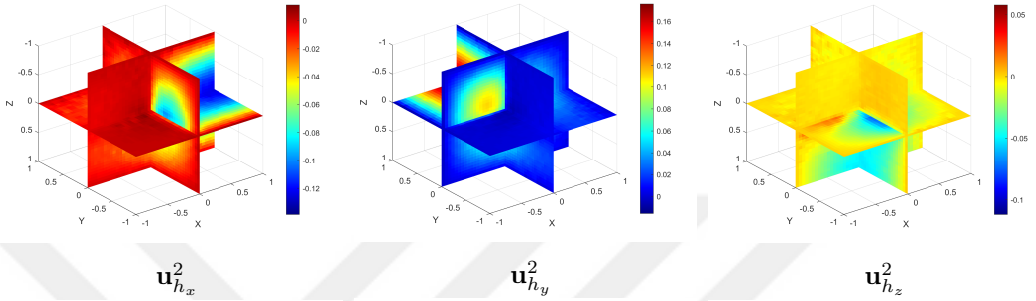
Reference	$h_{max} = 1$	$h_{max} = 0.55$	$h_{max} = 0.2700$	$h_{max} = 0.1415$	$h_{max} = 0.0700$
3.2199	1.9362	2.5970(1.2)	3.0429(1.8)	3.1491(1.4)	3.1929(1.4)
5.8804	5.5170	5.6866(1.1)	5.8508(2.6)	5.8782(4.0)	5.8803(3.7)
5.8804	5.7297	5.8050(1.2)	5.8610(1.9)	5.8790(4.0)	5.8804(7.9)
10.6855	9.7939	10.3241(1.5)	10.6662(4.1)	10.7051(0.0)	10.6962(0.9)
10.6938	10.6384	10.4949(-2.1)	10.7694(1.4)	10.7474(0.5)	10.7187(1.1)
10.6938	10.8054	10.5319(-0.6)	10.7928(0.7)	10.7504(0.9)	10.7198(1.1)
12.3165	11.0556	11.2619(0.3)	12.0720(2.1)	12.2628(2.3)	12.2977(1.5)
12.3165	11.2021	11.4382(0.4)	12.1082(2.0)	12.2677(2.2)	12.2997(1.5)
zeros	0	18	271	2635	25058
DOF	61	290	2544	20903	185705

As observed in the convergence rates of approximate eigenvalues in the thick L-shape domain, the convergence rates are not quadratic and vary in both meshes, as presented in Table 4.26 and Table 4.27. It is because both of the domains contain singular corners and edges. However, it can be observed from the results that all of the approximate eigenvalues converge to the reference ones. Additionally, the approximate eigenvalues are closer to the reference ones in the unstructured mesh.

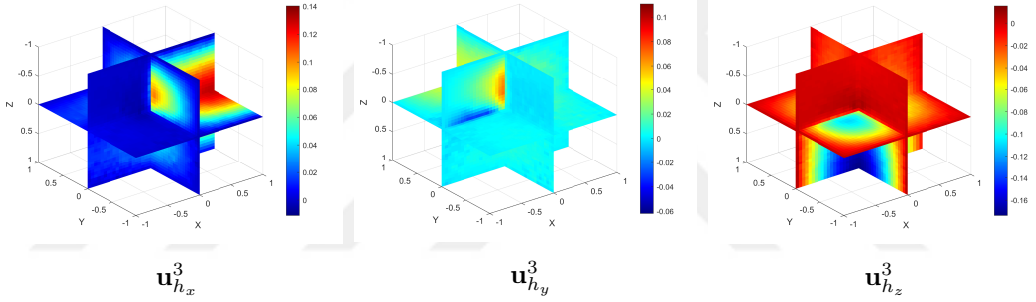
RBF interpolation is constructed using the numerical results of uniform mesh $(\mathrm{N} = 16)$ is considered to visualize the eigenfunctions. Then, using the extrapolated nodal values from the RBF interpolation, the slice contours of each component are given in Figure 4.27 on the domain Ω_7. The approximate eigenfunctions in these figures are well with the benchmarks given in [34].



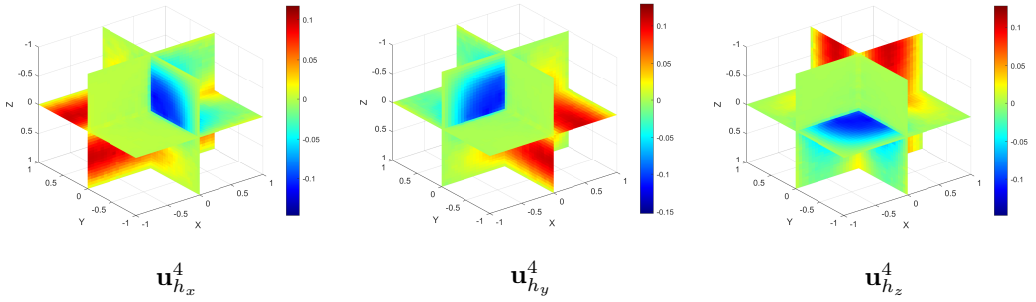
$\mathbf{u}^1_{h_x}$ $\mathbf{u}^1_{h_y}$ $\mathbf{u}^1_{h_z}$



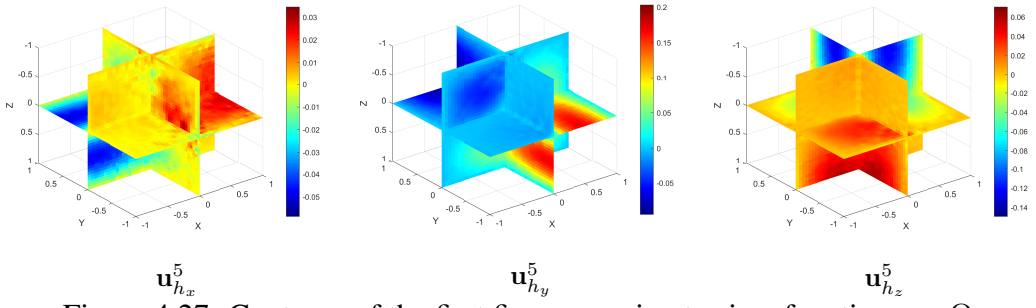
$\mathbf{u}^2_{h_x}$ $\mathbf{u}^2_{h_y}$ $\mathbf{u}^2_{h_z}$



$\mathbf{u}^3_{h_x}$ $\mathbf{u}^3_{h_y}$ $\mathbf{u}^3_{h_z}$



$\mathbf{u}^4_{h_x}$ $\mathbf{u}^4_{h_y}$ $\mathbf{u}^4_{h_z}$



$\mathbf{u}^5_{h_x}$ $\mathbf{u}^5_{h_y}$ $\mathbf{u}^5_{h_z}$

Figure 4.27: Contours of the first five approximate eigenfunctions on Ω_8.

CHAPTER 5

MODAL ANALYSIS OF THE ELECTROMAGNETIC WAVE PROPAGATION PROBLEM USING EDGE-BASED FEM

This chapter presents two methods to approximate the electric wave propagation problem introduced in Section 2.3. First, the given problem is approximated by applying the finite element method using the lowest-order Nédélec basis functions in space and finite difference in time. Then, a modal analysis approach is followed using the eigenmodes obtained from the finite element method using the lowest-order Nédélec basis functions approximation of the related eigenvalue problem that is Maxwell EVP applied to the same problem.

In this aim, the mentioned methods are discussed and presented following the study [33] that applies a modal analysis approach to describe the vibrations of an incompressible linearly elastic solid.

The outline of this chapter is constructed as follows. In the first section, the electric wave propagation problem and modal analysis at a continuous level are provided under the assumptions that the Fourier transform in time is allowed by the fields and the positive temporal frequency, as discussed in Section 2.4. The variational and finite element formulations for the introduced wave propagation problem and eigenvalue problem are presented in the second section. In the section after that, the discussed modal analysis is considered at a discrete level. Lastly, numerical results are presented in the last section of this chapter.

5.1 The electric wave propagation problem and modal analysis at continuous level

Consider the wave propagation problem for an electric field given in (2.10) with the assumption on the charge density as $\rho = 0$ for unity since the interest is on divergence-free fields in this study. Also, let the given source $-\frac{\partial \mathcal{J}_a}{\partial t}$ be denoted by $\mathbf{f}$ as $\mathbf{f} = -\frac{\partial \mathcal{J}_a}{\partial t}$. The following problem of finding electric field $\mathcal{E} : \Omega \times [0, T) \to \mathbb{R}^2$ is considered to be a boundary and initial value problem and defined on bounded, simply connected, Lipschitz, polygonal domain $\Omega \subset \mathbb{R}^{\{2,3\}}$ with boundary $\partial\Omega$, and time $t \in [0, T)$:

$$\begin{aligned}
\frac{\partial^2(\epsilon\mathcal{E})}{\partial t^2} + \frac{\partial(\sigma\mathcal{E})}{\partial t} + \nabla \times (\mu^{-1}\nabla \times \mathcal{E}) &= \mathbf{f} \qquad \text{in } \Omega,\ t \in (0, T), \\
\nabla \cdot \mathcal{E} &= 0 \qquad \text{in } \Omega,\ t \in (0, T), \\
\mathbf{n} \times \mathcal{E} &= 0 \qquad \text{on } \partial\Omega,\ t \in (0, T), \\
\mathcal{E}(\mathbf{x}, 0) &= \mathcal{E}_0 \qquad \text{in } \Omega, \\
\frac{\partial \mathcal{E}(\mathbf{x}, 0)}{\partial t} &= \dot{\mathcal{E}}_0 \qquad \text{in } \Omega,
\end{aligned} \tag{5.1}$$

where $\mathcal{E}_0$ and $\dot{\mathcal{E}}_0$ denote the given initial electric field and the given initial velocity, respectively. Also, $\mathbf{n}$ denotes the unit outward normal to the boundary $\partial\Omega$.

In this chapter, the material of domain Ω is considered as non-conducting material ($\sigma = 0$) together with the scalar permittivity ϵ and scalar permeability μ values. Also, the assumption on charge density being zero leads to divergence-free condition on the given source function that is $\nabla \cdot \mathcal{J}_a = 0$ from the relation (2.2), and Ohm's law (2.4) together with the zero conductivity $\sigma = 0$ (see, Section 3.3.1.3).

First, consider this problem with zero source function ($\mathbf{f} = \mathbf{0}$) in order to investigate the modal solution at the continuous level since it expresses the solution in terms of the modes obtained from the solution to the homogeneous problem.

Next, consider the solution $\mathcal{E}_H$ to the homogeneous problem in the form

$$\mathcal{E}_H(\mathbf{x}, t) = \sum_{m=0}^{\infty} \mathrm{e}^{-i\omega_m t}\Phi_m(\mathbf{x}). \tag{5.2}$$

If it is assumed that the modes Φ_m are linearly independent, then the amplitudes of modes Φ_m and the frequencies ω_m should be the solution of the following EVP that

is stated as

$$\begin{aligned} \nabla \times (\mu^{-1} \nabla \times \Phi_m) &= \omega_m^2 \epsilon \Phi_m \quad && \text{in } \Omega, \\ \nabla \cdot \Phi_m &= 0 && \text{in } \Omega, \\ \mathbf{n} \times \Phi_m &= 0, && \text{on } \partial\Omega, \end{aligned} \tag{5.3}$$

for $m = 1, 2, \ldots$. Equivalently, this EVP can be considered as the Maxwell EVP (see, Chapter 2) that is stated as

$$\begin{aligned} \nabla \times (\mu_r^{-1} \nabla \times \Phi_m) &= \kappa_m^2 \epsilon_r \Phi_m \quad && \text{in } \Omega, \\ \nabla \cdot \Phi_m &= 0 && \text{in } \Omega, \\ \mathbf{n} \times \Phi_m &= 0, && \text{on } \partial\Omega, \end{aligned} \tag{5.4}$$

where $\kappa_m = \omega_m \sqrt{\epsilon_0 \mu_0}$ is the wave number. The relative parameters ϵ_r, μ_r are already given as

$$\epsilon_r = \frac{1}{\epsilon_0}\Big(\epsilon + \frac{i\sigma}{\omega}\Big), \quad \mu_r = \frac{\mu}{\mu_0},$$

where the conductivity parameter is taken as $\sigma = 0$. Also, $\epsilon_0 = 8.854 \times 10^{-12}\text{Fm}^{-1}$, and $\mu_0 = 4\pi \times 10^{-7}\text{Hm}^{-1}$ are vacuum parameters.

The eigenvalues of the Maxwell EVP are all real and non-negative. If $\kappa^2 = 0$, then its corresponding eigenfunctions are associated with the infinite-dimensional eigenspace. On the other hand, for the real and positive eigenvalues $\kappa^2 \in \mathbb{R}^+$, there is a complete set of eigenvectors and corresponding eigenvalues, which can be arranged as

$$\{\Phi_1(\mathbf{x}), \ldots, \Phi_m(\mathbf{x}), \ldots\}, \qquad 0 < \kappa_1^2 \leq \cdots \leq \kappa_m^2 \leq \ldots. \tag{5.5}$$

The eigenpairs (κ_m^2, Φ_m) that are stated in (5.5) are the non-trivial solutions of (5.4) and these eigenvectors are $L^2(\Omega)$-orthogonal [13].

5.2 Finite element approximation of the wave propagation problem and the EVP

The variational formulations of the electric wave propagation problem and the EVP are considered before moving to the finite element approximations of these problems.

Firstly, consider the variational formulation of the electric wave propagation problem (5.1) that is the problem of finding $\mathcal{E} : (0, T) \to H_0(\text{curl}; \Omega)$ for all $\mathbf{v} \in H_0(\text{curl}; \Omega)$

that can be written as follows:

$$\begin{aligned}\Big(\frac{\partial^2(\epsilon\mathcal{E})}{\partial t^2},\mathbf{v}\Big)+(\mu^{-1}\nabla\times\mathcal{E},\nabla\times\mathbf{v})&=(\mathbf{f},\mathbf{v}),\ \text{for } t\in(0,T),\\ (\mathcal{E}(\mathbf{x},0),\mathbf{v})_{H_0(\text{curl};\Omega)}&=(\mathcal{E}_0,\mathbf{v})_{H_0(\text{curl};\Omega)},\\ \Big(\frac{\partial\mathcal{E}(\mathbf{x},0)}{\partial t},\mathbf{v}\Big)_{H_0(\text{curl};\Omega)}&=(\dot{\mathcal{E}}_0,\mathbf{v})_{H_0(\text{curl};\Omega)}.\end{aligned}\tag{5.6}$$

Next, consider the variational formulation of the related eigenvalue problem (5.4) that is the problem of finding non-trivial $\Phi\in H_0(\text{curl};\Omega)$ and $\kappa^2\in\mathbb{R}^+$ can be written as follows:

$$(\mu_r^{-1}\nabla\times\Phi,\nabla\times\mathbf{v})=\kappa^2(\epsilon_r\Phi,\mathbf{v}),\ \ \forall\mathbf{v}\in H_0(\text{curl};\Omega).\tag{5.7}$$

Then, finite element formulations of the wave propagation problem and the eigenvalue problem are obtained by considering the variational formulations of the related problems with the finite-dimensional subspace $V_h\subset H_0(\text{curl};\Omega)$ that is constructed using the lowest-order Nédélec basis functions introduced in Section 3.6. The finite element formulation of the electric wave propagation problem considering its variational formulation (5.6) and the finite-dimensional subspace V_h can be considered in the following as the problem of finding $\mathcal{E}_h:(0,T)\rightarrow V_h$ for all $\mathbf{v}_h\in V_h$, which is stated as

$$\Big(\frac{\partial^2(\epsilon\mathcal{E}_h)}{\partial t^2},\mathbf{v}_h\Big)+(\mu^{-1}\nabla\times\mathcal{E}_h,\nabla\times\mathbf{v}_h)=(\mathbf{f},\mathbf{v}_h),\ \text{for } t\in(0,T),\tag{5.8}$$

$$(\mathcal{E}_h(\mathbf{x},0),\mathbf{v}_h)_{H_0(\text{curl};\Omega)}=(\mathcal{E}_0,\mathbf{v}_h)_{H_0(\text{curl};\Omega)},\tag{5.9}$$

$$\Big(\frac{\partial\mathcal{E}_h(\mathbf{x},0)}{\partial t},\mathbf{v}_h\Big)_{H_0(\text{curl};\Omega)}=(\dot{\mathcal{E}}_0,\mathbf{v}_h)_{H_0(\text{curl};\Omega)}.\tag{5.10}$$

where $\mathcal{E}_h$ is the finite element approximation to $\mathcal{E}$ that is stated as

$$\mathcal{E}(\mathbf{x},t)\approx\mathcal{E}_h(\mathbf{x},t)=\sum_{s=1}^{n_e}\Upsilon_s(\mathbf{x})E_s(t),\tag{5.11}$$

where $\Upsilon_s(\vec{x})$ is the global Nédélec basis function, which is related to the edge s, $E_s(t)$ is the coefficient that controls the tangential field on edge s at time t, and n_e is the number of internal edges (degrees of freedom) when the Dirichlet boundary condition is imposed.

Moreover, the finite element formulation of the eigenvalue problem considering its variational formulation (5.7) and the finite-dimensional subspace V_h can be considered in the following as the problem of finding non-trivial $\Phi_h\in V_h$ and $\kappa^2\in\mathbb{R}^+$,

which is stated as

$$(\mu_r^{-1}\nabla \times \Phi_h, \nabla \times \mathbf{v}_h) = \kappa_h^2(\epsilon_r \Phi_h, \mathbf{v}_h), \quad \forall \mathbf{v}_h \in V_h. \tag{5.12}$$

Finally, algebraic forms of the finite element formulations of the wave propagation problem and the eigenvalue problem are considered. Let $E(t)$ be the array that contains $E_s(t),\ i = 1, 2, \ldots, n_e$ from Equation (5.11). Also, let E_0 and $\dot{E}_0$ be the initial conditions obtained from equations (5.9)-(5.10). Note that the time derivative of $E(t)$ is denoted by $\dot{E}(t)$. Then, the algebraic form of Equations (5.8)-(5.10) can be stated as

$$\epsilon_0 \mathbf{M}\ddot{E} + \mu_0^{-1}\mathbf{K}E = \mathbf{b}, \quad t \in (0, T), \tag{5.13}$$

$$E = E_0 \ \text{ at } t = 0, \tag{5.14}$$

$$\dot{E} = \dot{E}_0 \ \text{ at } t = 0, \tag{5.15}$$

where $\mathbf{K}, \mathbf{M}, \mathbf{b}$ denote the stiffness matrix that is introduced in (3.76), the mass matrix that is introduced in (3.79), and the load vector that is presented in (3.80), respectively. Note that the relative parameters ϵ_r, μ_r are included in the computations of $\mathbf{M}$ and $\mathbf{K}$, where the parameters can be expressed as $\epsilon = \epsilon_r\epsilon_0$ since $\sigma = 0$, and $\mu = \mu_r\mu_0$.

Let $\psi \in \mathbb{R}^{n_e}$ be the array that contains the coefficient that controls the tangential field on the related edge. Then, the algebraic form of Equation (5.12) can be stated as

$$\mathbf{K}\psi = \kappa_h^2 \mathbf{M}\psi. \tag{5.16}$$

If the mass matrix $\mathbf{M}$ is full rank, System (5.16) produces n_e solutions. Hence, the discrete eigenvectors and eigenvalues can be stated as

$$\{\psi_1, \ldots, \psi_{n_e}\}, \qquad 0 < \kappa_{h,1}^2 \leq \cdots \leq \kappa_{h,n_e}^2.$$

5.3 The discrete modal analysis

In this section, the solution of the electric wave propagation problem at the discrete level presented in Equations (5.13)-(5.15) in terms of the eigenpairs $(\kappa_{h,j}^2, \psi_j)$ obtained from the eigenvalue problem at the discrete level and presented in Equation

(5.16) is derived. It will be shown that the solution to Problem (5.13)-(5.15) can be expressed in the form

$$E(t) = \sum_{j=1}^{n_e} c_j(t)\psi_j, \tag{5.17}$$

with suitable scalar functions $c_j, \quad j = 1, 2, \ldots, n_e$ to be determined.

Let

$$\Psi = \begin{bmatrix} \psi_1 \ldots \psi_{n_e} \end{bmatrix} \in \mathbb{R}^{n_e}, \quad C(t) = \begin{bmatrix} c_1(t) \\ \vdots \\ c_{n_e}(t) \end{bmatrix} \in \mathbb{R}^{n_e}, \tag{5.18}$$

which follows

$$E(t) = \Psi C(t). \tag{5.19}$$

Substituting (5.19) into (5.13), and multiplying from the left by Ψ^T the following is obtained:

$$\epsilon_0 \Psi^T \mathbf{M} \Psi \ddot{C}(t) + \mu_0^{-1} \Psi^T \mathbf{K} \Psi C(t) = \Psi^T \mathbf{b}. \tag{5.20}$$

Then, the expanded form of Equation (5.20) can expressed as

$$\epsilon_0 \psi_m^T \sum_{n=1}^{n_e} \mathbf{M} \psi_n \ddot{c}_n + \mu_0^{-1} \psi_m^T \sum_{m=1}^{n_e} \mathbf{K} \psi_n c_n = \psi_m^T \mathbf{b}, \quad m = 1, \ldots, n_e. \tag{5.21}$$

Also, the $L^2(\Omega)$-orthogonality at discrete level is stated as

$$\psi_m^T \mathbf{M} \psi_n = \delta_{mn}, \quad \psi_m^T \mathbf{K} \psi_n = \kappa_{h,n}^2 \delta_{mn}, \quad m, n = 1, \ldots, n_e. \tag{5.22}$$

Thus, using (5.22) Equation (5.21) becomes

$$\epsilon_0 \ddot{c}_m + \mu_0^{-1} \kappa_{h,m}^2 c_m = \psi_m^T \mathbf{b}, \quad m = 1, \ldots, n_e. \tag{5.23}$$

Since $\kappa_{h,m}^2 = \omega_{h,m}^2 \epsilon_0 \mu_0$, Equation (5.23) is equivalently expressed as

$$\ddot{c}_m + \omega_{h,m}^2 c_m = F_m, \quad m = 1, \ldots, n_e, \tag{5.24}$$

where $F_m := \epsilon_0^{-1} \psi_m^T \mathbf{b}$.

The solution for the differential equation given in (5.24) can be stated as

$$c_m(t) = c_{m,h}(t) + c_{m,p}(t), \quad m = 1, \ldots, n_e, \tag{5.25}$$

where $c_{m,p}$ is a particular solution, and $c_{m,h}$ is the general solution for the homogeneous equation corresponding to Equation (5.24).

Then, the solution to Problem (5.13)-(5.15) is stated in the following.

$$E(t) = \sum_{m=1}^{n_e} (A_m \mathrm{e}^{i\omega_{h,m}t} + B_m \mathrm{e}^{-i\omega_{h,m}t} + c_{m,p}(t))\psi_m, \tag{5.26}$$

where $A_m, B_m,\ m = 1, \ldots, n_e$ are the coefficients to be determined using the following:

$$E(0) = \sum_{m=1}^{n_e} (A_m + B_m + c_{m,p}(0))\psi_m = \sum_{m=1}^{n_e} (\psi_m^T \mathbf{M} E_0)\psi_m, \tag{5.27}$$

$$\dot{E}(0) = \sum_{m=1}^{n_e} (i\omega_{h,m}A_m - i\omega_{h,m}B_m + \dot{c}_{m,p}(0))\psi_m = \sum_{m=1}^{n_e} (\psi_m^T \mathbf{M} \dot{E}_0)\psi_m, \tag{5.28}$$

where the right-hand-sides of (5.27) and (5.28) correspond to the initial conditions projected onto the subspace generated by the modes. Then, from these equations, the following is obtained:

$$A_m + B_m + c_{m,p}(0) = \psi_m^T \mathbf{M} E_0, \quad i\omega_{h,m}A_m - i\omega_{h,m}B_m + \dot{c}_{m,p}(0) = \psi_m^T \mathbf{M} \dot{E}_0, \tag{5.29}$$

for $m = 1, 2, \ldots, n_e$. Therefore, the solution for the electric wave propagation problem at the discrete level given in (5.13)-(5.15) can be written as described in the equation (5.17), since the solution A_m, B_m is unique where it is trivially examined.

Note that the modal analysis is considered as the approximate method where only a few modes denoted by n_m are used in the expansion (5.17). The solution is approximated using the following

$$E(t) = \sum_{j=1}^{n_e} c_j(t)\psi_j \approx E_{n_m}(t) = \sum_{j=1}^{n_m} c_j(t)\psi_j, \tag{5.30}$$

with $n_m \leq n_e$.

Moreover, consider the following norm introduced in [33], which will be useful in consideration of errors in numerical tests and is stated as:

$$||Z||_{\mathbf{A}} := (Z^T \mathbf{A} Z)^{1/2}, \tag{5.31}$$

where $\mathbf{A}$ is a $k \times k$ symmetric and positive definite or positive semi-definite matrix, and Z is an array of size k.

5.4 Numerical Results

In this section, numerical results are presented for the approximations of the inhomogeneous electric wave propagation problem (5.1) in the domain $\Omega := [0, \pi]^2$. The lowest-order Nédélec basis functions are used in the numerical experiments of the finite element approximations in space using the uniform mesh ($\mathrm{N} = 64, \mathrm{DOF} = 12160$). The second-order accurate backward difference scheme is stated as follows:

$$\ddot{E}(t_i) \approx (-E(t_{i-3}) + 4E(t_{i-2}) - 5E(t_{i-1}) + 2E(t_i))/(\Delta t)^2, \tag{5.32}$$

for $i = 3, 4, \ldots, n_T$, where, Δt is a time step and the discrete time set $t_i = i\Delta t$, is used for the approximation of the second-order time derivative.

Moreover, the modal analysis is applied to the given problems using the eigenmodes obtained from the finite element approximation of Maxwell EVP in square domain (see, Section 4.2.3.1.1).

The results of the finite element in space, the finite difference in time scheme, and the modal analysis are compared with the exact solution in the following section. Additionally, two approaches are compared in terms of CPU times and errors.

5.4.1 An Inhomogeneous Wave Propagation Problem

Consider the equations given in (5.1) with the settings:

- The material properties are $\epsilon = \epsilon_0 = 8.854 \times 10^{-12}\mathrm{Fm}^{-1}$, $\mu = \mu_0 = 4\pi \times 10^{-7}\mathrm{Hm}^{-1}$, $\sigma = 0$ (vacuum). This leads to $\epsilon_r = \mu_r = 1$.
- $\Omega = [0, \pi]^2$.
- $T = 10\pi$ nanoseconds.
- $\mathbf{f} = \cos(3 \times 10^8 t)\frac{1}{\mu_0}\begin{bmatrix} -2\cos(x_2) + x_2\sin(x_2)(1 - \epsilon_0\mu_0 9 \times 10^{16}) \\ -2\cos(x_1) + x_1\sin(x_1)(1 - \epsilon_0\mu_0 9 \times 10^{16}) \end{bmatrix}$.
- $\mathcal{E}_0 = \begin{bmatrix} x_2\sin(x_2) \\ x_1\sin(x_1) \end{bmatrix}, \dot{\mathcal{E}}_0 = \begin{bmatrix} 0 \\ 0 \end{bmatrix}$.

The exact solution for this problem is given as

$$\mathcal{E}_{\text{exact}} = \cos(3 \times 10^8 t) \begin{bmatrix} x_2 \sin(x_2) \\ x_1 \sin(x_1) \end{bmatrix}. \tag{5.33}$$

Now, consider the finite element formulation for this inhomogeneous wave propagation problem given in (5.8)-(5.10) with the settings that are introduced above.

$$\left(\frac{\partial^2 \epsilon_0 \mathcal{E}_h}{\partial t^2}, \mathbf{v}_h\right) + (\mu_0^{-1} \nabla \times \mathcal{E}_h, \nabla \times \mathbf{v}_h) = (\mathbf{f}, \mathbf{v}_h), \quad t \in (0, 10\pi), \tag{5.34}$$

$$(\mathcal{E}_h(\mathbf{x}, 0), \mathbf{v}_h)_{H(\text{curl};\Omega)} = (\mathcal{E}_0, \mathbf{v}_h)_{H(\text{curl};\Omega)}, \tag{5.35}$$

$$\left(\frac{\partial \mathcal{E}_h(\mathbf{x}, 0)}{\partial t}, \mathbf{v}_h\right)_{H(\text{curl};\Omega)} = (\dot{\mathcal{E}}_0, \mathbf{v}_h)_{H(\text{curl};\Omega)} \tag{5.36}$$

Next, considering the algebraic version introduced in (5.13) - (5.15), Problem (5.34)-(5.36) in an algebraic form is stated in the following as a problem of finding the array $E(t)$ containing the coefficients that control the tangential field on the related edge at time t.

$$\epsilon_0 \mathbf{M} \ddot{E} + \mu_0^{-1} \mathbf{K} E = \mathbf{b}, \quad t \in (0, 10\pi), \tag{5.37}$$

$$E = E_0 \ \text{ at } t = 0, \tag{5.38}$$

$$\dot{E} = \dot{E}_0 \ \text{ at } t = 0. \tag{5.39}$$

Note that, here E_0 and $\dot{E}_0$ corresponds to the projections of the given initial conditions that are obtained from the Equations (5.35) and (5.36).

The finite element in space finite-difference in time scheme is stated in the following using the finite-difference approximation of the second time derivative given in (5.32):

$$\left(\frac{2C}{(\Delta t)^2}\mathbf{M} + \mathbf{K}\right) E_i = \left(\frac{C}{(\Delta t)^2}\right) \mathbf{M}(E_{i-3} - 4E_{i-2} + 5E_{i-1}) + \mu_0 \mathbf{b}_i, \tag{5.40}$$

where $C = \epsilon_0 \mu_0$, $i = 3, \ldots, (10\pi/(\Delta t))$ and $E_i, \ i = 0, 1, 2$ are obtained from the given initial conditions. Following the setting presented in (5.40), the finite element in space and finite-difference in time approximation results are obtained. Also, the projection of the spatial part of the exact solution given in (5.33) and denoted by $\mathcal{P}^{\mathcal{E}_{\text{exact}}}$ onto $H(\text{curl};\Omega)$ space is obtained by

$$(\mathcal{P}^{\mathcal{E}_{\text{exact}}}, \mathbf{v}_h)_{H(\text{curl};\Omega)} = ((x_2 \sin(x_2), x_1 \sin(x_1))^T, \mathbf{v}_h)_{H(\text{curl};\Omega)} \ \ \forall \mathbf{v}_h \in V_h. \tag{5.41}$$

Then, the projection at a discrete time t_i is obtained by

$$\mathcal{P}_i^{\mathcal{E}_{\text{exact}}} = \cos(3 \times 10^8 t_i)\mathcal{P}^{\mathcal{E}_{\text{exact}}}, \quad i = 0, 1, 2, \ldots, (10\pi/(\Delta t)). \tag{5.42}$$

Next, the coefficients that correspond to the same edge from the FEM in space FD in time approximation denoted by E_i and the projection of exact solution $\mathcal{P}_i^{\mathcal{E}_{\text{exact}}}$ are compared over the discrete time $t_i,\ i = 0, 1, 2, \ldots, (10\pi/(\Delta t))$. The edge is chosen to be the one closest to the point $(\pi/2, \pi/2)$ since the largest fluctuations occur at this point. The comparison is presented in Figure 5.1, and it is observed that the method is accurate for both Δt (ns) values since the provided FD scheme is unconditionally stable. However, the decreasing value of the time step does not lead to better approximations for this case. This can be achieved with much smaller values of Δt, increasing the computational time enormously.

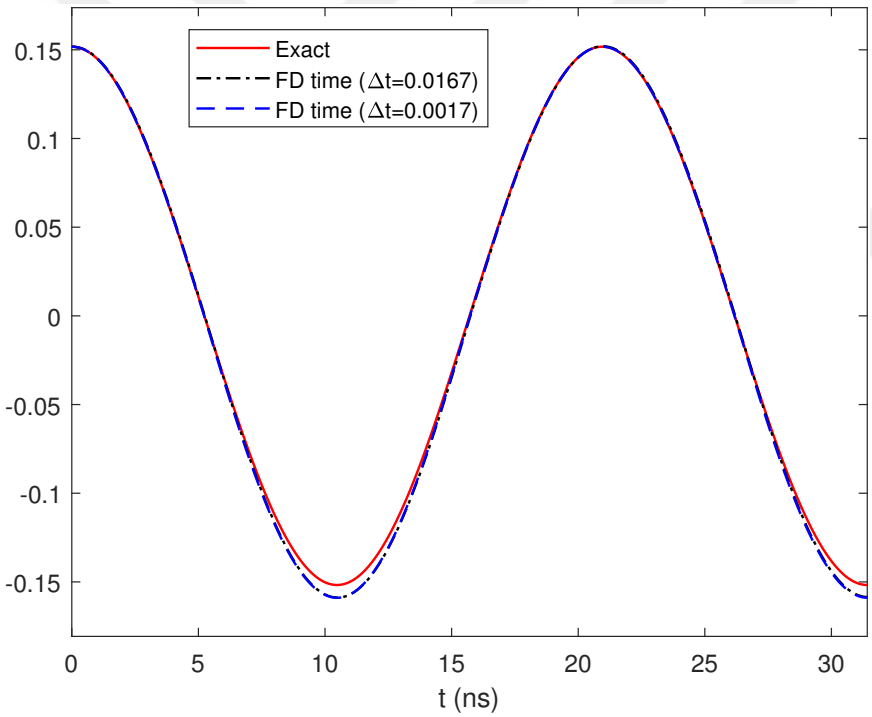


Figure 5.1: Coefficients that control the tangential field on the selected edge.

Then, consider the approximation of the algebraic form of the inhomogeneous wave propagation problem stated in (5.37)-(5.39) using the eigenmodes obtained by the solution of the eigenvalue problem (5.16) that are given in Section 4.2.3.1 with the expansion presented in (5.17). Following Section 5.3 and considering the case for this numerical experiment, the coefficients $c_m,\ m = 1, 2, \ldots, n_e$, are determined from the

equation

$$\ddot{c}_m(t) + \omega_{h,m}^2 c_m(t) = \psi_m^T(\epsilon_0^{-1}\cos(3\times 10^8 t)P^f), \quad m = 1, 2, \ldots, n_e, \tag{5.43}$$

where P^f is the projection of the spatial part of the given source function $\mathbf{f}$ that is results of

$$(P^f, \mathbf{v}_h)_{H(\text{curl};\Omega)} = (\mathbf{f}, \mathbf{v}_h)_{H(\text{curl};\Omega)}, \quad \forall \mathbf{v}_h \in V_h. \tag{5.44}$$

If the equation (5.43) is considered with the solution of the form $c_m(t) = \psi_m^T y_m(t),\ m = 1, 2, \ldots, n_e$, then the problem of finding $y_m(t)$ is derived as

$$y_m'' + \omega_{h,m}^2 y_m = \epsilon_0^{-1}\cos(3\times 10^8 t)P^f. \tag{5.45}$$

Solution to Problem (5.45) can be stated as

$$\begin{aligned} y_m &= y_{h,m} + y_{p,m}, \\ y_m &= A_m\cos(\omega_{h,m}t) + B_m\sin(\omega_{h,m}t) + y_{p,m}, \end{aligned} \tag{5.46}$$

where $y_{h,m} = A_m\cos(\omega_{h,m}t) + B_m\sin(\omega_{h,m}t)$ is the general solution of homogeneous problem, and $y_{p,m}$ is the particular solution.

Then, the equation to obtain the particular solution to Problem (5.45) is given as follows:

$$y_{p,m}'' + \omega_{h,m}^2 y_{p,m} = \epsilon_0^{-1}\cos(3\times 10^8 t)P^f. \tag{5.47}$$

The particular solution is obtained by considering the two cases, where $\omega_{h,m} = 3\times 10^8$, and $\omega_{h,m} \neq 3\times 10^8$.

If $\omega_{h,m} = 3\times 10^8$, then the particular solution and its second derivative can be stated as

$$\begin{aligned} y_{p,m} &= t(C_m\cos(3\times 10^8 t) + D_m\sin(3\times 10^8 t)), \\ y_{p,m}'' &= (-6\times 10^8 C_m - 9\times 10^{16} t D_m)\sin(3\times 10^8 t) \\ &\quad + (6\times 10^8 D_m - 9\times 10^{16} t C_m)\cos(3\times 10^8 t). \end{aligned} \tag{5.48}$$

Substituting (5.48) into (5.47) yields:

$$-6\times 10^8 C_m\sin(3\times 10^8 t) + 6\times 10^8 D_m\cos(3\times 10^8 t) = \epsilon_0^{-1}\cos(3\times 10^8 t)P^f, \tag{5.49}$$

where Equation (5.49) leads to $C_m = 0$, and $D_m = \frac{P^f}{\epsilon_0 6\times 10^8}$.

So, the particular solution is given by

$$y_{p,m} = \frac{P^f}{\epsilon_0 6\times 10^8} t\sin(3\times 10^8 t), \quad \text{when} \quad \omega_{h,m} = 3\times 10^8.$$

Next, the unknown coefficients A_m and B_m of the solution to the homogeneous problem determined from the equations

$$\begin{aligned} y_m &= A_m \cos(3\times 10^8 t) + B_m \sin(3\times 10^8 t) + t\sin(3\times 10^8 t)\frac{P^f}{\epsilon_0 6\times 10^8}, \\ y_m' &= -3\times 10^8 A_m \sin(3\times 10^8 t) + 3\times 10^8 B_m \cos(3\times 10^8 t) \\ &\quad + (\sin 3\times 10^8 t) + t\cos(3\times 10^8 t))\frac{P^f}{\epsilon_0 6\times 10^8}. \end{aligned} \tag{5.50}$$

Using the relations given in (5.29), it is obtained that

$$A_m = \mathbf{M}E_0, \quad B_m = 0.$$

Hence, the solution $c_m(t)$ to Problem (5.43) is presented as

$$c_m = \psi_m^T((\mathbf{M}E_0)\cos(3\times 10^8 t) + \frac{P^f}{\epsilon_0 6\times 10^8} t\sin(3\times 10^8 t)), \text{ for } \omega_{h,m} = 3\times 10^8. \tag{5.51}$$

If $\omega_{h,m} \neq 3\times 10^8$, then the particular solution for the second case can be stated as

$$y_{p,m} = C_m \cos(3\times 10^8 t) + D_m \sin(3\times 10^8 t). \tag{5.52}$$

Following the same steps performed for the first case, the solution $c_m(t)$ to Problem (5.43) is presented as

$$\begin{aligned} c_m = \psi_m^T((\mathbf{M}E_0 + \frac{P^f}{\epsilon_0(9\times 10^{16} - \omega_{h,m}^2)})\cos(\omega_{h,m} t) \\ - \frac{P^f}{\epsilon_0(9\times 10^{16} - \omega_{h,m}^2)}\cos(3\times 10^8 t), \end{aligned} \tag{5.53}$$

when $\omega_{h,m} \neq 3\times 10^8$.

The approximation to the considered inhomogeneous wave propagation problem using the eigenmodes from (5.16) and $c_m(t)$ from (5.51) and (5.53) is obtained as

$$E(t) = \sum_{j=1}^{n_e} c_j(t)\psi_j. \tag{5.54}$$

Now, truncating the solution with the number of modes denoted by n_m, it can be written that

$$E(t) = \sum_{j=1}^{n_e} c_j(t)\psi_j \approx E_{n_m}(t) = \sum_{j=1}^{n_m} c_j(t)\psi_j, \tag{5.55}$$

where $E_{n_m}(t)$ denote the truncation solution so that $n_m \leq n_e$.

The results obtained by the truncated modal solutions are compared with the projection of the exact solution. In this way, to investigate the effect of adding the next mode to the modal expansion, the error $||\mathcal{P}^{\mathcal{E}_{\text{exact}}} - E_{m_n}||_{\mathbf{M}}$ normalized by $||\mathcal{P}^{\mathcal{E}_{\text{exact}}}||_{\mathbf{K}}$ is examined with the corresponding eigenvalues ω^2_{h,n_m+1} for $n_m \leq 300$ at a fixed time $t^* \approx 20.94$ in Figure 5.2. The fixed time t^* is chosen to be $20.94 \approx 6.67\pi$ where the coefficients arrive at a local maximum, which can be seen Figure 5.3. However, results are alike at all time levels, which are not included for brevity.

As can be seen in Figure 5.2, the error decreases between the approximation using the truncated modal solution and the exact solution when more modes are included in the expansion. However, adding more modes to the expansion has relatively small effect on decreasing the error after using the first 12 modes. Also, there is a sufficient decrease in the error between the truncated modal solution using 4 modes.

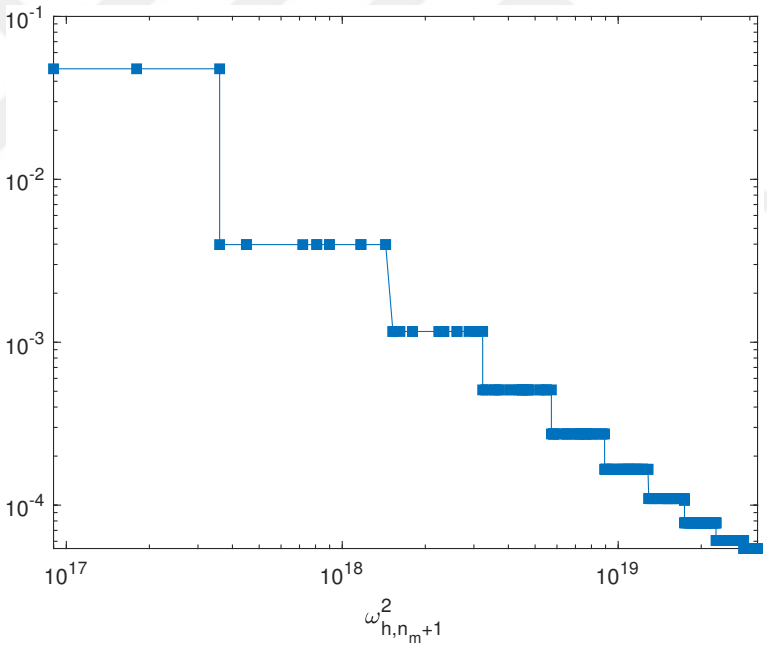


Figure 5.2: Variation of the error at fixed time t^*.

Therefore, the coefficients corresponding to the fixed edge obtained by truncated modal solutions using 12 modes and 300 modes are compared with the projected exact solution over the time $t \in [0, 10\pi]$ (ns) in Figure 5.3. Both truncated modal solutions are close to the exact solution, as expected from Figure 5.2. Also, Figure 5.3 validates the relatively poor effects of the modes after 12-th mode.

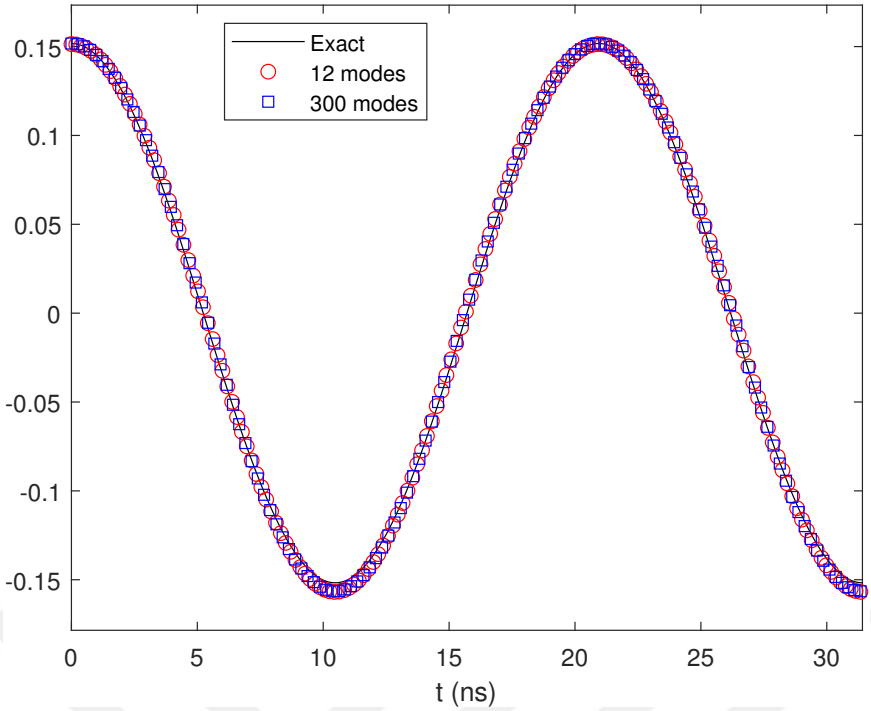


Figure 5.3: Coefficients that control the tangential field on the selected edge.

The approximations of two approaches that are based on the FEM model of the wave propagation problem are shown to be accurate. Next, the comparison between these two methodologies is performed in terms of computational time and error. The approximate solution resulted from the FEM in space/FD in time scheme when $\Delta t = 0.0167$ (ns) is considered for the comparison. On the other hand, the truncated modal expansion is considered with the first 12 modes. The CPU times are calculated by the average of ten runs for both methods. Also, for each case, the normalized error between the approximate solution and the exact solution is calculated using the following:

$$\text{Error} := \frac{(\int_0^T (\mathbf{u} - \mathbf{u}_h)^2 dt)^{1/2}}{(\int_0^T \mathbf{u}^2 dt)^{1/2}},$$

where $\mathbf{u}$ is the exact solution, and $\mathbf{u}_h$ is the one of the approximate solutions.

The CPU times and the errors are presented in Table 5.1, where it can be seen that the modal solution outperforms the FD scheme with a considerable time difference. Additionally, the error is smaller between the modal approximation and the exact solution when compared with the error of the approximation obtained by FD in time.

Table 5.1: Comparison between the two approaches in terms of CPU times and Errors.

Methods	CPU Time	Error
FD in time ($\Delta t = 0.0167$)	41.1831	0.0262
Modal (12 modes)	6.9423	0.0219

In this chapter, the wave propagation problem for an electric field is approximated using two methods. Both methods are conducted based on the FEM model of the wave propagation problem. Firstly, the second-order temporal derivative in the FEM model is approximated using an unconditionally stable backward-difference scheme. Next, the modal analysis is applied considering the FEM model, showing that the FEM model's solution can be expressed as an expansion employing approximate eigenmodes obtained from associated Maxwell EVP. For the validation of approaches, an inhomogeneous wave propagation problem is presented with its corresponding exact solution. Comparisons between the two approximation techniques and the exact solution are performed. It is shown that both approaches produce accurate results. Also, the comparison is performed between the two methods, where it is shown that the modal expansion outperforms the direct time domain approach.

CHAPTER 6

CONCLUSION

In this thesis, edge-based FEM approximations of Maxwell's equations are studied in three formulations: the source problem, the EVP, and the electromagnetic wave propagation problem. The source and eigenvalue problems are obtained from Maxwell's equations in consideration of time-harmonic behavior. The electromagnetic wave propagation problem is derived directly from Maxwell's equations in the time domain. The numerical approximations of the three forms are conducted by applying edge-based FEM using the lowest-order Nédélec basis functions due to their conformity with the physical properties of the Maxwell system. The electromagnetic wave propagation problem is approximated by employing two approaches that are the edge-based FEM in space/finite difference in time and a modal analysis.

The study on the Maxwell source problem contains the derivation of variational and finite element formulations using the related spaces $H(\text{curl};\Omega)$ and its finite-dimensional subspace constructed by the lowest-order Nédélec basis functions. The convergence analysis of FEM approximation is presented where the approximation converges uniformly in L^2-norm. A numerical test is performed on a two-dimensional domain with the exact solution using uniform, criss-cross, and unstructured meshes. The numerical results approve the presented theory where the approximate solution uniformly converges to the exact solution in all introduced meshes and in L^2-norm, $H(\text{curl})$-norm, and $H(\text{curl})$-seminorm.

The variational and finite element formulations of Maxwell EVP are derived using the $H(\text{curl};\Omega)$ and its finite-dimensional subspace constructed by the lowest-order Nédélec basis functions. The convergence analysis of the FEM approximation of

Maxwell EVP is presented by following the spectral theory with the corresponding source problem. Numerical tests that validate the theory are performed in two- and three-dimensional domains. The convergence rates of approximate eigenvalues to the exact or reference eigenvalues have been examined. The quadratic convergence rates are observed on the uniform meshes of convex polygons/polyhedra. Moreover, the convergence of approximate eigenvalues is presented on the unstructured meshes of convex polygons/polyhedra and on the domains that contain singularity with varying convergence rates. On the other hand, a solution of FEM utilizing the first-order Lagrange basis functions on Powell-Sabin triangulations for Maxwell EVP in 2D is considered. A comparison is conducted on the Powell-Sabin triangulation of the cracked square domain between the FEM approximations of Maxwell EVP using the Nédélec elements and the admissible nodal elements. The numerical results of both approaches put forward that the FEM using Nédélec elements provides more accurate approximations on the same mesh; however, more degrees of freedom are involved. The latter issue leads to larger matrices in the generalized eigenvalue problem to be solved, and importantly, a larger number of zeros is introduced in the edge-based solution in comparison with the nodal solution.

Finally, two approximations of the electromagnetic wave propagation problem are demonstrated, following the approximation strategies in a recent study that simulate the vibrations of incompressible elastic solids. The edge-based FEM in space-FD in time and modal analysis are employed to approximate the wave propagation problem for an electric field derived from Maxwell's equations in the time domain. It is shown that a solution to the FEM model can be represented as an expansion utilizing the eigenmodes obtained from the Maxwell EVP. The approximations of the electric wave propagation problem are obtained by the truncation of the provided modal expansion and by the direct time approach, where the second-order time derivative is approximated using the second-order accurate backward difference scheme in the FEM model. For the validation of the two numerical approaches, the wave propagation problem for an electric field is provided with the exact solution. The outcomes of the numerical tests demonstrate that both methods yield accurate results and that when additional modes are introduced to the modal expansion, the error between the exact and truncated solutions reduces. However, it is important to emphasize

that adding more modes to the expansion increases the computational cost and does not sufficiently decrease the error with a given tolerance after a certain mode in the considered configuration. Lastly, the CPU times and errors of the two methods are compared, where the results indicate that the modal expansion outperforms the direct time domain approach.

REFERENCES

[1] M. S. Alnæs, J. Blechta, J. Hake, A. Johansson, B. Kehlet, A. Logg, C. Richardson, J. Ring, M. E. Rognes, and G. N. Wells, The FEniCS project version 1.5, Archive of Numerical Software, 3(100), pp. 9–23, 2015.

[2] A. Alvarez Laguna, A. Lani, H. Deconinck, N. Mansour, and S. Poedts, A fully-implicit finite-volume method for multi-fluid reactive and collisional magnetized plasmas on unstructured meshes, Journal of Computational Physics, 318, pp. 252–276, 2016.

[3] A. Alvarez Laguna, N. Ozak, A. Lani, H. Deconinck, and S. Poedts, Fully-implicit finite volume method for the ideal two-fluid plasma model, Computer Physics Communications, 231, pp. 31–44, 2018.

[4] L. Andrade-Fonseca and H. E. Hernandez-Figueroa, Full-wave interior penalty discontinuous Galerkin method for waveguide analysis, Journal of Lightwave Technology, 36(22), pp. 5168–5176, 2018.

[5] A. Anees and L. Angermann, Time domain finite element method for Maxwell's equations, IEEE Access, 7, pp. 63852–63867, 2019.

[6] I. Anjam and J. Valdman., Fast MATLAB assembly of FEM matrices in 2D and 3D: Edge elements, Applied Mathematics and Computation, 267, pp. 252–263, 2015.

[7] I. Babuska and J. Osborn, Eigenvalue problems, in H. of Numerical Analysis volume II., editor, *P.G. Ciarlet, and J.L. Lions*, pp. 641–787.

[8] S. Badia and R. Codina, A nodal-based finite element approximation of the Maxwell problem suitable for singular solutions, SIAM Journal on Numerical Analysis, 50(2), pp. 398–417, 2012.

[9] G. R. Barrenechea, L. Boulton, and N. Boussaid, Eigenvalue enclosures and applications to the Maxwell operator, `https://arxiv.org/abs/1306.5354`, 2013.

[10] M. Benbouzid, G. Reyne, S. Derou, and A. Foggia, Finite element modeling of a synchronous machine: electromagnetic forces and mode shapes, IEEE Transactions on Magnetics, 29(2), pp. 2014–2018, 1993.

[11] S. Benhassine, L. Pichon, and W. Tabbara, An efficient finite-element time-domain method for the analysis of the coupling between wave and shielded enclosure, IEEE Transactions on Magnetics, 38(2), pp. 709–712, 2002.

[12] D. Boffi, Fortin operator and discrete compactness for edge elements, Numerische Mathematik, 87, pp. 229–246, 2000.

[13] D. Boffi, Finite element approximation of eigenvalue problems, Acta Numerica, 19, pp. 1–120, 2010.

[14] D. Boffi, M. Farina, and L. Gastaldi., On the approximation of Maxwell's eigenproblem in general 2D domains, Computers and Structures, 79, pp. 1089–1096, 2001.

[15] D. Boffi, P. Fernandes, L. Gastaldi, and I. Perugia., Computational models of electromagnetic resonators: Analysis of edge element approximation, Journal on Numerical Analysis, 36(4), pp. 1264–1290, 1999.

[16] D. Boffi and L. Gastaldi., Edge finite element for the approximation of Maxwell resolvent operator, Mathematical Modelling and Numerical Analysis, 36(2), pp. 293–305, 2002.

[17] D. Boffi and L. Gastaldi, Adaptive finite element method for the Maxwell eigenvalue problem, SIAM Journal on Numerical Analysis, 57(1), pp. 478–494, 2019.

[18] D. Boffi, L. Gastaldi, R. Rodríguez, and I. Šebestová., A posteriori error estimates for Maxwell's eigenvalue problem, Journal of Scientific Computing, 78, pp. 1250–1271, 2019.

[19] D. Boffi, J. Guzmán, and M. Neilan, Convergence of Lagrange finite elements for the Maxwell eigenvalue problem in two dimensions, IMA Journal of Numerical Analysis, pp. 1–29, 2022.

[20] D. Boffi, F. Kukichi, and J. Schoberl., Edge element computation of Maxwell's eigenvalues on general quadrilateral meshes, Mathematical Models and Methods in Applied Sciences, 16(2), pp. 265–273, 2006.

[21] A. Bonito and J.-L. Guermond., Approximation of the eigenvalue problem for the time harmonic Maxwell system by continuous Lagrange elements, Mathematics of Computation, 80(276), pp. 1887–1910, 2011.

[22] A. Bonito and J.-L. Guermond, Approximation of the eigenvalue problem for the time harmonic Maxwell system by continuous Lagrange finite elements, Math. Comput., 80, pp. 1887–1910, 10 2011.

[23] A. Bossavit, Solving Maxwell equations in a closed cavity, and the question of 'spurious modes', IEEE Transactions on Magnetics, 26(2), pp. 702–705, 1990.

[24] F. Brezzi and M. Fortin, *Mixed and hybrid finite element methods*, Springer Series in Computational Mathematics, New York, 15 edition, 1991.

[25] A. Buffa, M. Costabel, and D. Sheen, On traces for $H(\mathrm{curl}, \Omega)$ in Lipschitz domains, Journal of Mathematical Analysis and Applications, 276, pp. 845–867, 2002.

[26] A. Buffa, P. Houston, and I. Perugia, Discontinuous Galerkin computation of the Maxwell eigenvalues on simplicial meshes, Journal of Computational and Applied Mathematics, 204, pp. 317–333, 2007.

[27] A. Buffa, P. C. Jr., and E. Jamelot., Solving electromagnetic eigenvalue problems in polyhedral domains with nodal finite elements, Numerische Mathematik, 113, pp. 497–518, 2009.

[28] A. Buffa and I. Perugia., Discontinous Galerkin approximation of the Maxwell eigenproblem, SIAM Journal on Numerical Analysis, 44(5), pp. 2198–2226, 2006.

[29] A. Buffa, I. Perugia, and T. Warburton., The mortar-discontinuous Galerkin method for the 2D Maxwell eigenproblem, Journal of Scientific Computing, 40(0), pp. 86–114, 2009.

[30] S. Caorsi, P. Fernandes, and M. Raffetto, On the convergence of Galerkin finite element approximations of electromagnetic eigenproblems, SIAM Journal on Numerical Analysis, 38(2), pp. 580–607, 2001.

[31] J. R. Cardoso, *Electromagnetics Through the Finite Element Method: A Simplified Approach Using Maxwell's Equations*, 2016, ISBN 9781315366777.

[32] L. E. Castillo, I. G. Revuelto, F. S. Adana, and M. S. Palma, A finite element method for the analysis of radiation and scattering of electromagnetic waves on complex environments, Computer Methods in Applied Mechanics and Engineering, 194, pp. 637–655, 2005.

[33] R. Codina and Ö. Türk, Modal analysis of elastic vibrations of incompressible materials using a pressure-stabilized finite element method, Finite Elements in Analysis and Design, 206, 2022.

[34] G. Cohen and M. Durufle, Benchmark computations for Maxwell equations for the approximation of highly singular solutions, results from inria rocquencourt, computed with montjoie, `https://www.math.u-bordeaux.fr/~durufle/eigenvalue.php#1`, [Online; last accessed 22-December-2022].

[35] D. Colton and R. Kress, *Integral Equation Methods in Scattering Theory*, Wiley, New York, 1983.

[36] M. Costabel and M. Dauge, Singularities of electromagnetic fields in polyhedral domains, Archive for Rational Mechanics and Analysis, 151, pp. 221–276, 2000.

[37] M. Costabel and M. Dauge., Weighted regularization of Maxwell equations in polyhedral domains, Numerische Mathematik, 93, pp. 239–277, 2002.

[38] M. Costabel and M. Dauge, *Computation of resonance frequencies for Maxwell equations in non-smooth domains*, pp. 125–161, Springer Berlin Heidelberg, 2003, ISBN 978-3-642-55483-4.

[39] Q. I. Dai, W. C. Chew, Y. H. Lo, Y. G. Liu, and L. J. Jiang, Generalized modal expansion of electromagnetic field in 2D bounded and unbounded media, IEEE Antennas and Wireless Propagation Letters, 11, pp. 1052–1055, 2012.

[40] M. Dauge, Benchmark computations for Maxwell equations for the approximation of highly singular solutions, `https://perso.univ-rennes1.fr/monique.dauge/benchmax.html`, [Online; last accessed 22-December-2022].

[41] R. W. Davies, K. Morgan, and O. Hassan, A high order hybrid finite element method applied to the solution of electromagnetic wave scattering problems in the time domain, Computational Mechanics, 44, pp. 321–331, 2009.

[42] H. Duan, Z. Du, W. Liu, and S. Zhang, New mixed elements for Maxwell equations, SIAM Journal on Numerical Analysis, 57(1), pp. 320–354, 2019.

[43] H. Duan, Z. Du, W. Liu, S. Zhang, and J. Ma, A family of optimal Lagrange elements for Maxwell's equations, Journal of Computational and Applied Mathematics, 358, pp. 241–265, 2019.

[44] H. Duan, R. Tan, S. Yang, and C. You, Computation of Maxwell singular solution by nodal-continuous elements, Journal of Computational Physics, 268, pp. 63–83, 2014.

[45] Y. El-Batawy, F. Mohammedy, and M. Deen, *Resonant cavity enhanced photodetectors: Theory, design and modeling*, pp. 415–470, 10 2015, ISBN 9781782424451.

[46] P. Fernandes and G. Gilardi, Magnetostatic and electrostatic problems in inhomogeneous anisotropic media with irregular boundary and mixed boundary conditions, Mathematical Models and Methods in Applied Sciences, 07(07), pp. 957–991, 1997.

[47] M. Fortin, An analysis of the convergence of mixed finite element methods, ESAIM: Mathematical Modeling and Numerical Analysis - Modeling Mathematical and Numerical Analysis, 11(4), pp. 341–354, 1977.

[48] M. Franco, A. Passaro, F. Neto, J. Cardoso, and J. Machado, Modal analysis of anisotropic diffused-channel waveguide by a scalar finite element method, IEEE Transactions on Magnetics, 34(5), pp. 2783–2786, 1998.

[49] N. Georg, W. Ackermann, J. Corno, and S. Schöps, Uncertainty quantification for Maxwell's eigenproblem based on isogeometric analysis and mode tracking, Computer Methods in Applied Mechanics and Engineering, 350, pp. 228–244, 2019.

[50] V. Girault and P. Raviart, *Finite Element Methods for Navier-Stokes Equations, Theory and Algorithms*, Springer-Verlag, Berlin, 1986.

[51] M. Halla, Galerkin approximation of holomorphic eigenvalue problems: weak t-coercivity and t-compatibility, Numerische Mathematik, 148, pp. 387–407, 2021.

[52] P. Hansbo and T. Rylander, A linear nonconforming finite element method for Maxwell's equations in two dimensions. Part i: Frequency domain, Journal of Computational Physics, 229, pp. 6534–6547, 2019.

[53] F. Hecht, New development in FreeFem++, Journal of numerical mathematics, 20(3-4), pp. 251–266, 2012.

[54] M. W. Hess and P. Benner, Fast evaluation of time–harmonic Maxwell's equations using the reduced basis method, IEEE Transactions on Microwave Theory and Techniques, 61(6), 2013.

[55] J. S. Hesthaven and T. Warburton, High-order nodal discontinuous Galerkin methods for the Maxwell eigenvalue problem, Philosophical Transactions of The Royal Society A: Mathematical, Physical and Engineering Sciences, 362, pp. 493–524, 2004.

[56] V. Hill, O. Farle, and R. Dyczij-Edlinger, A stabilized multilevel vector finite-element solver for time-harmonic electromagnetic waves, IEEE Transactions on Magnetics, 39(3), 2003.

[57] W. Jiang, N. Liu, Y. Tang, and Q. H. Liu., Mixed finite element method for 2D vector Maxwell's eigenvalue problem in anisotropic media, Progress In Electromagnetics Research, 148, pp. 159–170, 2014.

[58] F. Kikuchi, Mixed and penalty formulations for finite element analysis of an eigenvalue problem in electromagnetism, Computer Methods in Applied Mechanics and Engineering, 64, pp. 509–521, 1987.

[59] F. Kikuchi, On a discrete compactness property for the Nédélec finite elements, Journal of the Faculty of Science, University of Tokyo, 36, pp. 479–490, 1989.

[60] A. Kirsch and F. Hettlich, *The Mathematical Theory of Time-Harmonic Maxwell's Equations*, Springer, 2014, ISBN 978-3-319-11085-1.

[61] A. J. Kobelansky and J. P. Webb, Eliminating spurious modes in finite-element waveguide problems by using divergence-free fields, Electronics Letters, 22, pp. 569–570, 1986.

[62] A. Konrad, High-order triangular finite elements for electromagnetic waves in anisotropic media, IEEE Transactions on Microwave Theory and Techniques, MTT-25, pp. 353–360, 1977.

[63] A. Konrad, On the reduction of the number of spurious modes in the vectorial finite-element solution of three-dimensional cavities and waveguides, IEEE Transactions on Microwave Theory and Techniques, 34(2), pp. 224–227, 1986.

[64] S. Kurz, S. Schöps, G. Unger, and F. Wolf, Solving Maxwell's eigenvalue problem via isogeometric boundary elements and a contour integral method, Mathematical Methods in the Applied Sciences, 44, 2020.

[65] M. G. Larson and F. Bengzon, *The Finite Element Method: Theory, Implementation, and Applications*, Springer, 2013.

[66] J. Lee, R. Lee, and A. Cangellaris, Time-domain finite-element methods, IEEE Transactions on Antennas and Propagation, 45(3), 1997.

[67] F. Li, Y. Wang, C. Zhang, and G. Yu, Boundary element method for band gap calculations of two-dimensional solid phononiccrystals, Engineering Analysis with Boundary Elements, 37, pp. 225–235, 2013.

[68] J. Li, X. Lu, C. G. Farquharson, and X. Hu, A finite-element time-domain forward solver for electromagnetic methods with complex-shaped loop sources, Geophysics, 83(3), pp. E117–E132, 2018.

[69] X. Lin, G. Cai, H. Chen, N. Liu, and Q. H. Liu, Modal analysis of 2D material-based plasmonic waveguides by mixed spectral element method with equivalent boundary condition, Journal of Lightwave Technology, 38(14), pp. 3677–3686, 2020.

[70] N. Liu, L. E. Tobon, Y. Zhao, Y. Tang, and Q. H. Liu, Mixed spectral-element method for 3D Maxwell's eigenvalue problem, IEEE Transactions on Microwave Theory and Techniques, 63(2), 2015.

[71] J. C. Maxwell, *Treatise on Electricity and Magnetism*, Clareonden Press Series, 1873.

[72] M. Mehdizadeh, *Fundamentals of Field Applicators and Probes at RF and Microwave Frequencies*, pp. 35–66, 12 2010, ISBN 9780815515920.

[73] R. Misawa, K. Niino, and N. Nishimura, Boundary integral equations for calculating complex eigenvalues of transmission problems, SIAM Journal on Applied Mathematics, 77(2), pp. 770–788, 2017.

[74] P. Monk, An analysis of Nédélec's method for the spatial discretization of Maxwell's equations, Journal of Computational and Applied Mathematics, 47, pp. 101–121.

[75] P. Monk, A mixed method for approximating Maxwell's equations, SIAM Journal on Numerical Analysis, 28(6), pp. 1610–1634.

[76] P. Monk, A finite element method for approximating the time-harmonic Maxwell equations, Numerische Matematik, 63, pp. 243–261, 1992.

[77] P. Monk, *Finite Element Methods for Maxwell's Equations*, Clarendon Press, Newark, 2003.

[78] P. Monk and L. Demkowicz, Discrete compactness and the approximation of Maxwell's equations in $\mathbb{R}^3$, Mathematics of Computation, 70(234), pp. 507–523, 2000.

[79] N. Nguyen, J. Peraire, and B. Cockburn, Hybridizable discontinuous Galerkin methods for the time-harmonic Maxwell's equations, Journal of Computational Physics, 230, pp. 7151–7175, 2011.

[80] J. C. Nédélec, Mixed finite elements in $\mathbb{R}^3$, Numerische Mathematik, 35, pp. 315–341.

[81] F. T. Orlandini, P. R. B. Devloo, H. E. Hernandez-Figueroa, and L. P. de Oliveira, A high-precision FEM scheme for modal analysis of photonic waveguides using high-order edge elements, in *2019 International Conference on Optical MEMS and Nanophotonics (OMN)*, pp. 160–161, 2019.

[82] J. Patrick Ciarlet and G. Hechme., Mixed, augmented variational formulations for Maxwell's equations:numerical analysis via the macroelement technique, Numerische Mathematik (submitted), 2007.

[83] L. Pichon, A. Bourhattas, and A. Razek, An efficient solution for dielectric-loaded or ridged waveguides problems, Electronics Letters, 11, pp. 17–20, 1992.

[84] W. Pinello, R. Lee, and A. C. Cangellaris, Finite element modeling of electromagnetic wave interactions with periodic dielectric structures, IEEE Transactions on Microwave Theory and Techniques, 42(12), 1994.

[85] Z. Qiao., C. Yao, and S. Jia, Superconvergence and extrapolation analysis of a nonconforming mixed finite element approximation for time-harmonic Maxwell's equations, Journal of Scientific Computing, 46, pp. 1–19.

[86] P. A. Raviart and J. M. Thomas, A mixed finite element for second order elliptic problems, in I. Galligani and E. Magenes, editors, *Mathematical Aspects of Finite Element Methods*, pp. 292–315, 1977.

[87] J. F. Ready, Laser components and accessories, in J. F. Ready, editor, *Industrial Applications of Lasers*, pp. 144–192, Academic Press, San Diego, second edition, 1997.

[88] C. J. Reddy, M. D. Deshpande, C. R. Cockrell, and F. B. Beck., Finite element method for eigenvalue problems in electromagnetics, NASA Technical Paper, 3485, 1994.

[89] Z. Ren, T. Kalscheuer, S. Greenhalgh, and H. Maurer, A goal-oriented adaptive finite-element approach for plane wave 3D electromagnetic modelling, Geophysical Journal International, 194, pp. 700–718, 2013.

[90] M. E. Rognes, R. C. Kirby, and A. Logg, Efficient assembly of $H(\mathrm{div})$ and $H(\mathrm{curl})$ conforming finite elements, SIAM Journal on Scientific Computing, 31(6), pp. 4130–4151, 2009.

[91] A. Schneebeli, An $H(\mathrm{curl}; \Omega)$ FEM: Nédélec's elements of first type, Technical Report, 2003.

[92] S. Schnepp, E. Gjonaj, and T. Weiland, A hybrid finite integration–finite volume scheme, Journal of Computational Physics, 229(11), pp. 4075–4096, 2010.

[93] J. Schöberl, C++ 11 implementation of finite elements in NGSolve, Institute for analysis and scientific computing, Vienna University of Technology, 30, 2014.

[94] H. Shahnoor and K. Behzad, Calculation of multiconductor underground cables high-frequency per-unit-length parameters using electromagnetic modal analysis, IEEE Transactions on Power Delivery, 28(1), pp. 276–284, 2013.

[95] M. Smolik and V. Skala, Vector field interpolation with radial basis functions, in *Linköping Electronic Conference Proceedings*, volume 127, pp. 161–174, 2016.

[96] D. Song and Y. Lu, Analyzing leaky waveguide modes by pseudospectral modal method, Photonics Technology Letters, Ieee, 27, pp. 955–958, 05 2015.

[97] J. Sun and A. Zhou, *Finite Element Methods for Maxwell's Equations*, CRC Press, 2017.

[98] N. Thomas, P. Sewell, and T. M. Benson, A new full-vectorial higher order finite-difference scheme for the modal analysis of rectangular dielectric waveguides, Journal of Lightwave Technology, 25(9), pp. 2563–2570, 2007.

[99] C. Y. Tian, Y. Shi, and C. H. Chan, Interior penalty discontinuous Galerkin time domain method based on wave equation for 3D electromagnetic modeling, IEEE Transactions on Antennas and Propagation, 65(12), pp. 7174–7184, 2009.

[100] G. Unger, Convergence analysis of a Galerkin boundary element method for electromagnetic resonance problems, Partial Differential Equations and Applications, 2(39), 2021.

[101] J. L. Volakis, A. Chatterjee, and L. C. Kempel, *Finite Element Method Electromagnetics: Antennas, Microwave Circuits, and Scattering Applications*, 1998.

[102] C. Wieners and J. Xin, Boundary element approximation for Maxwell's eigenvalue problem, Mathematical Methods in the Applied Sciences, 36, pp. 2524–2539, 2013.

[103] Y. Yang, H. Bi, J. Han, and Y. Yu, The shifted-inverse iteration based on the multigrid discretizations for eigenvalue problems, SIAM Journal on Scientific Computing, 37(6), pp. A2583–A2606, 2015.

[104] M. Zghal, F. Bahloul, R. Chatta, R. Attia, D. Pagnoux, P. Roy, G. Melin, and L. Gasca, Full vector modal analysis of microstructured optical fiber propagation characteristics, in *Novel Optical Systems Design and Optimization VII*, volume 5524, pp. 313 – 322, SPIE, 2004.

[105] L. Zhong, S. Shu, G. Wittum, and J. Xu, Optimal error estimates for Nédélec edge elements for time-harmonic Maxwell's equations, Journal of Computational Mathematics, 27(5), pp. 563–572, 2009.

[106] J. Zhou, X. Hu, S. Shu, and L. Chen, Two-grid methods for Maxwell eigenvalue problems, SIAM Journal on Numerical Analysis, 52(4), pp. 2027–2047, 2014.

[107] Ö. Özgün and M. Kuzuoğlu, *MATLAB-based Finite Element Programming in Electromagnetic Modeling*, CRC Press, 2019, ISBN 9781498784085.